Modeling and Simulation of Neocortical Micro- and Mesocircuitry. Part II: Physiology and Experimentation

James B. Isbister[1,†], András Ecker[1,†], Christoph Pokorny[1,†], Sirio Bolaños-Puchet[1,†], Daniela Egas Santander[1,†], Alexis Arnaudon[1], Omar Awile[1], Natali Barros-Zulaica[1], Jorge Blanco Alonso[1], Elvis Boci[1], Giuseppe Chindemi[1,2], Jean-Denis Courcol[1], Tanguy Damart[1], Thomas Delemontex[1], Alexander Dietz[1], Gianluca Ficarelli[1], Mike Gevaert[1], Joni Herttuainen[1], Genrich Ivaska[1], Weina Ji[1], Daniel Keller[1], James King[1], Pramod Kumbhar[1], Samuel Lapere[1], Polina Litvak[1], Darshan Mandge[1], Eilif B. Muller[1,3,4], Fernando Pereira[1], Judit Planas[1], Rajnish Ranjan[1], Maria Reva[1], Armando Romani[1], Christian Rössert[1], Felix Schürmann[1], Vishal Sood[1], Aleksandra Teska[1], Anil Tuncel[1], Werner Van Geit[1], Matthias Wolf[1], Henry Markram[1,*,‡], Srikanth Ramaswamy[1,5,*,‡], and Michael W. Reimann[1,*,‡]

[1]Blue Brain Project, École polytechnique fédérale de Lausanne (EPFL), Campus Biotech, Geneva, Switzerland
[2]Department of Basic Neurosciences, University of Geneva, Geneva, Switzerland
[3]Department of Neurosciences, Faculty of Medicine, Université de Montréal, Montréal, Canada
[4]CHU Sainte-Justine Research Center, Montréal, Canada
[5]Neural Circuits Laboratory, Newcastle University, Newcastle, UK
[†]Co-lead authors
[‡]Co-senior authors
[*]Corresponding authors

August 4, 2023

Summary

Cortical dynamics underlie many cognitive processes and emerge from complex multiscale interactions, which can be studied in large-scale, biophysically detailed models. We present a model comprising eight somatosensory cortex subregions, 4.2 million morphological and electrically-detailed neurons, and 13.2 billion local and long-range synapses. *In silico* tools enabled reproduction and extension of complex laboratory experiments under a single parameterization, providing strong validation. We reproduced millisecond-precise stimulus-responses, stimulus-encoding under targeted optogenetic activation, and selective propagation of stimulus-evoked activity to downstream areas. The model's direct correspondence with biology generated predictions about how multiscale organisation shapes activity. We predict that structural and functional recurrency increases towards deeper layers and that stronger innervation by long-range connectivity increases local correlated activity. The model also predicts the role of inhibitory interneuron types in stimulus encoding, and of different layers in driving layer 2/3 stimulus responses. Simulation tools and a large subvolume of the model are made available.

1 Introduction

Cortical dynamics underlie many cognitive processes and emerge from complex multiscale interactions, which are challenging to study *in vivo*. Such dynamics can be explored in *large-scale, data-driven, biophysically detailed* models (Markram et al., 2015; Billeh et al., 2020), which integrate different levels of organization. The strict biological and spatial context enables the integration of knowledge and theories, the testing and generation of precise hypotheses, and the opportunity to recreate and extend diverse laboratory experiments within a single model. Investigating the multiscale interactions that shape perception, requires a model of multiple cortical subregions with interregion connectivity. This approach differs from more abstract models in that it emphasizes *anatomical completeness* of a chosen brain volume rather than implementing a specific hypothesis. Using a "bottom-up" modeling approach, many detailed constituent models are combined to produce a larger multiscale model. To the best possible approximation, such models should explicitly include different cell and synapse types with the same quantities, geometric configuration and connectivity patterns as the biological tissue it represents.

Here and in our companion paper (Reimann et al., 2022a), we present how we built and validated a model of the entire non-barrel primary somatosensory cortex (nbS1) comprising eight subregions. Whilst our previous data-driven, biophysically detailed model (Markram et al., 2015) provided insights at the scale of a single cortical column (Reimann et al., 2013, 2017, 2022b; Nolte et al., 2019, 2020; Newton et al., 2021), the new model is ∼140 times larger and to our knowledge offers the first simulations of *in vivo*-like spontaneous and stimulus-evoked activity in a biophysically detailed cortical model with interregion connectivity. In the companion paper, we introduce the anatomical model (Fig. 1, Step 1), describing how neuron morphologies were placed within an atlas-based geometry and connected through local and long-range synapses. Here, we describe our improved techniques to model and validate the electrical properties of neurons and synapses (Figure 1, Steps 2 & 3 (Reva et al., 2022; Barros-Zulaica et al., 2019)), and to compensate for input from missing brain areas (Figure 1, Steps 4). These improvements enabled enhanced validation of emerging *in vivo*-like activity (Figure 1, Steps 5), including the reproduction and extension of five published studies in rodent sensory cortex under a single *in vivo*-like regime (Figure 1, Steps 6). The model's direct biological correspondence and ability to go beyond laboratory experiments generated diverse predictions about how multiscale orgnanization shapes emergent activity.

Ensuring that network activity emerges from the same interactions driving *in vivo* dynamics, is best validated through comparison with an increasing battery of laboratory experiments. Spontaneous activity reproduced layer-wise *in vivo* firing rates (or a specified proportion of *in vivo* firing rates to account for *in vivo* recording bias (Wohrer et al., 2013)), varied along a spectrum of asynchronous to synchronous activity, exhibited spatially structured fluctuations and produced long-tailed firing rate distributions with sub 1 Hz peaks as *in vivo* (Wohrer et al., 2013; Buzsáki and Mizuseki, 2014). Under the same parameterization, the model also reproduced precise millisecond dynamics of layer-wise populations in response to simple stimuli and demonstrated selective propagation of stimulus-evoked activity to downstream areas. Again under the same parameterization, we reproduced and extended more complex experiments through accurate modeling of targeted optogenetic stimulation and lesions. Particularly, through methods currently not possible *in vivo*, the model generated predictions about the role of different layers in

driving layer 2/3 stimulus responses and how inhibitory interneuron types encode contrast, synchronous and rate-coded information.

Using the full structural connectome and metrics outlined in the companion paper, the model made further predictions about the relation between cortical structure and function. For example, the model predicts that the recurrency of connectivity and activity jointly increase from superficial to deeper layers, and that subregions more strongly innervated by long-range connectivity have higher correlated activity locally. Such analysis provided general insights and tools for calibrating and understanding large cortical models. Importantly, we highlight where emergent activity shows discrepancies with *in vivo* activity, to guide future data-driven model refinement. To provide a framework for further simulation-based studies and integration of experimental data, a sizable part of the model and simulation tools are made available to the community (Figure 1, Step 7).

These results were made possible by a novel methodology presented here, which compensates for missing synapses from non-modeled brain regions. Without compensating for the resulting lack of excitatory drive, an *in vivo*-like and computationally relevant activity state can not be attained (see also Billeh et al., 2020). This represents a fundamental challenge for biophysically detailed models. Compensation which changes existing parameters would violate the important stipulation of anatomical completeness, whilst modeling each missing synapse ($\sim$2 times the model's 13.2B synapses) would be too computationally expensive (Cremonesi et al., 2020). Here we model the effect of these missing synapses explicitly as noisy somatic conductance injections (Destexhe et al., 2001) and present an algorithm which efficiently calibrates the parameters of this input compensation, despite the non-linearity and computational cost of simulations (Figure 1, Step 4). Unlike in our previous model (Markram et al., 2015), these parameters were specific for different neuron populations and were found to be in accordance with laminar profiles of long range innervation (Felleman and Van Essen, 1991; Harris et al., 2019; Gao et al., 2022). Importantly, the algorithm rapidly produces a set of activity regimes for testing, closing the loop for iterative refinement of cortical models.

2 Results

The companion paper describes the full anatomical nbS1 model containing 4.2M morphological neuron models, connected through 9.1B local synapses and 4.1B long-range synapses (Reimann et al., 2022a). Each neuron is modeled as a multi-compartmental model belonging to one of 60 morphological types (m-types; Fig. 2A1), and is either an instance or statistical variant of an exemplar in a pool of 1,017 morphological reconstructions. Neurons were placed (orientated towards the surface) within an atlas-based geometry (Fig. 2A2) based on estimated layer-wise density profiles of different morphological types. Local connectivity is based on axo-dendritic overlap with neighbouring neurons, whilst long-range connectivity combines data on interregion connectivity and laminar innervation profiles. Thalamocortical afferents were also modeled based on laminar innervation to the barrel cortex. To simulate emergent activity it is necessary to model and validate the electrical properties of these neurons and synapses (Figure 1 Steps 2 & 3). These modeling steps are based on published methods and data sources (Table 1), and are summarized first. The method for compensating for missing synapses and the remaining results are then described (Figure 1 Steps 4-6).

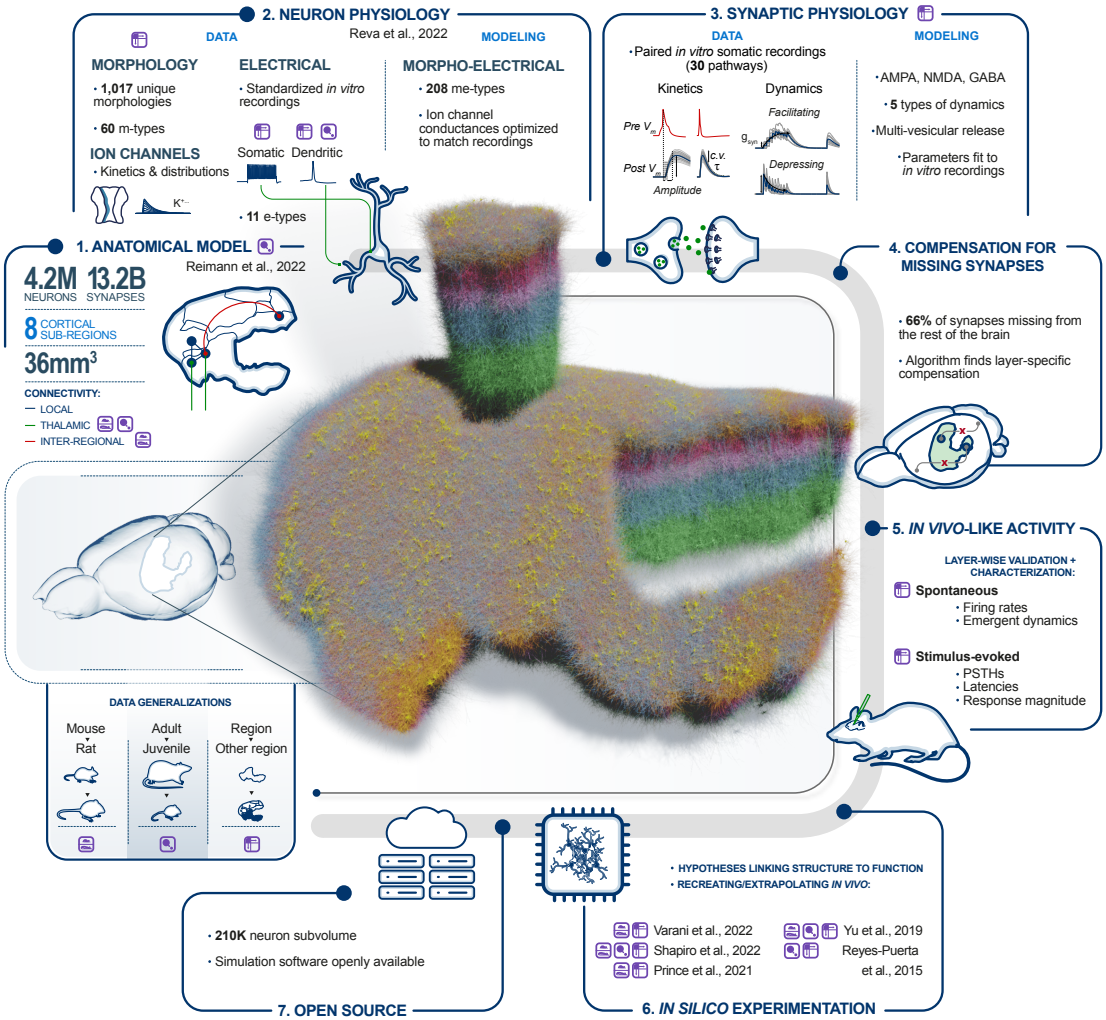

Figure 1: Overview of the physiology and simulation workflow. 1. Anatomical model: Summary of the anatomical nbS1 model described in the companion paper. **2. Neuron physiology:** Neurons were modeled as multi-compartment models with ion channel densities optimised using previously established methods and data from somatic and dendritic recordings of membrane potentials *in vitro*. **3. Synaptic physiology:** Models of synapses were built using previously established methods and data from paired recordings *in vitro*. **4. Compensation for missing synapses:** Excitatory synapses originating from outside nbS1 were compensated with noisy somatic conductance injection, parameterized by a novel algorithm. **5. *In vivo*-like activity:** We calibrated an *in silico* activity regime compatible with *in vivo* spontaneous and stimulus-evoked activity. **6. *In silico* experimentation:** Five laboratory experiments were recreated. Two were used for calibration and three of them were extended beyond their original scope. **7. Open Source:** Simulation software and a seven column subvolume of the model are available on Zenodo (see data availability statement). **Data generalisations:** Three data generalisation strategies were employed to obtain the required data. Left: Mouse to rat, middle: Adult to juvenile (P14) rat, right: Hindlimb (S1HL) and barrel field (S1BF) subregions to the whole nbS1. Throughout the figure, the corresponding purple icons show where these strategies were used.

Table 1: Previously published modeling techniques and data to parameterize them that were combined in this work to model the physiology of nbS1 and conduct *in silico* experimentation.

	Data	
Stage	**Topic**	**Reference**
Neuron physiology	E-type composition	Markram et al. (2004, 2015)
	Electrophysiological recordings	Markram et al. (2015)
		Larkum et al. (2001)
		Nevian et al. (2007)
	Ion-channel models	Reva et al. (2022)
Synaptic physiology	Synaptic pathway physiology	Markram et al. (2015)
		Barros-Zulaica et al. (2019)
		Gupta et al. (2000)
		13 additional sources in Tables S4, S5, S6
In vivo-like activity	*In vivo* spont. firing rates	Reyes-Puerta et al. (2015)
		De Kock et al. (2007)
	In vivo evoked responses	Reyes-Puerta et al. (2015)
		Yu et al. (2019)
	In vivo thalamic spiking	Diamond et al. (1992)
		Yu et al. (2019)
In silico experimentation	L4 - L2/3 pathway	Varani et al. (2022)
	Visual contrast	Shapiro et al. (2022)
	Coding in inhibitory subpopulations	Prince et al. (2021)
	Modeling methods	
Stage	**Topic**	**Reference**
Neuron physiology	E-model building	Van Geit et al. (2016)
		Reva et al. (2022)
Synaptic physiology	Synapse model building	Ecker et al. (2020)
	Model of multi-vesicular release	Barros-Zulaica et al. (2019)
In vivo-like activity	Missing input compensation	*New, original methods based on Destexhe et al. (2001)
In silico experimentation		*New, original methods

2.1 Modeling and validation of neuron physiology

Electrical properties of single neurons were modeled by optimising ion channel densities in specific compartment-types (soma, axon initial segment (AIS), basal dendrite, and apical dendrite) (Figure 2B) using an evolutionary algorithm (IBEA; Van Geit et al., 2016) so that each neuron recreates electrical features of its corresponding electrical type (e-type) under multiple standardized protocols. The methodology and resulting electrical models are described in Reva et al. (2022) (see also STAR*Methods). Electrical features included firing properties (e.g. spike frequency, interspike interval), action potential waveforms (e.g. fall and rise time, width) and passive properties (e.g. input resistance). The optimisation was performed for a subset of neuron models. The resulting ion channel densities were generalised to other neuron models of the same e-type, and the resulting electrical activity of each neuron was validated against the corresponding electrical features, including the *characteristic* firing properties of the 11 e-types (Figure 2C).

For each of the 60 morphological types (m-types), the corresponding fractions of e-types were determined from experimental data as in Markram et al. (2015), resulting in

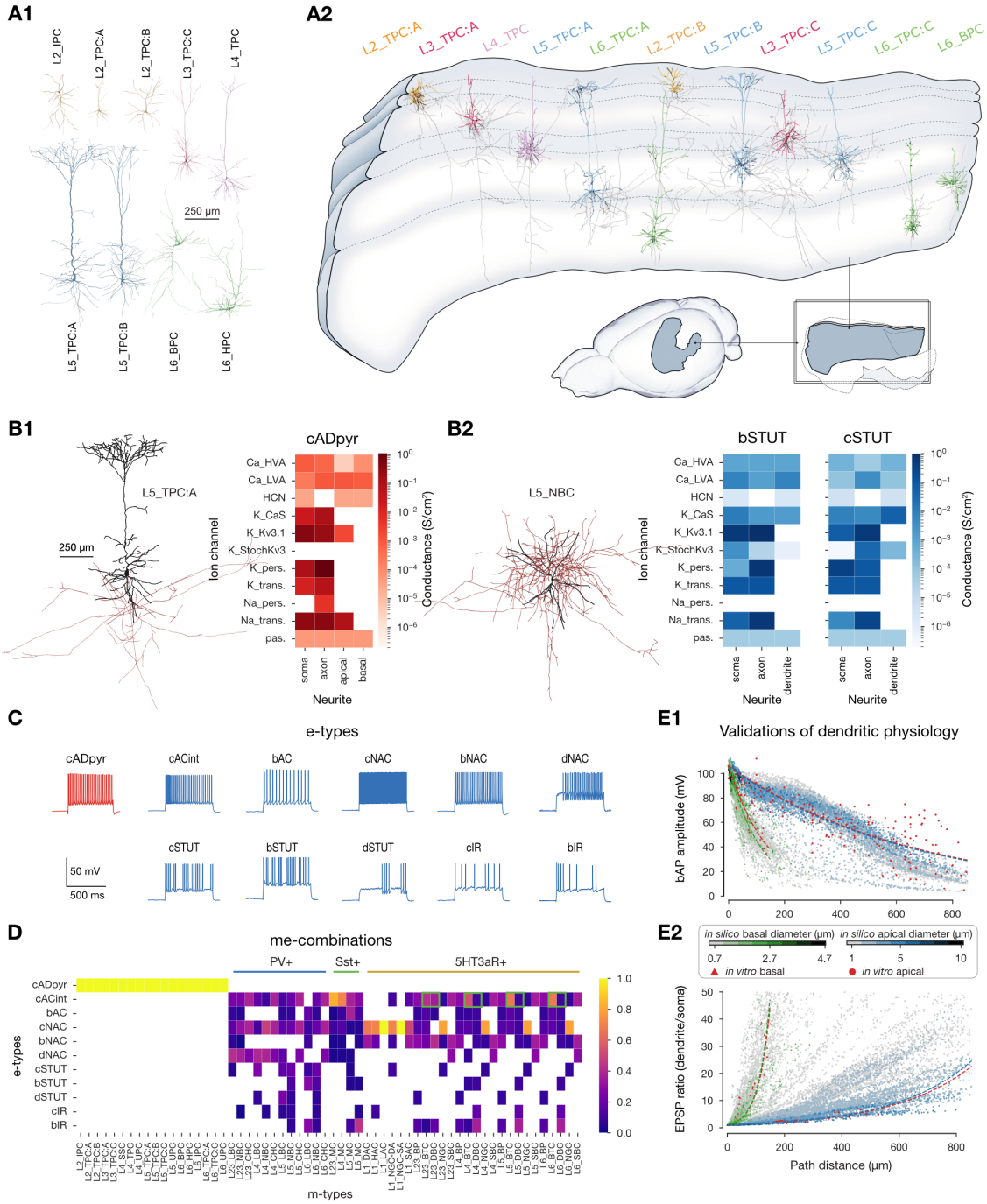

Figure 2: Modeling and validation of neuron physiology. **A1:** Example excitatory neuron morphologies. See companion paper for exemplar morphologies of all morphological types. **A2:** Example morphologies placed within the atlas-based volume. Axons shown in grey. **B**: Optimized conductance densities for two exemplary e-types. **B1**: cADpyr e-type on L5_TPC:A m-type, **B2**: bSTUT and cSTUT e-types on L5_NBC m-type. (The L5_NBC m-type is combined with more e-types than the two shown, see panel D.) Morphologies were visualized with NeuroMorphoVis (Abdellah et al., 2018). Neurite diameters are enlarged (x3) for visibility. Soma and dendrites in black, axon in red. **C:** e-types used in the model. As used in Markram et al. (2015) and similar to the Petilla terminology (Ascoli et al., 2008)).

D: me-type composition. Heatmap shows the proportion of e-types for each m-type. Each me-type is assigned to one of the three I subpopulations. Assignments depending not only on m-type are highlighted by a green box. Particularly, for BTC and DBC m-types, the cACint e-type belongs to the Sst+ subpopulation. **E**: Validation of dendritic physiology of all L5 TTPCs. Panel reproduced from Reva et al. (2022). **E1**: Validation of back-propagating action potential (bAP) amplitude (i.e., the dependence of bAP amplitude on distance from the soma) for basal (green) and apical (blue) dendrites. Reference data (in red) comes from Stuart and Sakmann (1994); Larkum et al. (2001) (apical) and Nevian et al. (2007) (basal). Lines show exponential fits for the *in silico* (green and blue) and *in vitro* (red) data. Color bar indicates dendritic diameter. **E2:** Validation of EPSP attenuation. Reference data (in red) comes from Berger et al. (2001) (apical) and Nevian et al. (2007) (basal). Lines and colorbar same as in D2.

208 morpho-electrical types (me-types; Figure 2D). Correspondence with predominant expression of biological markers PV (parvalbumin), Sst (somatostatin) or 5HT3aR (serotonin receptor 3A) was determined based on me-type, as previously done in Markram et al. (2015) (Figure 2D). Finally, for layer five thick-tufted pyramidal cell (L5 TTPC) morphologies, we found that dendritic electrical features, namely the attenuation of back propagating action potentials and excitatory postsynaptic potentials (EPSPs), reproduced experimental measurements (Figure 2E, Reva et al., 2022).

2.2 Modeling and validation of synaptic physiology

Synapses are modeled with a stochastic version of the Tsodyks-Markram model (Tsodyks and Markram, 1997; Markram et al., 1998; Fuhrmann et al., 2002; Loebel et al., 2009), upgraded to feature multi-vesicular release as described in Barros-Zulaica et al. (2019) and Ecker et al. (2020). The model assumes a pool of available vesicles that is utilized by a presynaptic action potential, with a release probability dependent on the extracellular calcium concentration ($[Ca^{2+}]_o$; Ohana and Sakmann, 1998; Rozov et al., 2001; Borst, 2010). Additionally, single vesicles spontaneously release with a low frequency as an additional source of variability. The utilization of vesicles leads to a postsynaptic conductance with bi-exponential kinetics. Short-term plasticity (STP) dynamics in response to sustained presynaptic activation are either facilitating (E1/I1), depressing (E2/I2), or pseudo-linear (I3). E synaptic currents consist of both AMPA and NMDA components, whilst I currents consist of a single $GABA_A$ component, except for neurogliaform cells, whose synapses also feature a slow $GABA_B$ component. The NMDA component of E synaptic currents depends on the state of the Mg^{2+} block (Jahr and Stevens, 1990), with parameters fit to cortical recordings from Vargas-Caballero and Robinson (2003) by Chindemi et al. (2022).

The workflow for determining a dense parameter set for all synaptic pathways, starting with sparse data from the literature, is described for the use case of hippocampal CA1 in Ecker et al. (2020) and briefly in the STAR*Methods. We combined data sources used in Markram et al. (2015), with a large number of recent data sources (Qi and Feldmeyer, 2016; Barros-Zulaica et al., 2019; Yang et al., 2020, 2022). The resulting pathway-specific parameters are listed in Tables S1, S2, S3, the most common short-term dynamics are depicted in Figure 3A1-2, and the assignment of STP profiles to different pathways are shown in Figure A3. Postsynaptic potential (PSP) amplitudes and their coefficient of variation (CV; std/mean) closely matched their biological counterparts ($r = 0.99$, $n = 27$; Figure 3B1; Table S4 and $r = 0.63$, $n = 10$; Figure 3C1; Table S5, respectively). The dense parameter set also allowed prediction of PSP amplitudes and CVs for all cortical

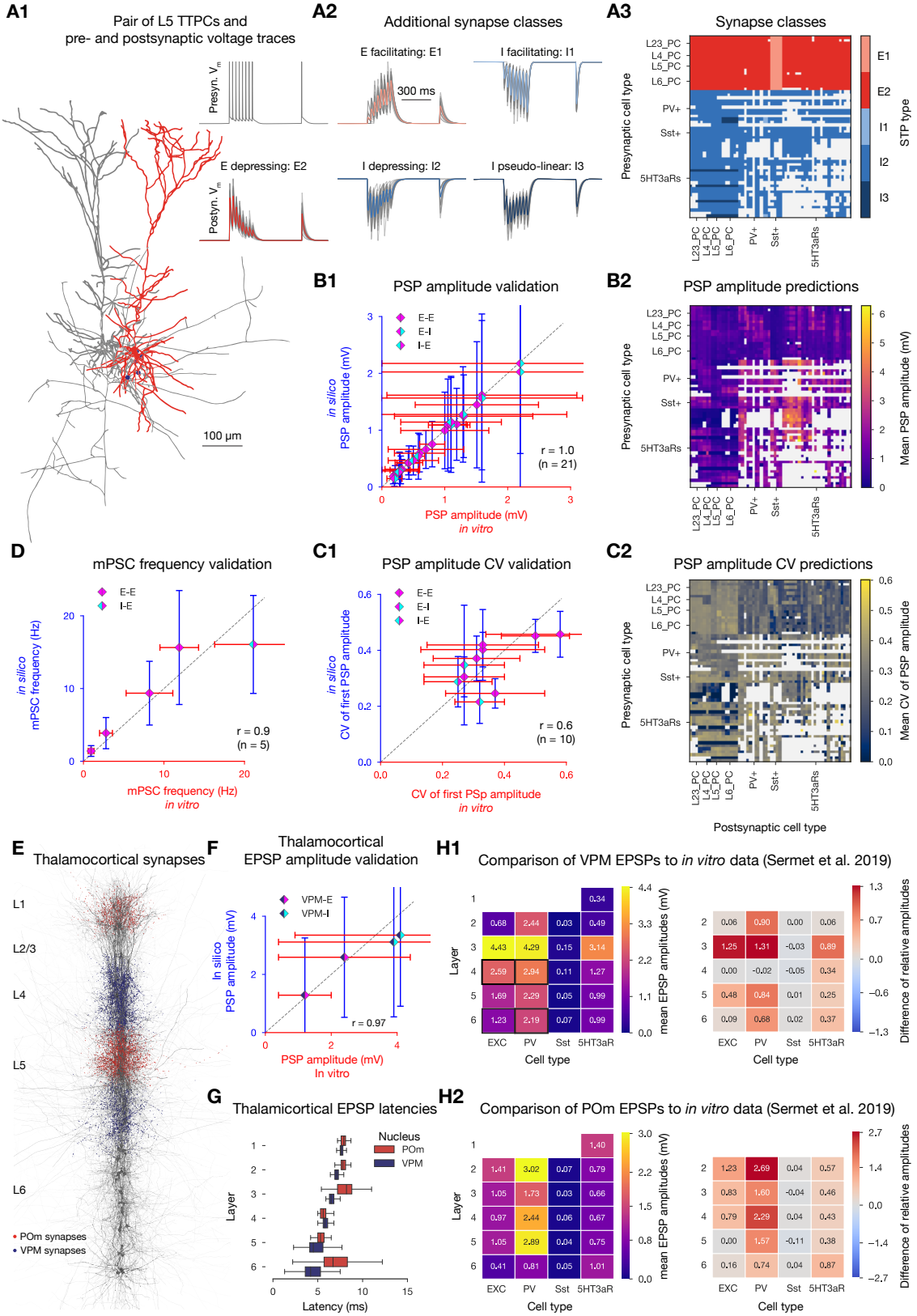

Figure 3: Modeling and validation of synaptic physiology. Caption on the following page.

A1: Exemplary pair of L5 TTPCs (visualized with NeuroMorphoVis (Abdellah et al., 2018)). Presynaptic cell in gray, postsynaptic cell in red, synapses between them in purple. Neurite diameters are enlarged (x3) for visibility and axons were cut to fit into the figure. Pre- and postsynaptic voltage traces on the top right. **A2:** Exemplary postsynaptic traces with different STP profiles. **A3:** Assignment of STP profiles to viable pathways. (Pathways were considered viable if there were at least 10 connections in all eight subregions of the model.) **B1:** Validation of first PSP amplitudes (see also Table S4). Dashed gray line represents perfect correlation between experimental and model values. Error bars show one standard deviation (also for C1, D and F). **B2:** Predicted PSP amplitudes of all viable pathways in the circuit. Postsynaptic cells were held at -70 mV using an *in silico* voltage-clamp. Means were calculated over 100 pairs of neurons with 35 repetitions each. **C1** and **C2**: same as B1 and B2, but showing the CV of the first PSP amplitude (corresponding Table is S5). **D:** Validation of mPSC frequencies (see also Table S6). **E:** Location of synapses from VPM fibers (purple) and POm fibers (red) on 38 neurons (dark gray) in a 5 μm radius column (visualized with `BioExplorer`). **F:** Validation of thalamocortical EPSP amplitudes as in B1. The four pathways used for the validation are marked with a black rectangle on H1 to its right. **G**: EPSP latencies (time from presynaptic spike to the rise to 5% of peak EPSP amplitude in the postsynaptic trace). **H1** Left: mean VPM evoked EPSP amplitudes on postsynaptic cell types (over 50 pairs). Right: Comparison of normalized *in silico* amplitudes (normalized by L4 E as in Sermet et al. (2019)) to *in vitro* reference data from Sermet et al. (2019). Heatmap shows model minus reference values, thus positive values indicate a higher normalized EPSP amplitude in our model than in the reference experimental dataset. **H2**: same as H1 but for POm (normalized by L5 E as in Sermet et al. (2019)).

pathways (Figure 3B2, C2). The frequency of miniature postsynaptic currents (mPSCs) were also in line with *in vitro* measurements ($r = 0.92$, $n = 5$; Figure 3D; Table S6).

The anatomical model includes fibers from the thalamus, based on fibres projecting to the barrel cortex from the ventral posteriomedial (VPM) and posteriormedial (POm) thalamic nuclei. These fibres make synaptic contacts within a radius of the fiber probabilistically based on laminar innervation profiles (see Reimann et al. (2022a); Figure 3E). Compared to the previous model (Markram et al., 2015), POm projections are added and the physiology of synapses from VPM improved (see STAR*Methods; Figure 3E, F). Latencies of layer-wise EPSPs increase with distance from the thalamus (Figure 3G). Additionally, thalamocortical EPSP amplitudes normalized relative to a single population were compared to normalized EPSPs in response to optogenetic stimulation targeting bundles of thalamic fibers (Sermet et al., 2019). This provided contrasting insights, however. For example, whilst VPM to L6 I EPSPs match the initial validation data (Figure 3F), VPM to L6 PV+ responses appear too strong relative to other populations (Figure 3H1). The results suggest that the model's POm to L5 E pathway is too weak, when compared to other POm to E and all POm to PV+ pathways (Figure 3H2, right).

2.3 Defining subvolumes and populations

To enable smaller simulations and targeted analyses, we defined standardized partitions comprising all neurons (and their connections) contained in a *subvolume* of the full nbS1 model. We decomposed the model into full-depth hexagonal prisms of a certain diameter that we call *hexagonal subvolumes*. These are slightly curved, following the geometry of the cortex, and have an intact layer structure. When the diameter of the hexagons is 520 μm, comparable to the size of the single cortical column model from (Markram et al., 2015), we call these subvolumes *columns*. Taken together, a *central column* and the six columns surrounding it define a *seven column subvolume* (Figure 4A). Additionally, when

we separately analyze the E and I neurons in different layers, we refer to them as neuron *populations* of the model or a subvolume. Groups of I neurons that predominantly express either PV, Sst or 5HT3aR markers, are referred to as *inhibitory subpopulations*.

2.4 Compensating for missing brain regions

Initial simulations produced no activity, and it was necessary to compensate for missing excitatory input from neurons external to the model. We estimated that the number of missing synapses for the full nbS1 and seven hexagon subvolume as $\sim$ two and seven times the number of internal synapses, based on Oh et al. (2014). We model the effect of these missing synaptic inputs explicitly as time-varying and statistically independent somatic conductance injections, using Ornstein-Uhlenbeck (OU) processes that mimic aggregated random background synaptic inputs (Destexhe et al., 2001; Figure 4B1; see also Discussion). The mean (OU_μ) and standard deviation (OU_σ) are defined as a percentage of an individual cell's input conductance at its resting membrane potential. The choice of OU_μ and OU_σ for different populations and $[Ca^{2+}]_o$ (Figure 4B2), determine the model's emergent dynamics and mean firing rates (Figure 4B3). Initial simulations showed that using the same value of OU_μ and OU_σ for all neurons makes some populations highly active whilst others are silent, or produces network-wide bursts. Finding population-specific OU parameters which produce stable *in vivo*-like activity is challenging, however, due to the non-linearity and computational cost of simulations.

We developed an algorithm that efficiently calibrates population-specific OU parameters, for different values of $[Ca^{2+}]_o$, which affects the strength and reliability of synaptic transmission (see "Synaptic Physiology"). Additionally, it fixes the ratio OU_σ/OU_μ, denoted R_{OU}, across all neurons to specific values representing the amount of noise in the extrinsic inputs (Figure 4B2). As extracellularly-derived firing rates are known to be severely overestimated to an unknown degree (Olshausen and Field, 2006; Wohrer et al., 2013; Buzsáki and Mizuseki, 2014), the algorithm finds parameters which produce realistic inter-population firing rate ratios at different global levels of activity (Figure 4B3). Specifically, it targets mean spontaneous firing rates of neuron populations that are a constant fraction P_{FR} of *in vivo* reference values, for 10 P_{FR} values between 0.1 and 1. We refer to $[Ca^{2+}]_o$, R_{OU} and P_{FR} as *meta-parameters*. The initial calibration was made for the seven hexagonal subvolume, and later generalised to the full nbS1 model.

The algorithm was first run for $[Ca^{2+}]_o = 1.1\,\text{mM}$, $R_{OU} = 0.4$. Target firing rates for the 10 P_{FR} values were reached (Figure 4C) after five iterations of 10 simulations of 6.5 seconds (Figure 4D, left upper). Only three iterations were needed when calibration began using previously calibrated parameters for different R_{OU} and $[Ca^{2+}]_o$ (Figure 4D, right upper). This allowed us to parameterize extrinsic input for a range of combinations of the three *meta-parameters* (Figure 4D, lower & 4E, left) within biologically relevant ranges ($[Ca^{2+}]_o$: 1.05 mM - 1.1 mM (Jones and Keep, 1988; Massimini and Amzica, 2001; Amzica et al., 2002; Gonzalez et al., 2022); P_{FR}: 0.1 - 1.0; R_{OU}: 0.2 - 0.4 (Destexhe et al., 2001)). We found that the resulting mean conductance injections were highly population-specific (Figure 4E, centre). The range of OU_μ values between populations was on average 5.2 times higher than the range of OU_μ values for a single population across meta-parameter combinations (Figure 4E, right). This was expected, as the missing long-range innervation is known to have specific and heterogeneous laminar profiles (Felleman and Van Essen, 1991; Harris et al., 2019; Gao et al., 2022). We estimated the number of missing

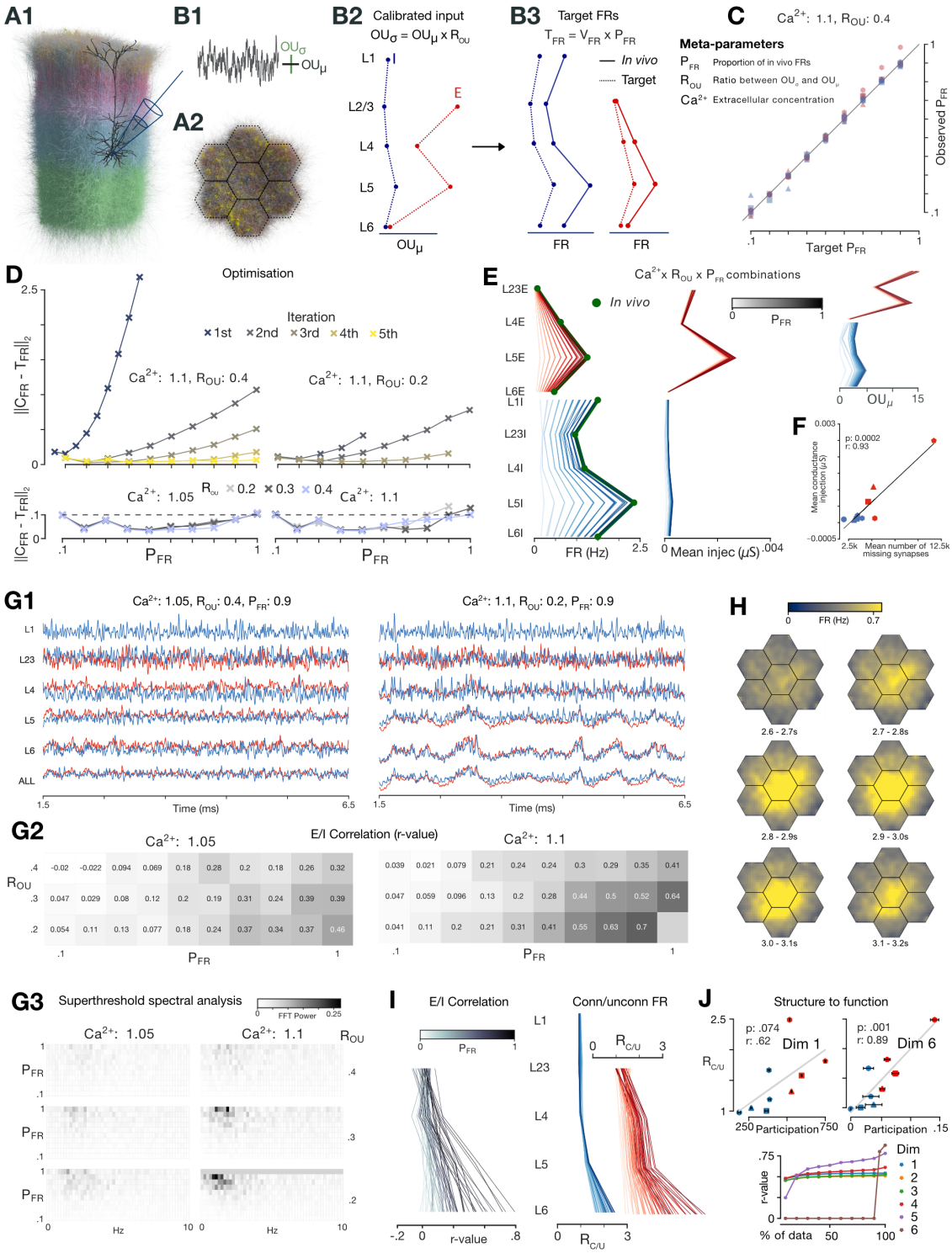

Figure 4: Spontaneous activity: calibration, *in vivo*-like dynamics, linking structure to function. A: Seven column subvolume. **B:** OU_μ and OU_σ of somatic conductance injection (B1) parameterized by population (B2) determine FRs (B3). Target FRs equal to *in vivo* firing rates multiplied by P_{FR}. Inset: Table summarising meta-parameters. **C:** Target P_{FR} (x-axis) plotted against the observed P_{FR} (y-axis) for each E (red) and I (blue) population after calibration. The number of sides of the shape indicates the layer (triangle used for L2/3).

D: Euclidean distance between target and observed P_{FR} values (over populations) decreases over iterations for two meta-parameter combinations (upper). Values after final iteration shown for all meta-parameter combinations (lower; dashed line shows termination condition). **E:** (left) Firing rates, (centre) mean conductance injection and (right) OU_μ by population for the non-bursting simulations (1 line per simulation; E and I values separated). **F:** Mean missing number of synapses vs. the mean conductance injection, averaged over all combinations, for each population. **G1:** Max normalised histograms for two meta-parameter combinations (5 ms bin size, 1σ Gaussian smoothing). **G2:** Effect of meta-parameters on correlation between E and I histograms (5 ms bin size, 1σ Gaussian smoothing; central column). **G3:** Fourier analysis of spontaneous activity for the 59 non-bursting simulations. **H:** Activity in flat space over seven consecutive 100 ms windows. Activity smoothed (Gaussian kernel, $\sigma = 1 pixel$). **I:** Left: Correlation r-value between the histograms of layer-wise E and I populations for the 59 non-bursting simulations. Right: $R_{C/U}$ by population for the 59 non-bursting simulations. **J:** Top: The mean *node participation* of E and I populations in each layer for dimension one (left) and six (right) vs. $R_{C/U}$ for the parameter combination $[Ca^{2+}]_o = 1.05$ mM, $R_{OU} = 0.4$ and $P_{FR} = 0.3$. Markers as in C. Line shows linear fit. Bottom: Correlation r-values between mean node participation and $R_{C/U}$ when neurons with highest node participation are not included in the calculation of mean node participation (via a sliding threshold).

synapses per neuron assuming a total density of E synapses of 1.1 synapses/μm, based on mean spine densities (Larkman, 1991; Datwani et al., 2002; Kawaguchi et al., 2006), and subtracting the number of synapses present in the model. We confirmed a strong correlation between this measure and required conductance injection (Figure 4F).

2.5 *In vivo*-like spontaneous activity

Histograms of spontaneous activity for two meta-parameter combinations are shown in Figure 4G1 (and for all combinations in Video 1). The two combinations have the same population firing rates ($P_{FR} = 0.9$) but the first simulation uses a higher R_{OU} and lower synaptic transmission reliability ($[Ca^{2+}]_o$). In the second simulation, we found larger fluctuations, correlated between E and I populations across layers. Overall, increasing $[Ca^{2+}]_o$ and P_{FR}, and decreasing R_{OU}, increases the amplitude of correlated fluctuations (Video 1; Figure 4G2) and increases power at lower frequencies (Figure 4G3). This supports the notion that decreasing R_{OU} or increasing $[Ca^{2+}]_o$ shifts the model along a spectrum from externally (noise) driven to internally driven correlated activity.

We confirmed that spontaneous firing rate distributions were long-tailed with peaks below 1 Hz for all of the meta-parameter combinations, in line with *in vivo* activity (Figure S3). In the horizontal dimensions, under higher correlation regimes, fluctuations are spatially coordinated and global within the central hexagon of the simulated subvolume (Figure 4H; Video 2). In depth, the size of fluctuations and level of correlated activity increases from supragranular to infragranular layers (Figure 4G1, I, left; Video 1), suggesting that activity in deeper layers of the model is more internally driven. We characterized the effect of recurrent connectivity by measuring the layer-specific decrease in firing rates when neurons in the model are disconnected from each other. As expected, we found that the effect (quantified by the ratio between connected and disconnected firing rates: $R_{C/U}$) increased from supra- to infragranular layers (Figure 4I, right).

2.6 High-dimensional connectivity motifs predict layer-wise spontaneous activity

By analysing the underlying network structure, we observed a corresponding gradient in the topology of intra-layer synaptic connectivity from supra- to infragranular layers. We calculated the mean *node participation* of neuron populations in various dimensions (see STAR*Methods; Figure 4J, top). For dimension one, this is simply the degree of a neuron; for dimensions above one, this generalizes the notion to counting participation in dense, directed motifs of increasing size (*directed simplices*; Reimann et al., 2017). We found that correlations of this measure with the ratio of connected and disconnected firing rates increased with dimension (Figure 4J, bottom, 100% of data), indicating the importance of large directed simplices in shaping activity. Curiously, the correlations for higher dimensions were driven by a small number of neurons with a very high node participation. This was indicated by a sharp drop of correlation when neurons above a given value were excluded (Figure 4J, bottom). This demonstrates high variability between neurons, in line with biology, both structurally (Towlson et al., 2013; Nigam et al., 2016) and functionally (Wohrer et al., 2013; Buzsáki and Mizuseki, 2014).

2.7 Stimulus-responses reproduce *in vivo* dynamics with millisecond-scale precision

We compared stimulus-responses with *in vivo* barrel cortex responses to both *single whisker deflections* and *active whisker touches* under anaesthetized (Reyes-Puerta et al., 2015) and awake states (Yu et al., 2019) respectively. While the model is of non-barrel somatosensory regions, this nevertheless provides validations of overall excitability and the laminar structure of responses reflecting general trends of cortical processing. We activated a percentage (F_P) of the VPM fibers projecting to the central column of the seven column subvolume (Figure 5A1). For each selected thalamic fiber, spike times were drawn from VPM PSTHs (peristimulus time histogram) recorded *in vivo* for the two stimulus types (Figure 5A2; STAR*Methods). For both stimulus types, a single thalamic stimulus was presented 10 times at 1 s intervals at three intensities ($F_P : 5\%, 10\%, 15\%$).

For the parameter combination $[Ca^{2+}]_o = 1.05\,\text{mM}$, $R_{OU} = 0.4$, $P_{FR} = 0.3$ and $F_P = 10\%$, E and I populations in each layer show clear responses on each trial (Figure 5B; three trials shown), except for L1. Videos 3 and 4 show all simulated combinations of the four meta-parameters. Out of 72 parameter combinations, 21 passed an initial assessment of *in vivo* similarity to the *in vivo* data based on latencies and decays (see STAR*Methods, Figure 5C; Figure S4). Responses remained localized to within $600\,\mu m$ of the stimulus location (Figure 5D, Video 5). *In vivo*, layer-wise I populations precede the corresponding E populations and response latencies increase with distance from thalamus, except for the fast response of L4 I. The latencies and decays are matched by criteria passing simulations (Figure 5C, E, left), except for a longer L4 I latency, and shorter and longer sustained responses of L2/3 E and L4 E. PV+ and Sst+ subpopulations respond reliably in layers 2-6, but the 5HT3aR+ subpopulation responses are weaker and less reliable (Figure S4). Under the active whisker touch paradigm, PV+ latencies precede Sst+ latencies *in vivo*, and either precede or are simultaneous with Sst+ latencies *in silico* (Figure 5E, right).

The passing parameter combinations form a contiguous region in the parameter space (Figure 5F), characterized by combinations of low P_{FR}, $[Ca^{2+}]_o$ and F_P with higher R_{OU}, which displayed weakly correlated spontaneous activity (compare Figure 5F with Figure

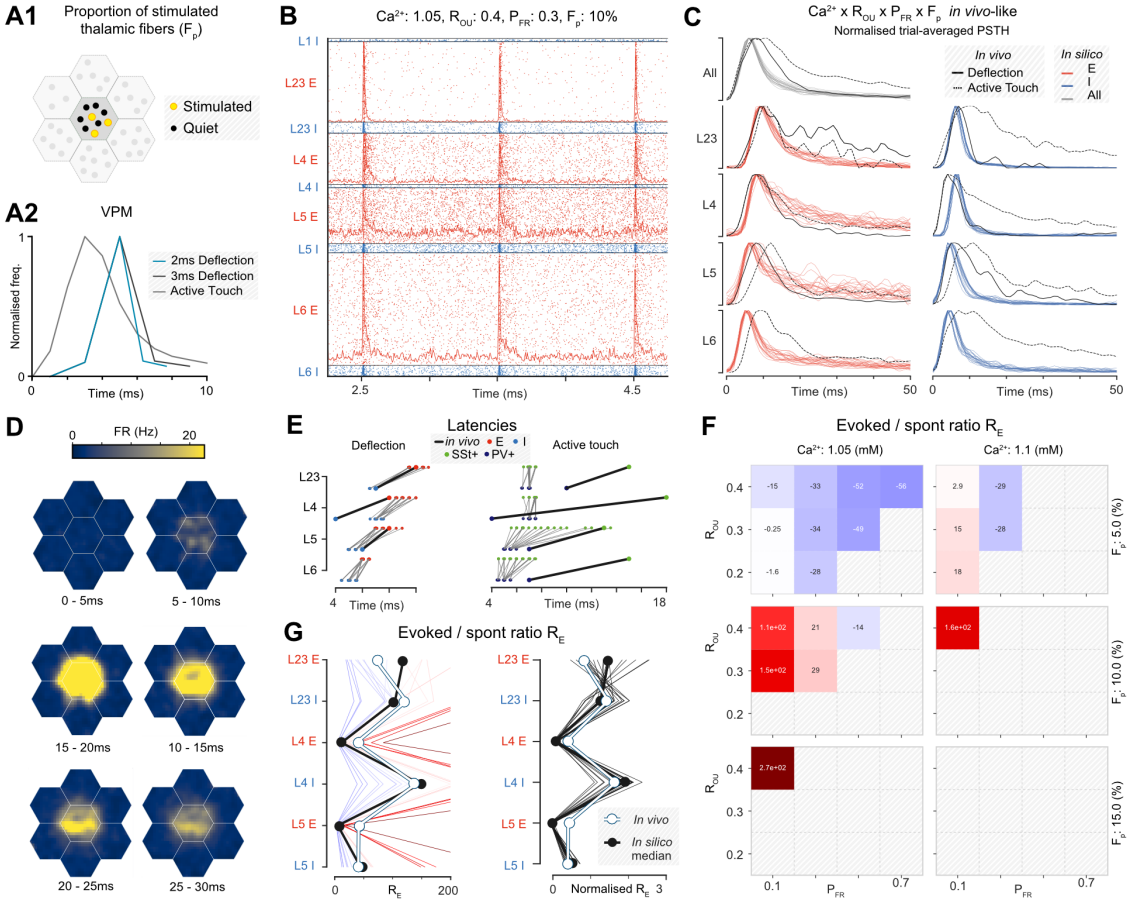

Figure 5: Layer-wise population responses to single whisker deflection and active whisker touch stimuli closely match *in vivo* millisecond dynamics and response amplitudes. A1: Stimuli are simulated by activating a proportion (F_P) of fibers projecting to the central hexagon of the seven column subvolumne. **A2:** Each fiber is assigned a spike time from a PSTH of VPM activity recorded *in vivo* for either a single whisker deflection or active whisker touch paradigm. **B:** Spiking activity and histograms (baseline and max normalised) for each layer-wise E and I population for the parameter combination $[Ca^{2+}]_o = 1.05\,\text{mM}$, $R_{OU} = 0.4$, $P_{FR} = 0.3$ and $F_P = 10\%$ for a 2.5s section of the 10 whisker deflection test protocol. **C:** Trial-averaged PSTHs (baseline and max normalised) in response to the single whisker deflection stimulus for all of the parameter combinations which passed the initial criteria, and the *in vivo* references. **D:** Spatiotemporal evolution of the trial-averaged stimulus response in flat space for the same parameter combination in B. **E:** Left: Latencies of different layer-wise E and I populations for all criteria passing combinations in response to single whisker deflection stimuli. Right: Latencies for inhibitory interneuron subpopulations in response to active whisker touch stimuli. Correponding *in vivo* references are shown. **F:** Heatmap showing the effect of the meta-parameters on the difference of R_E for the entire central column from the corresponding *in vivo* reference. Parameter combinations which failed the criteria tests are masked. **G:** Left: Ratio R_E between maximum evoked response and spontaneous baseline activity by population. One line per simulation. Simulation line colour shows the difference of R_E for the entire central column from the corresponding *in vivo* reference (color values shown in G). Thick black line shows median of *in silico* values. White shows *in vivo* reference. Right: Normalised ratios of each simulation by dividing by R_E for the entire central column.

4G2). This offers a prediction that true *in vivo* firing rates are within the range of these lower FRs. The remaining results apply to the criteria passing simulations. We characterized the magnitude of responses by R_E, the ratio between the peak of the evoked response

and the pre-stimulus baseline activity level. Assuming that extracellular sampling biases are similar during spontaneous and evoked activity, R_E provides a bias-free metric for comparing response magnitude with *in vivo*. Decreasing R_{OU} and P_{FR}, and increasing $[Ca^{2+}]_o$ and F_P led to a global increase of R_E, and results matched *in vivo* closely for a large part of the parameter space (Figure 5F).

Interestingly, the parameter combination closest to *in vivo* was central in the parameter space of criteria passing simulations (Figure 5G, left). Values of R_E, normalized by the mean R_E across populations, were remarkably constant (Figure 5G, right), indicating that variation of the parameters provides a global scaling of response magnitude. Moreover, I populations matched the *in vivo* reference closely, while the responses of L2/3 E were slightly greater, and for L4 E and L5 E slightly weaker. The region of the parameter space where responses match *in vivo* for the active whisker touch stimulus was the same as for single whisker deflections (Figure S5). Latencies were also similar to *in vivo*, with the main discrepancy being slower responses in L4 (E and I). With respect to the meta-parameters, we found that the best match for the anesthetized state was characterized by lower firing rates (P_{FR}) and reduced external noise levels (lower R_{OU}) compared to the awake active whisker touch paradigm (white areas in Figures 5F and S5B). These results fit expectation for anaesthetized and awake states respectively, and provide predictions of their spontaneous firing rates, noise levels and corresponding *in silico* regimes.

Response sparsity (i.e. the proportion of neurons spiking at least once following a stimulus) varied across populations and meta-parameter combinations, but was around the range of 10-20% reported *in vivo* in the barrel cortex (Barth and Poulet (2012); Figure S4D). Interestingly, excitatory population responses were sparser than the corresponding inhibitory layer-wise populations across layers. The observed heterogeneous layer-wise population sparsities offer a prediction for *in vivo*. Moreover, the majority of responding cells spike only once to single whisker whisker deflections (Figure S4E), as reported *in vivo* (Isbister et al., 2021).

2.8 Validation and prediction through reproduction and extension of complex laboratory experiments using a single model parameterization

Building upon the *in vivo*-like activity states, we combined various simulation techniques to recreate laboratory experiments from the literature (see STAR*Methods). For these experiments, we use the parameter combination: $[Ca^{2+}]_o = 1.05\,\text{mM}$, $R_{OU} = 0.4$ and $P_{FR} = 0.3$, as this combination supports realistic *in vivo*-like responses to the two stimulus types over a range of fiber percentages (F_P).

2.8.1 Exploring the canonical model: layer-wise contributions to L2/3 stimulus-responses

In the canonical model of the cortex (reviewed e.g., in Lübke and Feldmeyer, 2007; Feldmeyer, 2012) information from the thalamus arrives to L4, then propagates to L2/3, from there to L5 (which serves as the main cortico-cortical output layer) and lastly to L6 (which projects back to the thalamus). The coordinated action of all layers of S1 is required for high-level behavioral tasks (Park et al., 2020). As the canonical model is based on the highest layer-wise density of axons, it cannot describe all interactions in the cortex. For example VPM does not only innervate L4, but also the border of L5 and L6, as well as the

bottom of L2/3 (Meyer et al., 2010; Constantinople and Bruno, 2013; Sermet et al., 2019).

To study how L4 contributes to the stimulus preference of L2/3 PCs, Varani et al. (2022) used optogenetic inactivation of L4 PCs during whisker stimulation and quantified the changes in the subthreshold response of L2/3 PCs. They found, that the early phase of the subthreshold response significantly differed from the control condition, if the whisker was deflected in either the most or the least preferred direction (see the top and bottom rows of their Figure 5B, C). From this they concluded that both L4 and VPM contribute to the direction tuning of L2/3 PCs. After reproducing their experimental conditions *in silico* (Figure 6A-D; see STAR*Methods) we confirmed that we can reproduce their results, i.e., subthreshold responses of L2/3 PCs decreased, when L4 PCs were inhibited (Figure 6E for preferred direction whisker stimulation; see STAR*Methods).

We then leveraged our *in silico* setup to study what Varani et al. (2022) could not, because of methodological limitations. In our reading, the authors aimed to test how direct E connections from L4 PCs to L2/3 PCs influence the stimulus representation in L2/3. This connection can not specifically be blocked *in vivo*, instead (95% of) the L4 PC population is inhibited (as well as some lower L3 PCs). In our setup we could selectively block the connection and found almost the same result (compare Figure 6E and F, left). This extends the conclusion of Varani et al. (2022): L4 PCs contribute to the stimulus preference of L2/3 PCs via direct E connections, and not via disynaptic inhibition.

The authors also discussed studying L5 PCs' contribution to L2/3 responses (as a large fraction of L5 PC axons terminate in L2/3), but this is infeasible with current mouse lines. Leveraging our model, we found that L5 contributes much less to subthreshold L2/3 traces than L4 (Figure 6F, right). Extending to other presynaptic layers, we found that the contribution of L2/3 is similar to that of L4, whereas inputs from L6 are negligible (Figure 6F, right). Whilst mouse lines targeting L5 PCs might might arrive soon (which could validate our predictions), blocking L2/3 connections between L2/3 cells without hyperpolarizing the same L2/3 population seems only achievable *in silico*.

2.8.2 Contrast tuning by inhibitory interneuron sub-types under optogenetic activation

Shapiro et al. (2022) compared the modulatory effects of optogenetic activation of interneuron subtypes on contrast tuning of neurons in V1. Whilst visual regions differ from somatosensory regions, the study provided an opportunity to explore the generality of interactions between E and I subpopulations. We therefore created a version of the study *in silico*, presenting spatio-temporally modulated patterns with various contrast levels through the VPM inputs (Figure 7A; see STAR*Methods).

Overall, we found within the single simulated column 228 PCs and 259 PV+ interneurons with robust contrast tuning of their responses (see STAR*Methods). Within spike detection range of a vertically penetrating extracellular electrode (50 μm; Henze et al. (2000); Buzsáki (2004)), we found 15 PCs and 13 PV+ interneurons with robust tuning, which is roughly comparable to the original study (average of 8.2 tuned PCs and 3.0 PV+ neurons per mouse Shapiro et al., 2022). Unlike the original study we found no Sst+ neurons with robust tuning.

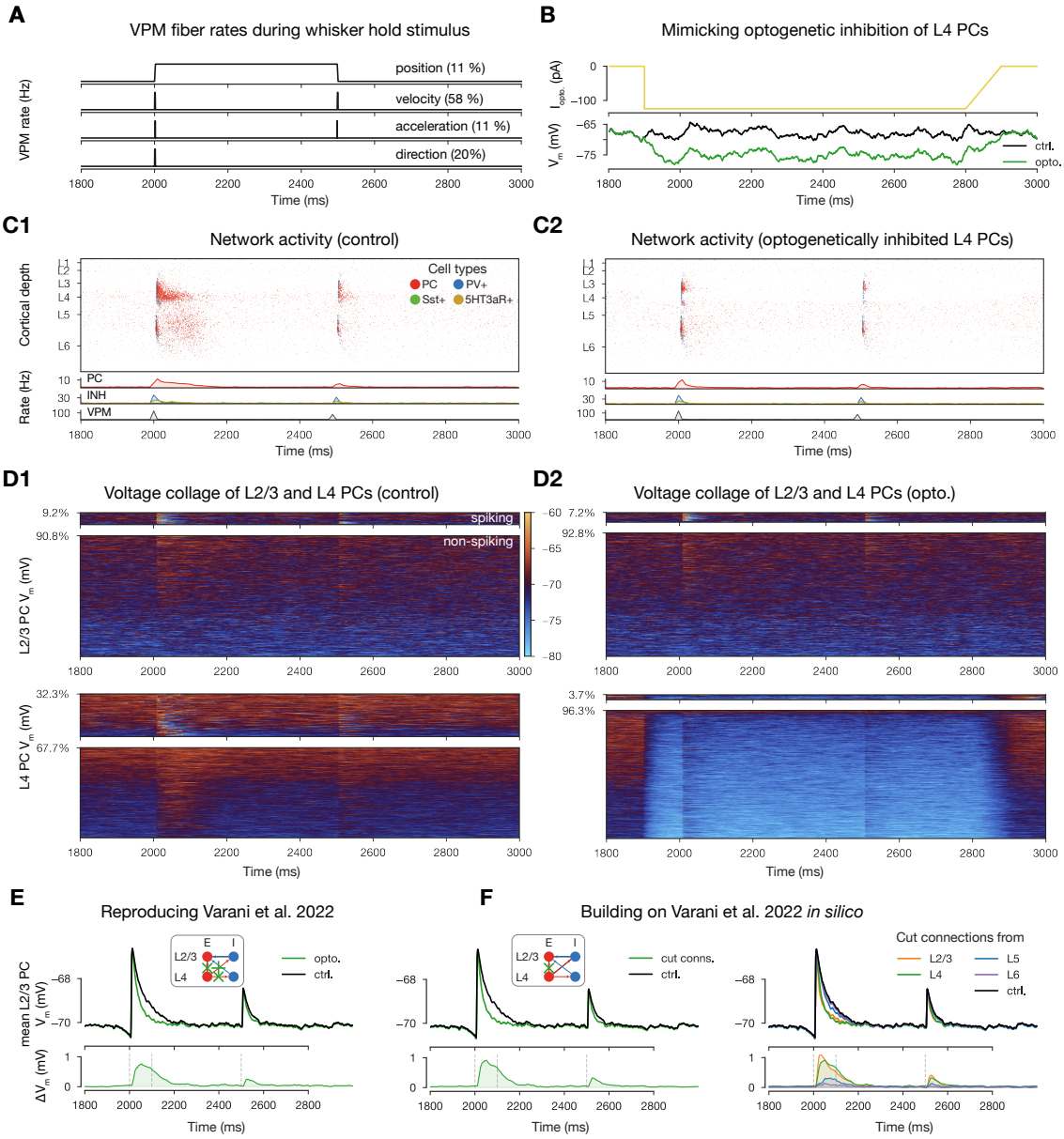

Figure 6: Exploring the canonical model. Reproducing the effect of optogenetic inactivation of L4 pyramidal cells on L2/3 stimulus responses and predicting the role of other pathways through circuit lesions. A: Schematics of whisker kinetics and VPM fiber rates during 500 ms long whisker hold stimulus. Fraction of VPM fibers coding for each kinetic feature are taken from Petersen et al. (2008). **B:** Mimicking the effect of activation of the Halo inhibitory opsin *in silico*. Injected somatic hyperpolarizing current mimicking opsin activation (top), and the resulting somatic voltage trace from a combination of injected conductance, current, and synaptic PSPs from the network (bottom). **C:** Raster plots of the microcircuit's activity and population firing rates below. **C1**: Control conditions, **C2**: 95% of L4 PCs inhibited (by direct somatic current injection depicted in B above, see STAR*Methods). **D**: Voltage traces of all L2/3 (top) and all L4 (bottom) PCs. Panels show spiking traces (top), and subthreshold traces (bottom). **D1** and **D2** depict the same conditions as C above. **E:**: Comparison of average traces from selected L2/3 PCs (see STAR*Methods) in control (black) and optogenetically inhibited (green) conditions. **F:** Same as E, but instead of mimicking the optogenetic inhibition of L4 PCs, only the connections to L2/3 PCs are "cut" (compare inset with the one in E). The right part depicts connections systematically cut from PCs in all layers, while the left shows L4 only for a better visual comparison with the conditions of Varani et al. (2022) in E.

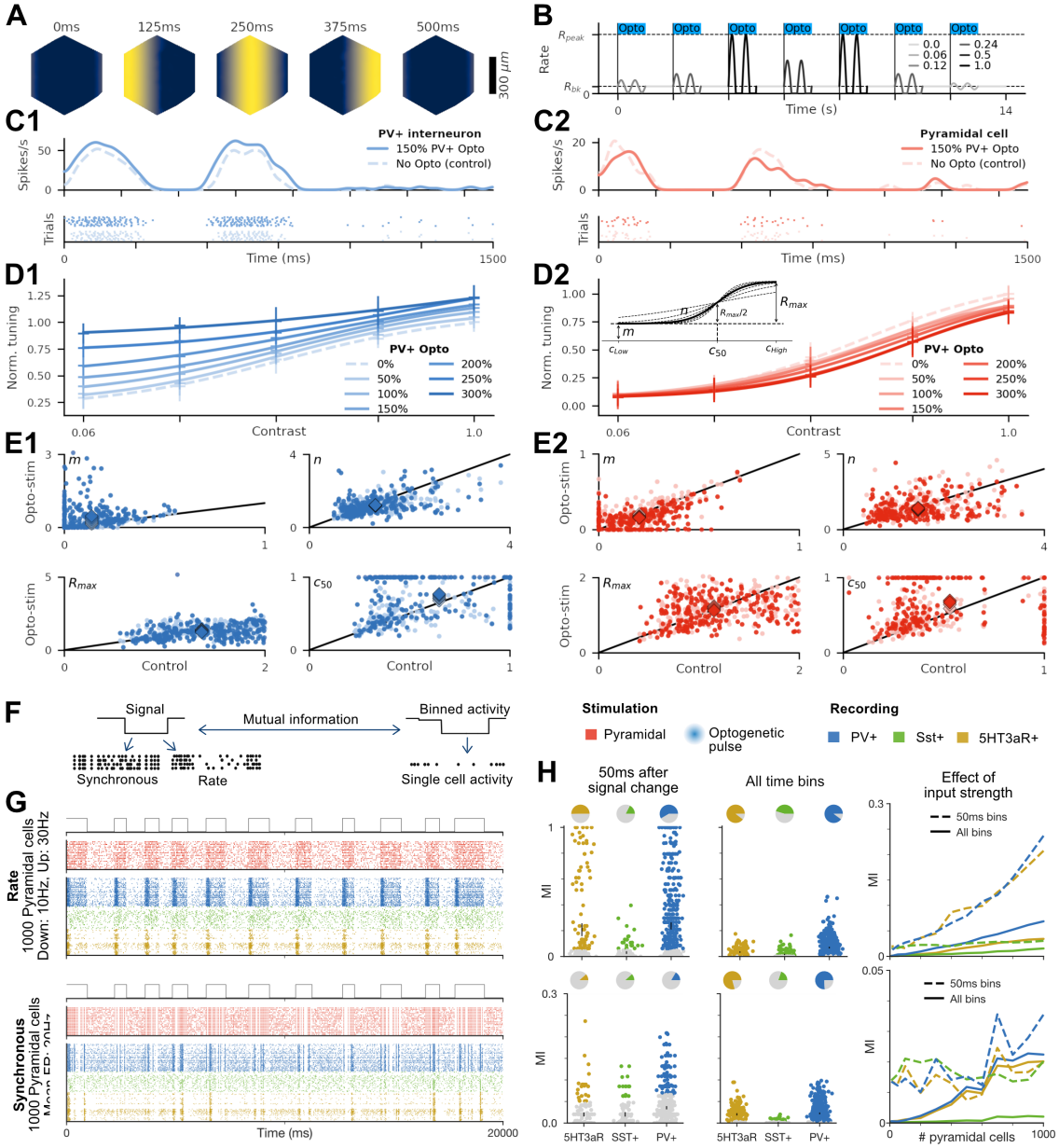

Figure 7: Encoding by interneuron subtypes. Contrast tuning by PV+ interneurons matches *in vivo*, and *in vivo* predictions of encoding of synchronous and rate-coded signals by interneuron subtypes. A: Spatial distribution of firing rates of VPM fibers projecting to a single simulated column at different points in time, corresponding to linear drifting gratings with a temporal frequency of $f_{temp} = 2\,\text{Hz}$ and a spatial frequency of $f_{spat} = 0.001\,\text{cycles}/\mu\text{m}$. **B:** Firing rate signal of a single VPM fiber corresponding to a random sequence of drifting grating patterns with different contrast levels C, as indicated by the legend. All optogenetic stimuli targeting PV+ (or Sst+) interneurons were completely overlapping with the grating stimulus intervals, as indicated by the blue bars. **C1:** Spiking activity and PSTH of an exemplary PV+ interneuron over 10 repetitions (trials) in response to a grating stimulus at maximum contrast ($C = 1.0$) without (control) and with medium strength (150%) optogenetic stimululation. **D1:** Contrast tuning modulation of an exemplary PV+ interneuron by different levels of PV+ optogenetic stimulation, ranging from 0% (control) to 300%. The individual markers denote actual data points (mean ± SD over 10 repetitions, normalized to baseline response at maximum contrast) while curves illustrate sigmoidal fits to these data points.

E1: Scatter plots showing the fitted sigmoidal parameter values in control condition vs. PV+ optogenetic stimulation at lowest (50%) and highest (300%) level respectively for all 259 robustly tuned PV+ interneurons. Diamond markers indicate mean values over neurons, including all optogenetic stimulation levels from 50% to 300%. Colors as in panel D1 legend. **C2/D2:** Same as C1/D1, but for exemplary PCs. **D2 inset:** Illustration of sigmoidal parameters m, n, R_{max}, and c_{50}. **E2:** Same as E1, but for all 228 robustly tuned PCs. **F:** A binary signal is encoded either through changes in the rate or synchronicity of optogenetic pulses applied to a set of PCs. We define a direct correspondence between single optogenetic pulses and single spikes. Spiking activity is measured in PV+, Sst+ and 5HT3aR+ cells, and the mutual information between the binned activity of individual cells and the original binary signal is measured. **G:** Visualization of the rate (upper) and synchronous (lower) coded stimulus experiments stimulating 1000 PCs, showing the binary signal (top), input neuron spike trains for 40 neurons (middle), and responses of the three L2/3 neuron types (bottom). **H: Upper:** Results for the rate coded stimulus experiment. Left: Mutual information between spiking activity and the binary signal (one point for each cell that spiked at least once). Only activity in the 50 ms following the change of the binary signal is considered. Cells with mutual information not significantly different from that of a shuffled control are coloured grey. Centre: Same as left but considering all time bins. Right: The effect of the number of stimulus neurons on the mean single cell mutual information for each subpopulation. **Lower:** The same as upper but for the synchronous stimulus type.

Additionally, we found the following results, all in line with (Shapiro et al., 2022): The firing rates of both PCs and PV+ neurons were affected by optogenetic activation of the PV+ subpopulation (Figure 7C), resulting in changes to the contrast tuning curves of these populations (Figure 7D). The main effect of the optogenetic manipulation was an increase in contrast tuning for PV+ and a decrease for PCs. The tuning curves could be accurately fit by sigmoidal functions ($r^2_{PV+} = 0.995 \pm 0.008$; $r^2_{PC} = 0.990 \pm 0.012$), and consequently the effect of optogenetic activation could be quantified in terms of changes to the fitted parameters (Figure 7D1 inset, E; STAR*Methods). We found great variability between neurons with increasing trends for parameter m in PV+ and c_{50} in PCs, and decreasing trends for R_{max} in PV+ and both m and R_{max} in PCs. Unlike in (Shapiro et al., 2022), we found in addition an increasing trend of c_{50} also in PV+ interneurons (Figure 7E1).

Comparing three abstract mathematical models (Shapiro et al., 2022; STAR*Methods), we found that the saturation additive model best captured the effect of the optogenetic manipulation for PV+ neurons (Figure S8A, B1), as in the reference study. The relative contributions of saturation and addition varied strongly between individual neurons (Figure S8C1). At low intensities of the optogenetic manipulation, this distribution matched qualitatively the results of Shapiro et al. (2022), but at higher intensities we observed a shift towards stronger saturation. Combining the saturation additive model with a simplified, population-level model of PC firing (Shapiro et al., 2022; STAR*Methods) provided a good description of the observations (Figure S8B2) with relative contributions of saturation and addition that qualitatively match the reference (Figure S8C2).

2.8.3 Encoding of synchronous and rate-coded signals by inhibitory interneuron sub-types

Prince et al. (2021) studied how different I subpopulations represent signals that are encoded as changes in the firing rate or synchronicity of PCs (Figure 7F). We repeated their study *in silico* (Figure 7G), but using *in vivo*-like conditions as the authors have suggested in their Discussion. The original study pointed out the importance of mem-

brane properties and short-term dynamics of synaptic inputs onto the subpopulations in shaping the results. Note, that the lower synaptic reliability *in vivo* weakens synaptic depression (Borst, 2010), and the ongoing background input leads to higher membrane conductance (Destexhe et al., 2001); therefore our results are expected to differ substantially, and provide an independent prediction for a different dynamic state. While in the original *in vitro* study stimulation of 10 PCs was sufficient to find a decodable signal, we expected a larger number to be required under our *in vivo*-like conditions, due to the lower $[Ca^{2+}]_o$, and the higher level of noise (see STAR*Methods).

Indeed, we found little discernible mutual information in I spiking for the activation of 10 PCs, but that mutual information increased with the number of activated neurons (Figure 7H, right). For 1000 activated neurons each of the three I subpopulations in L2/3 showed clear but qualitatively unique modulation for both encoding schemes (Figure 7G). As in (Prince et al., 2021) we found differences in the encoding capabilities of the I subpopulations (Figure 7H). We found strongest encoding in PV+ neurons for both schemes, and overall low encoding strength in Sst+ neurons. Further, we found overall low amounts of mutual information for the synchronous stimulus, which is in line with Prince et al. (2021), as they linked encoding of that stimulus to depressing synaptic dynamics, which would be weakened *in vivo*.

2.9 Long-range connectivity determines independent functional units and selective propagation of stimulus-responses at larger spatial scales

After calibrating the model of extrinsic synaptic input for the seven column subvolume, we tested to what degree the calibration generalizes to the entire nbS1. Notably, this included addition of long-range connectivity (Reimann et al., 2022a). The total number of local and long-range synapses in the model was 9138 billion and 4075 billion, i.e., on average full model simulations increased the number of intrinsic synapses onto a neuron by 45%. Particularly, the final $\phi_{1.05,0.4}$ calibrated for the seven column subvolume was used in conjunction with $P_{FR} \in [0.1, 0.15, ..., 0.3]$. Each of the full nbS1 simulations (using $[Ca^{2+}]_o = 1.05\,\text{mM}$ and $R_{OU} = 0.4$) produced stable non-bursting activity, except for the simulation for $P_{FR} = 0.3$, which produced network-wide bursting activity.

Activity levels in the simulations of spontaneous activity were heterogeneous, ranging from a mean firing rate of 0.15 Hz to 0.3 Hz (when activity was averaged in flat space for $P_{FR} = 0.15$; Figure 8A1; Video 6). The subregion with consistently higher firing rates was the upper-limb representation (S1ULp), separated from subregions of lower activity by the dysgranular zones (S1DZ, S1DZO). This demonstrates that the larger spatial scale of the model supports several independently acting functional units. Locations with higher firing rates were accompanied by higher spiking correlations of the local population (Figure 8A2), indicating activity that was more driven by intrinsic excitation. Unlike in the simulations of smaller volumes, the correlation emerged mostly from short, transient packets of activity in L6 (Figure 8B). Consequently, deviation from the target P_{FR} in those cases was largest in L6 (Figure 8C). Taken together, it appears as if the additional synapses from long-range connectivity moved the model along the spectrum from extrinsically vs. intrinsically driven, but further for some regions than for others. We confirmed a divergence into two populations: one with correlation slightly increased from the simulations of smaller volumes, and one with almost maximal correlations (Figure 8D). This distinction

was determined mostly in L6 with increases of correlations in other layers remaining small.

We repeated the previous single whisker deflection evoked activity experiment in the full model, providing a synchronous thalamic input into the forelimb sub-region (S1FL; Figure 8E; Video 7). Responses in S1FL were remarkably similar to the ones in the seven column subvolume, including the delays and decays of activity (Figure 8F). However, in addition to a localized primary response in S1FL within 350 μm of the stimulus, we found several secondary responses at distal locations (Figure 8E; Video 7), which was suggestive of selective propagation of the stimulus-evoked signal to downstream areas efferently connected by long-range connectivity. The response of the main activated downstream area (visible in Figure 8E) was confined to L6 (Figure 8G).

As the model is homogeneous across the different subregions in terms of neuronal morphologies and physiology, we expected the differences in spontaneous and evoked activity across the model to be explained by the topology of synaptic connectivity (Reimann et al., 2022a). While the extrinsic input from the OU injections was uncorrelated by design, synaptic input from local connectivity would feature at least some degree of correlation. This led to asking, how correlated was the input from long-range connections? We estimated for each pair of long-range connections innervating a 460 μm hexagonal subvolume its spiking correlation and compared the resulting distribution to the correlation within the subvolume itself (see STAR*Methods; Figure 8H, upper). We found low correlations for most pairs, but with a significant number of high-correlation outliers for subvolumes with high internal correlations. Moreover, when we considered the mean of the measure, we found that it explains most of the variability in internal correlations, for both spontaneous (Figure 8H, lower) and evoked states (Figure S9).

This led to the following tentative explanation: Local connectivity provides inputs from within 500 μm, which is virtually guaranteed to be correlated to some degree (Figure 8I upper vs. lower, orange). This is a result of connections being *locally dense*, as they are concentrated within a small neighborhood (Figure 8 lower, green vs. orange). Long-range connectivity originates from further away, sampling from different functional units that may or may not be correlated, and being more diluted (Figure 8I lower, green vs. blue). Consequently, long-range inputs are likely to act not much different from the uncorrelated OU process, unless this is overcome by a non-random topology of long-range connectivity.

Specifically, we considered the long-range connectivity at meso-scale in terms of the graph of synapse counts between 460 μm subvolumes. When the graph was thresholded at eight million synapses, most subvolumes lacked connections at that strength completely, but others formed a single connected component, indicating the formation of a *rich club* (Colizza et al., 2006; Figure 8J, upper, red and orange). We found that subvolumes with high internal correlation were part of the rich club, or directly adjacent to one of its members (Figure 8J). In the presence of strong thalamic inputs, this could be overcome, as the increased activity level spread along sufficiently strong long-range connections (Figure 8K), albeit with substantial delays between 60 and 100 ms. This could induce high correlations in strongly connected parts of the model, outside the rich club as well (Figure S9) and shows that the model supports selective propagation of activity to areas efferently connected with long-range connectivity.

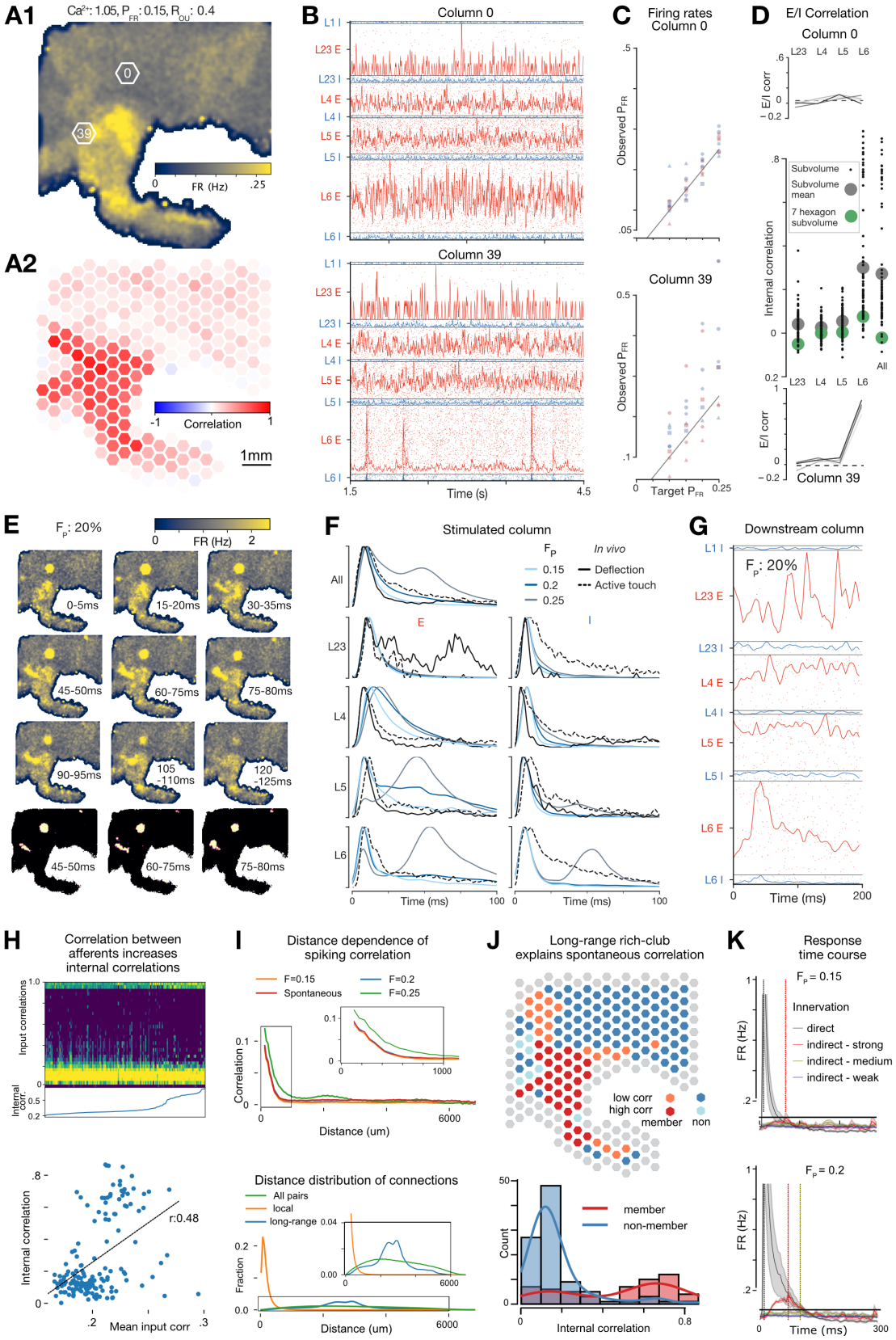

Figure 8: Full nbS1 simulations: independent functional units, millisecond-precise stimulus-responses, selective propagation of stimulus-evoked activity through long-range connectivity, linking structure to function. Caption on following page.

A1: Mean FRs across the model. Columns 0 and 39 (subsequently used) are highlighted. **A2:** Spiking correlations of E/I populations in 240 hexagonal subvolumes (diameter: $\approx 460\,\mu m$). **B:** Spiking activity and max normalised histograms for layer-wise E and I populations for the parameter combination in A, and the 0th (upper) and 39th (lower). **C:** Target vs. observed P_{FR} values for the four non-bursting simulations. The number of sides of each marker corresponds to the layer (triangle represents L2/3). Red: E, blue: I.. **D:** Correlations between E and I populations by layer for the four non-bursting simulations for the two hexagons (top and bottom). Color of line from light to dark represents P_{FR}. Middle: Distributions of spiking correlations of layer-specific populations in columns ($520\,\mu m$) of the nbS1 model (black dots; mean values: grey). Compared to the central column when the seven column subvolume is simulated in isolation (green). **E:** Trial-averaged activity in flatspace following single whisker deflections. Lower: Subset of time windows shown with only the top 2% of bins for each time window after baseline activity level subtracted. **F:** Trial-averaged PSTHs (baseline and max normalised) for column 0. For $F_P = 15\%$ and $F_P = 25\%$ respectively, the evoked responses passed and failed the latency and decay-based criteria tests for similarity to *in vivo*. Response for $F_P = 20\%$ passed the tests for all populations except L5 E which showed a more sustained response. **G:** Trial-averaged response of column 39. **H:** Correlations of long-range inputs. Upper: Distribution of spiking correlations of inputs into 240 subvolumes. Calculated at reduced spatial resolution, based on connection counts and correlations between the subvolumes (see STAR*Methods). Subvolumes are sorted by the E/I correlation of neurons within them. Lower: Mean of the correlations of inputs into 240 subvolumes vs internal spiking correlation for all subvolumes during spontaneous activity. Black line: linear fit. Calculated based on connection counts and correlations between $50\,\mu m$ hexagonal subvolumes (see STAR*Methods). Data for evoked activity is shown in Figure S9. **I**: Upper: Spiking correlations of subvolumes against their distances in spontaneous (red) and evoked (orange: $F_p = 0.15\%$, blue: $F_p = 0.2\%$, green: $F_p = 0.25$) activity. For increased spatial resolution, smaller ($58\,\mu m$) subvolumes were used, hence correlation values are not comparable to values in B. Lower: Distribution of soma distances of neuron pairs connected by local (orange) or long-range (blue) connectivity. Green: distances of all pairs, independent of connectivity. **J:** Upper: Classification of subvolumes based on low or high internal correlation and membership in long-range rich club Data for evoked activity shown in Figure S9. Lower: E/I correlation of subvolumes for members of the rich club (red) and non-members (blue). **K:** FRs of subvolumes following a stimulus with $F_P = 0.15\%$ (top) and $F_P = 0.2\%$ (bottom). Mean (lines) and SEM (shaded area) over 10 repetitions shown for subvolumes directly innervated by the VPM stimulus (black), strongly innervated by directly innervated subvolumes (with over 10^6 synapses, red), or by medium strength (over 10^5 synapses, yellow) or weak (over 10^4 synapses) indirect innervation. Dashed lines indicate locations of peaks.

3 Discussion

We presented novel methods to build, simulate and validate models of cortical tissue that correspond directly with 3D digitised brain atlases. As demonstrated, this enables laboratory experiments to have a simulatable *in silico* counterpart, and vice versa: predictions made by the model automatically have a precise correspondence in biology. By recreating and extending five laboratory experiments under a single model parameterization, we provided strong model validation and demonstrated the model's natural versatility. To our knowledge the simulations of the full nbS1 represent the first simulations of stable *in vivo*-like spontaneous and stimulus-evoked activity in a large-scale biophysically detailed model of multiple cortical subregions connected through local and long-range connectivity. The model generated an initial set of predictions about the relationship between cortical structure and function, and provides a basis for future studies and prediction. Through the production of high-quality software, we are able to make the model and simulation tools available for use, enabling community driven testing, exploration and refinement.

We also presented a novel calibration technique, which allows rapid and methodical characterisation and validation emergent model activity. The associated parameters and meta-parameters offer a mathematical notation for complex large-scale biophysically detailed models, that facilitate easy interpretation of large, complex data. Excitation from non-modeled brain regions is modeled by injecting somatic conductances and is calibrated for specific populations. Although abstract relative to the model, the injection amplitudes could be predicted from the number of missing synapses, suggesting it provides a functional representation of their anatomical counterparts. The modular model of extrinsic connectivity can be refined or replaced in the future, or when larger fractions of the brain are modeled. Our approach to obtaining *in vivo*-like activity contrasts with a recent approach in a large-scale biophysical model of primary visual cortex of similar scale to our smaller subvolume (Billeh et al., 2020). There, they delivered extrinsic inputs through dendritic synapses instead of somatic injection, which is more anatomically realistic, and they adjusted intrinsic recurrent weights to match extracellularly recorded firing rates. They find a single activity state, instead of the *in vivo*-compatible spectrum here that allowed us to contrast anesthetized and awake states. The model in general differs from hybrid models, which jointly use biologically-detailed models and point neuron models (Billeh et al., 2020; Dura-Bernal et al., 2023), and also from the work of Egger et al. (2020) who modeled activation of L5 pyramidal cells by constraining patterns of synaptic input based on receptive fields and predicted annatomical innervation.

A region of the parameter space defined by three meta-parameters supported *in vivo*-like responses to single whisker deflections and active whisker touch stimuli, under anesthetized and awake conditions, respectively. Although from the barrel system, these stimuli offer some of the simplest stimulus-response paradigms, enabling principles of neural dynamics and information processing to be studied; in particular, the correspondence between atomic units of sensory information and neural representations. Such validations are crucial for complex models, as they provide context for more complex validations. If a model reproduces properties of neural activity in more complex experimental paradigms, but not for simpler ones, it would suggest that the model acts in a regime different from biology. Moreover, in a rich and complex nonlinear system, the source of discrepancies with *in vivo* activity are simpler to ascertain under simpler protocols. The model also predicts the number of thalamic fibers stimulated for both stimuli. Responses were closer to biology for values of the P_{FR} meta-parameter between 0.1 and 0.3, according with the known inflation of mean firing rates stemming from the bias of extracellular spike sorting techniques towards larger and more active neurons (Olshausen and Field, 2006).

Supporting our estimates, patch-clamp experiments show ubiquitous neuronal silence (Crochet and Petersen, 2006), and spontaneous and stimulus-evoked barrel cortex firing rates as much as 10 times lower than for extracellular recordings (0.05-0.15 Hz vs. 0.8-1.5 Hz; Olshausen and Field, 2006). Each recording technique comes with challenges and biases (Shoham et al., 2006; Olshausen and Field, 2006; Barth and Poulet, 2012; Wohrer et al., 2013). Calcium imaging and patch-clamp experiments are less biased towards frequently spiking neurons (Wohrer et al., 2013), yet the former can only infer spiking activity and may be biased towards neurons that favour marker expression. Patch-clamp techniques can reduce firing rates, be biased towards larger or more active neurons (Olshausen and Field, 2006); and are limited to recording a few neurons simultaneously, preventing characterizations of single trial population dynamics. An earlier version of the model has been used to simulate cortical extracellular potentials (Reimann et al., 2013).

We can now simulate modern extracellular electrodes and compare spike sorting results to the *in vivo*-like ground truth. The model's large scale also ensures contributions of distal neurons to the signal. Comparison of firing rates of multi-unit activity could also be made.

Given the complications of elctrophysiological recording, how can we be confident that the model's activity is *in vivo*-like? First, we demonstrated correlated spontaneous dynamics in the form of global and local fluctuations and dynamic E-I balance, as found experimentally (Renart et al., 2010). Second, population firing rate distributions were long-tailed with sub 1 Hz peaks, and were similar for spontaneous and stimulus-evoked activity, as reported (Wohrer et al., 2013). Moreover, mean firing rates below 1 Hz are required by metabolic constraints (Attwell and Laughlin, 2001; Lennie, 2003). In response to simple whisker stimuli, response sparsity, spike counts, and the temporal profile and amplitudes of layer-wise populations were similar to *in vivo*. The effect of the spontaneous meta-parameters on evoked responses, also shows that the networks spontaneous state affects stimulus-responses, as observed *in vivo* (Isbister et al., 2021).

The calibration of extrinsic inputs approximates the relationship between unconnected and connected firing rates for different populations. The calibration technique simplifies this highly complex problem by approximating it for states where firing rates are a constant proportion of reference rates. The number of iterations was reduced by starting with a calibration from a related model. The ability to change an aspect of the model and quickly recalibrate the network, could be applied in many other settings, for example, when a different brain region is connected to the model. The efficiency of the optimisation process is critical, given the large computational cost of simulations. Connected divided by unconnected firing rates are also a prediction of the degree to which the activity of a population is determined by incoming connections from local sources. We found an increase of the importance of local connectivity from superficial to deeper layers. This is largely in line with the canonical view of the cortex (Lübke and Feldmeyer, 2007; Feldmeyer, 2012), which places layers 5 and 6 at the end of local (i.e., intra-columnar) information flow.

It is important to highlight where the model deviates from biological data. For example, the timing of inhibitory subpopulation responses were not reproduced. Furthermore, the model omits several known anatomical elements, such as glia and the presence of gap junctions between certain neuron-types, but the model's spatial context provides a natural scaffold for them. Some shortcomings indicate a lack of available data. For example, the physiological strength of thalamic inputs onto many cortical populations remain unclear as the best available data mixes structural and physiological strength (Sermet et al., 2019). Our modeling techniques assume generality of rules and parameters, unless indicated by the data. Therefore, violations indicate specific biological rules. For example, model thalamic inputs innervate any dendrite placed in the targeted layers equally. The delay of responses of PV+ and Sst+ neurons in layer 4 could be adjusted to match the biological data better by biasing innervation towards PV+ dendrites. As stated, the model's release will allow the community to identify further data-model mismatches, reveal gaps in current understanding, and drive furtherrefinements.

During spontaneous activity, we found emerging spatial inhomogeneities in network activity. Specifically, we observed sharp transitions in firing rates and pairwise correlations

at disgranular zones. This highlights that the model supports several, independently acting functional units. Analysis of spatial correlations suggests a radius of approximately $400\,\mu m$ for a single unit. This property was not present in the previous intra-regional scale model (Markram et al., 2015), but is rather an emergent property of the interregional scale, demonstrating that we achieved our goal of building a model that can be used to study long-range interactions between regions. Analyzing the source of the inhomogeneities suggested a prominent role of a non-random rich-club structure of long-range connections at the meso-scale. Within functional units, we found that inhomogeneous increases of spiking correlations were confined to spontaneous packets of L6 activity.

In addition to demonstrating close similarity with *in vivo* whisker-stimulus responses, we reproduced protocols from three more complex laboratory experiments. These experiments used a wide array of techniques, which could be accurately recreated due to the model's close correspondence with biological tissue. Additionally, we could go beyond the original experiments. For example, we predicted an increased number of neurons would be required to have a decodable effect on postsynatic activity under *in vivo* conditions over the *in vitro* conditions of the original experiment. This can be explained by lower synaptic reliability under *in vivo* conditions. This demonstrates that the approach of modeling entire brain regions can be used to further probe the topics of the original articles and cortical processing. For example, demonstrating selective propagation of stimulus-evoked activity to downstream areas, and the long-rage interactions shaping local activity correlations, allows the simulation-based study of processing in cortical hierarchies in more complex setups. For example, the integration of multiple stimuli applied to distal parts of the model could be studied. Studying activity in more complex paradigms at large spatial scales may also allow us to characterize expected correlations and replace statistically independent input compensation with more specific conductance injections.

The model provides an opportunity to study plasticity under *in vivo*-like conditions at the level of interacting regions and beyond pairs of neurons (Markram et al., 1997b; Larsen and Sjöström, 2015). In an earlier version of this model, we implemented a plasticity rule that captures the roles of calcium and dendritic integration in plasticity (Chindemi et al., 2022). We can now bridge these scales to understand learning in cortical hierarchies.

Acknowledgements

The authors would like to thank Fabien Delalondre, Adrien Devresse, Hugo Dictus, Juan B. Hernando, Nicolas Cornu, Daniel Fernandez, Jeremy Fouriaux and Ioannis Magnakaris for helpful discussions and contributions to the model; Eva Kenny for help with project management; Cyrille Favreau, Marwan Abdellah and Nadir Roman for support with graphics and figure design and Karin Holm and Akiko Sato for support of manuscript development and helpful discussions. The authors would also like to thank Heiko Luhmann, Vicente Reyes Puerta and Jhy-Jung Sun for supporting access to data used in the primary validation of the model.

Funding

This study was supported by funding to the Blue Brain Project, a research center of the École polytechnique fédérale de Lausanne (EPFL), from the Swiss government's ETH Board of the Swiss Federal Institutes of Technology.

Author contributions

In alphabetical order under each point.

- Conceptualization: H.M., E.B.M., S.R., M.W.R.
- Data curation: S.B.P., A.E., W.V.G, J.B.I, D.M., S.R., R.R., M.R., A.T.
- Formal analysis: A.A., S.B.P., J.B.I., A.E., D.E.S., P.L., C.P., M.W.R., M.R, C.R., V.S., A.T., W.V.G.
- Investigation: S.B.P., A.E., D.E.S., J.B.I., P.L., C.P., M.W.R.
- Methodology: S.B.P., N.B.Z., D.E.S., A.E., J.B.I., P.L., D.M., C.P., M.W.R., M.R., A.R., A.T., W.V.G.
- Project administration: J.D.C., J.K., S.L., H.M., J.P., A.R., S.R., M.W.R., F.S.
- Resources: J.D.C., M.G., W.J., P.K., J.K., P.K., F.P., F.S.
- Software: A.A., O.A., J.B.A., J.D.C., T.Da., T.De., G.F., M.G., J.H., G.I., W.J., J.K., P.K., F.P., M.W.R., V.S., A.T., M.W.
- Supervision: H.M., S.R., M.W.R.
- Validation: A.A., N.B.Z., S.B.P., G.C., A.D., A.E., M.G., J.B.I., D.K., C.P., M.W.R., M.R., V.S., W.V.G.
- Visualization: E.B., S.B.P, A.E., D.E.S., J.B.I., J.P., C.P., M.W.R.
- Writing - original draft: S.B.P, D.E.S., A.E., J.B.I., C.P., M.W.R., M.R.
- Writing - review & editing: S.B.P., D.E.S., A.E., J.B.I., D.K., C.P., S.R., M.W.R., V.S.

Declaration of interests

The authors declare no competing interests.

4 STAR*Methods

Key resources table

REAGENT or RESOURCE	SOURCE	IDENTIFIER
Deposited data		
Raw neuron recordings	Reva et al.	bbp.epfl.ch/nmc-portal/downloads.html
Neuron morphology reconstructions	Reimann et al.	10.5281/zenodo.6906785
Raw paired recordings	Markram et al.	bbp.epfl.ch/nmc-portal/downloads.html
PSP amplitudes	Sources as listed in	Table S4
CV of PSP amplitudes	Sources as listed in	Table S5
mPSC frequencies	Sources as listed in	Table S6
Spont. and evoked spiking freq.	Reyes-Puerta et al.	from original authors on request
VPM spike trains	Diamond et al.	digitized from Figure 8
	Yu et al.	from original authors on request
Volumetric atlases	Bolaños-Puchet et al.	10.5281/zenodo.7930276
Ion channel models	Reva et al.	10.5281/zenodo.7930276
Anatomical model	Reimann et al.	10.5281/zenodo.6906785
Models of neuron electrical types	Reva et al.	10.5281/zenodo.7930276
Anatomical and physiological model	This paper	10.5281/zenodo.7930276
Software and algorithms		
Electrical model optimization	Reva et al.	github.com/BlueBrain/singlecell-emodel-suite
Simulation software	This paper	10.5281/zenodo.8075202
Model loading and interaction	This paper	10.5281/zenodo.8026852
Model and simulation analysis	This paper	10.5281/zenodo.8016989
Specific simulation configurations	This paper	10.5281/zenodo.7930276

Resource availability

Lead contact

Further information and requests for data and code should be directed to and will be fulfilled by the lead contact: Michael W. Reimann (michael.reimann@epfl.ch)

Materials availability

No materials were used in this computational work.

Data and code availability

- Neuron morphology reconstructions, ion channel models, neuron electrical models, volumetric atlases, and the description of the model in SONATA format (Dai et al., 2020) have been deposited at Zenodo and are publicly available as of the data of the publication. The DOI is listed in the key resources table. Raw single cell recordings and paired synaptic recordings have been deposited in the Blue Brain portal and are publicly available as of the date of publication. The links are listed in the key resources table.

- All original code has been deposited at Zenodo and is publicly available as of the date of publication. DOIs are listed in the key resources table.

- Any additional information required to reanalyze the data reported in this paper is available from the lead contact upon request.

4.1 Method details

4.1.1 Optimisation of ion channel conductance densities

Neuron models from Reva et al. (2022) were made as follows. Ion channel conductance densities were optimised for a pool of reconstructed neurons, for which *in vitro* recordings had previously been made. Ion channel densities were then generalised to other neuron models of the same e-type. Resulting neuron models were only used in the construction of the model if the value of the cost function was within 5F standard deviations of the experimental mean.

4.1.2 AIS Adjustment

For some electrical models, further adjustments were made to AIS sections to handle the large input currents present under conditions of high network activity. In short, for certain pyramidal cell morphologies, the AIS was replaced by a cylinder with a length of $60\,\mu m$. Its diameter was manually calibrated such that the ratio of the AIS input resistance over the input resistance of somato-dendritic compartments was equal to 2. Afterwards, it was confirmed that the cost function of their electrical models remained below the threshold.

4.1.3 Parametrization of synaptic physiology

Synapse physiology parameters were taken from the literature, and after eventual corrections (for differences in the solutions used in the experiments), were put directly into the model using the technique described for the use case of hippocampal CA1 in (Ecker et al., 2020). For the parameterization of cortico-cortical synaptic physiology, paired-recording data sources from Markram et al. (2015) were re-used. To further constrain the variance of EPSP amplitudes in L5 TTPCs, fitted parameters from Barros-Zulaica et al. (2019) were used. The dataset was also enriched with recent recordings from L6 (Qi and Feldmeyer, 2016; Yang et al., 2020, 2022). Instead of generalizing L4 E peak synaptic conductances for all thalamic fibers (as in Markram et al., 2015), synaptic conductances were constrained using EPSP amplitude measurements from thalamocortical slices (Beierlein and Connors, 2002; Beierlein et al., 2003). Fibers originating from POm were not present in Markram et al. (2015). Due to the lack of *in vitro* measurements, physiological parameters from VPM synapses were generalized to describe POm synapses.

Not all synaptic peak conductances can be measured with paired recordings due to the space-clamp artifact (Markram et al., 2015; Ecker et al., 2020), and estimating the number of release-ready vesicles is also challenging experimentally (Loebel et al., 2009; Barros-Zulaica et al., 2019). Thus, for synaptic pathways for which there was *in vitro* reference data, these two parameters were determined in a simulation-driven iterative process. Firstly, 50 pairs of *in silico* neurons were randomly sampled. Second, the postsynaptic cell was current-clamped, and the PSP at the soma of the postsynaptic cell in response to a presynaptic action potential was measured. This was repeated 35 times for each pair as in Ecker et al. (2020). Thridly, the mean and the CV of these amplitudes were extracted and compared with reference *in vitro* data. Finally, peak conductance ($\hat{g}$), and the average number of vesicles in the release-ready pool (N_{RRP}) were adjusted to

match the amplitude and CV of the *in vitro* reference (Ecker et al., 2020). In some cases, this resulted in reaching the lower bound of univesicular release (Barros-Zulaica et al., 2019).

Where experimental data was not available, mean synaptic physiology parameters from similar pathways were used (Markram et al., 2015; Ecker et al., 2020). For the VPM to L5 E pathway, the maximum of VPM to L4 E and VPM to L6 E conductances (instead of the mean) were used, based on resulting evoked firing rates found in a later modeling step (Figure S4C). To calibrate the mPSC frequencies of different pathways, single cell simulations with different values of the spontaneous release frequency for all synapses of a set of 1000 cells in a given pathway were run. In these simulations, *in silico* voltage-clamp recordings were performed to measure the resulting mPSC frequency at the soma. This data was then fitted with a logarithmic function and the value of the spontaneous release frequency matching the *in vitro* reference value for the mPSC frequency was interpolated. As *in vitro* paired recording data is sparse, all available sources to determine synaptic parameters were re-used for validation.

4.1.4 Datasets used for validation of *in vivo*-like dynamics

Activity in the model is compared with spike-sorted extracellular recordings from the barrel cortex of anaesthetised rats (Reyes-Puerta et al., 2015). The dataset contains single unit spike times for both spontaneous activity and responses to single whisker deflections, across 6 layer-wise neuron populations (L2/3 E, L2/3 I, L4 E, L4 I, L5 E & L5 I). We extend the dataset using the average of L2/3 I, L4 I and L5 I as a reference for L1 I and L6 I, and an alternative reference for L6 E (De Kock et al., 2007). The spontaneous firing rates of the 9 neuron populations are collected in the vector of reference firing rates, $\boldsymbol{V_{FR}}$.

As a secondary comparison, we use a dataset of *in vivo* juxtacellular and whole-cell recordings of barrel cortex responses in awake mice during an active whisker touch paradigm (Yu et al., 2019). While the animal model is different, using this data enables comparison to awake responses of layer-wise E populations and I subpopulations (VIP+ (vasoactive intestinal peptide, a part of our 5HT3aR+ subpopulation), Sst+, FS (fast spiking, corresponding to our PV+ subpopulation)). Moreover, this allows validating the model against properties of cortical responses across similar but different paradigms, reducing the risk of over fitting.

4.1.5 Somatic conductance injection

Random background synaptic inputs, representing uncorrelated inputs from other brain regions not present in the model, are modelled as a conductance-based somatic injection (Figure 4B1). Specifically, we inject conductance signals described by an Ornstein-Uhlenbeck (OU) process (similar to Destexhe et al. (2001)), given by the following equation:

$$\frac{dg(t)}{dt} = -\frac{1}{\tau}[g(t) - g_0] + \sqrt{D} \tag{1}$$

where $g(t)$ is the conductance signal, g_0 its mean value, τ is the decay time constant, D is the diffusion coefficient, and $\chi(t)$ is a Gaussian white noise process. The diffusion coefficient can also be expressed in terms of the standard deviation σ of the signal: $D = \frac{2\sigma^2}{\tau}$.

Note that we only consider an excitatory conductance signal representing long-range excitatory drive, whereas local inhibitory input is deemed sufficient within the circuit model. As we are modeling a non-specific random background noise, we use a different, uncorrelated OU process for each cell.

Given the diversity of morphologies and electrical behaviors of cells in our circuit, we scale the mean and standard deviation of the injected signal based on individual cell properties. Specifically, we compute the input resistance R_{in} of each cell at its resting potential, then take its reciprocal value $G_{in} = 1/R_{in}$ (units of conductance). The mean g_0 and standard deviation σ of the injected conductance signal are then expressed as percentages OU_μ and OU_σ of this input conductance G_{in}:

$$g_0 = \frac{OU_\mu}{100} * G_{in} \tag{2}$$

$$\sigma = \frac{OU_\sigma}{100} * G_{in} \tag{3}$$

The OU_μ and OU_σ percentage values are used in the calibration technique described in the following sections. To reiterate, OU_μ and OU_σ scale the mean of the injected conductance and the size its fluctuations respectively.

4.1.6 Details of spontaneous activity calibration

OU_μ and OU_σ are parameterised separately for each of 9 populations (layer-wise E and I combinations; Figure 4B2), leading to 18 parameters, grouped into two 9-dimensional vectors $\boldsymbol{OU_\mu}$ and $\boldsymbol{OU_\sigma}$. Spontaneous firing rates across populations, denoted by the vector $\boldsymbol{C_{FR}}$, are then determined by the vectors $\boldsymbol{OU_\mu}$ and $\boldsymbol{OU_\sigma}$, and $[Ca^{2+}]_o$. The objective of the calibration procedure is to determine a mapping that outputs the $\boldsymbol{OU_\mu}$ and $\boldsymbol{OU_\sigma}$ required to achieve a particular set of firing rates $\boldsymbol{C_{FR}}$, for a given $[Ca^{2+}]_o$.

This requires two simplifications: First, we reduce the space of possible $\boldsymbol{OU_\mu}$ and $\boldsymbol{OU_\sigma}$ values by fixing $\boldsymbol{OU_\sigma} = \boldsymbol{OU_\mu} * R_{OU}$, where R_{OU} is a pre-specified constant that controls the level of noise assumed to be present in the external synaptic input. Second, we learn the mapping only for dynamical states where the firing rates of the 9 populations are a proportion of reference *in vivo* firing rates, i.e. $\boldsymbol{C_{FR}} = P_{FR} * \boldsymbol{V_{FR}}$, with $P_{FR} \in [0, 1]$ (Figure 4B2). This is based on the assumption that extracellular spike detection sampling biases (Olshausen and Field, 2006; Wohrer et al., 2013) affect all populations equally.

The mapping can be written as $\Psi_{Ca^{2+},R_{OU}} : \boldsymbol{C_{FR}} \mapsto \boldsymbol{OU_\mu}$ and is simplified into two separate mappings which are determined separately and then combined (Figure S1). The first mapping finds values of the 9 output parameters $\boldsymbol{OU_\mu}$, for a given R_{OU}, which produce particular *unconnected firing rates* $\boldsymbol{U_{FR}}$ (i.e., where the neurons in the network are not connected to each other). The second then maps between $\boldsymbol{U_{FR}}$ and $\boldsymbol{C_{FR}}$.

The first mapping $\chi : (R_{OU}, \boldsymbol{U_{FR}}) \mapsto \boldsymbol{OU_\mu}$, is attained by running 1 second simulations over various combinations of OU_μ and OU_σ (Figure S1). R_{OU} constrains OU_μ and OU_σ to a line of possible combinations in the 2D space. We generate an approximation of χ based on linear interpolation between the results of simulations along the line. Note in particular, that χ is independent of $[Ca^{2+}]_o$.

Given the mapping χ, the remaining problem is to determine the values of $\boldsymbol{U_{FR}}$ that achieve certain target firing rates given by $P_{FR} * \boldsymbol{V_{FR}}$, for $P_{FR} \in [0, P_{max}]$ and each combination of $[Ca^{2+}]_o$ and R_{OU}, i.e., to determine the mapping $\phi_{Ca^{2+},R_{OU}} : \boldsymbol{U_{FR}} \mapsto \boldsymbol{C_{FR}}$. This is done by measuring values of $\boldsymbol{C_{FR}}$ produced for given values of $\boldsymbol{U_{FR}}$ in a number of simulations. However, instead of exploring the whole parameter space of possible $\boldsymbol{U_{FR}}$ values, we only explore a small number of values of $\boldsymbol{U_{FR}}$ which we expect to produce the target $\boldsymbol{C_{FR}}$ values. This is done by iteratively learning the mapping $\phi_{Ca^{2+},R_{OU}} : \boldsymbol{U_{FR}} \mapsto \boldsymbol{C_{FR}}$ and in each iteration using ϕ to predict $\boldsymbol{U_{FR}}$ values that bring the dynamics closer to the target firing rate, i.e., by sampling values given by $\boldsymbol{U_{FR}} = \phi^{-1}(C_{FR}) = \phi^{-1}(P_{FR} * \boldsymbol{V_{FR}})$ for 10 equidistant values of $P_{FR} \in [0, P_{max}]$. The initial guess of ϕ is simply the identity, i.e., assuming no effect of connecting the network, with $P_{max} = 0.5$. All other iterations use $P_{max} = 1.0$.

We update ϕ by fitting an exponential: $\boldsymbol{C_{FR}} = \alpha * e^{\beta \boldsymbol{U_{FR}}} + \kappa$ to the values of $\boldsymbol{U_{FR}}$, $\boldsymbol{C_{FR}}$ measured on the latest iteration (Figure S1). In a recurrently connected network such as our model, the connected firing rate of a population depends on the firing rates of all other populations in complex and nonlinear ways. This is addressed by our simplification to restrict the compatible dynamic states, where by definition the target firing rate of one population determines the target firing rates of all others.

The firing rates of the L2/3 I, and L4 I and L6 I populations could not be sufficiently lowered for $P_{FR} < 0.2$ and $P_{FR} < 0.1$ respectively, as they spontaneously fired even at their resting potentials (Figure S1D).

4.1.7 Generalization to other network states

We first approximated ϕ for $[Ca^{2+}]_o = 1.1\,\text{mM}$ and $R_{OU} = 0.4$. To reduce the number of iterations steps needed for other combinations of $[Ca^{2+}]_o$ and R_{OU}, we initialized the optimization process with the mapping ϕ obtained for this parameter pair instead of basing it on the identity (Figure S1D, lower; Figure S1). Only for P_{FR} above 0.8 and $[Ca^{2+}]_o = 1.1\,\text{mM}$ did we have to slightly relax our acceptance criteria (Figure 4D, lower). Additionally $[Ca^{2+}]_o = 1.1\,\text{mM}$, $P_{FR} = 1.0$, and $R_{OU} = 0.2$ led to bursting activity uncharacteristic of *in vivo* activity and was excluded from further study.

4.1.8 Evoked activity comparison and validation

The spike times of single whisker deflection stimuli were drawn from a PSTH of VPM neurons in response to 3 ms mechanical single whisker deflections made at 1 Hz in urethane anesthetized rats (Diamond et al., 1992; Figure 5A2). Since the *in vivo* data for cortical responses to single whisker deflections was from responses to 2 ms mechanical whisker deflections, we compressed the tail of the VPM PSTH to allow a direct comparison with *in silico* responses (Figure 5A2). A VPM PSTH for the active whisker touch stimulus was used from the same dataset as the corresponding cortical responses (Yu et al., 2019).

Firstly, *in silico* responses were compared to data from the C2 barrel of the anaesthetized rat in response to single whisker deflections made at $<$ 1Hz. For the active whisker touch stimulus, *in vivo* activity was used from aggregated over principal barrels corresponding to the untrimmed whisker.

As an initial test of similarity with the corresponding *in vivo* dataset, trial-averaged PSTHs were first calculated for each parameter combination, both for all neurons, and for each of the layer-wise E and I populations. We then tested whether the latencies, 50% and 25%-decay points of the trial-averaged PSTHs were respectively no more than 10 ms, 10 ms and 40 ms later than those of the corresponding *in vivo* populations, and that there was no secondary rise in the PSTHs after the initial decay (by testing that none of the PSTHs for individual populations were more than 35% above baseline after 75 ms). L1 I was excluded from these tests, as it showed little or no response to the stimulus and we had no *in vivo* reference. These tests allowed us to split the 4D parameter space into two regions, one where *in silico* responses are consistent with *in vivo* responses, and another where they are not (see Results).

4.1.9 In-silico experimental methods

Simulation of a morphologically detailed model first requires specifying the conditions (parameters and inputs) under which to perform the simulation. Given the correspondence between variables in the model and properties of biological systems, we are able to mimic to a certain extent the conditions and protocols of experimental studies. These are combinations of existing techniques, or even techniques that cannot or have not yet been performed experimentally. On top of the compensation for missing external input and different $[Ca^{2+}]_o$, we implemented further mechanisms to simulate specific experimental conditions. On a technical level, these comprise somatic current or conductance injections, adjustment of synaptic connectivity parameters, and selective activation of thalamic fibers. These are static conditions, however, in that their time course must be determined before the simulation is run. Somatic injections and connectivity adjustments can be targeted with single neuron or single pair resolution, respectively. To each thalamic fiber or neuron in the model, we can assign an arbitrary spike train, triggering synaptic release from all of its synapses with anatomically determined delays (from axonal conduction speed and path length). These mechanisms can target specific groups of neurons, e.g. based on neuron properties, such as location, layer, m-type or e-type, or inhibitory subpopulation (determined based on me-type as in Markram et al. (2015); Figure 2B). We combined mechanisms to simulate various *in vitro* or *in vivo* experimental paradigms. Pathway lesions, for example, are simulated by selecting sets of pre- and postsynaptic neurons and removing all synaptic connections between them (Figure S2A). Simulated optogenetic stimulation, in addition to being targeted at specific groups of neurons, took into account the attenuation of light with depth for the wavelength being used. Neurons were then inhibited or excited according to the intensity of light reaching them (Figure S2B). Finally, sensory stimuli were simulated by generating instances of stimulus-specific stochastic spike trains activating the thalamic input fibers (Figure S2C).

4.1.10 Optogenetic inhibition or activation

We model optogenetic inhibition or activation of a neuron population through a current injection at the soma of each cell in the population, with an intensity proportional to the cell's threshold current (see Reva et al. (2022)). To mimic the conditions of surface illumination, we considered the dependence of effective depolarization strength on cortical depth using a modified Beer-Lambert law approximation for the exponential attenuation

of light intensity through scattering tissue (Al-Juboori et al., 2013; Azimipour et al., 2014, Figure S2B):

$$I(d) = I_0 \exp(-\mu_{eff}\, d) \tag{4}$$

where $I(d)$ describes the light intensity at depth d (in mm), with a maximum light intensity I_0 (on the surface of the cortex) and an effective attenuation coefficient given by:

$$\mu_{eff} = \sqrt{3\mu_a(\mu_a + \mu_s')} \tag{5}$$

Values for the absorption coefficient μ_a and the reduced scattering coefficient μ_s' were interpolated for the chosen wavelength from Mesradi et al. (2013). For implementation reasons, the targeted cells were grouped into depth bins and for each group the intensity at the center of the bin was used. Bins were equally distributed in terms of the injected current, and not in terms of depth. The value of I_0 was calibrated independently for each experimental paradigm.

4.1.11 Modeling sensory inputs

Sensory inputs were simulated using a three step procedure (Figure S2C2): First, a time series representing sensory stimulation is assigned to each selected thalamic fiber; second, the time series is optionally transformed with a fiber-dependent transfer function; third, a spike train is generated from the time series through a stochastic spiking process. Thalamic input fibers were associated with roughly columnar, overlapping volumes of the model that they formed synaptic connections in (Reimann et al., 2022a). Their centers were projected into the plane using a flat map of the model (Bolaños-Puchet and Reimann, prep), yielding $[x_\zeta, y_\zeta]$, the *flat locations* of each fiber ζ. A sensory stimulus was defined based on fiber location as $\rho_\zeta(t) = \rho(x_\zeta, y_\zeta, t)$. The stimulus function could be partially stochastic and its value was evaluated for each time bin of the simulation (Figure S2C1). Next, a fiber could be associated with a transfer function υ_ζ that transforms the results of ρ. If none is mentioned, identity was used as transfer function. Finally, a spiking process ψ was used to instantiate a spike train for each fiber, based on its transformed time series. That is, the spike train associated with ζ was $\Gamma_\zeta = \psi(\upsilon_\zeta(\rho_\zeta))$. The processes used were stochastic, leading to different spike trains for fibers associated with the same time series. Different, specific ρ, υ and ψ were used for different experimental paradigms that will be further described below.

4.1.12 Recreating Varani et al., 2022

To study how input from L4 contributes to L2/3 subthreshold responses Varani et al. (2022) used a 500 ms long whisker hold paradigm, while patch-clamping PCs in L2/3 in anesthetized and awake mice. We encoded the whisker hold stimulus as a step function ($\rho_\zeta(t) = 1$, if 2000 ms $\leq$ t $<$ 2500 ms, 0 otherwise) in 10% of the VPM fibers within the seven column subvolume. One of four transfer functions were assigned to each fiber, based on the types of kinetic response properties of thalamic neurons identified in (Pe-

tersen et al., 2008). The types were selective for whisker position (υ_{pos}), velocity (υ_{vel}), acceleration (υ_{acc}), or direction (υ_{dir}), and were implemented as:

$$\begin{aligned}
\upsilon_{pos}(t) &= r_{max} \cdot \rho(t) \\
\upsilon_{vel}(t) &= r_{max} \cdot (\rho(t+1) - \rho(t)) \\
\upsilon_{acc}(t) &= r_{max} \cdot (\rho(t+1) - 2\rho(t) + \rho(t-1)) \\
\upsilon_{dir}(t) &= r_{max} \cdot |\rho(t+1) - \rho(t)|_{+}
\end{aligned}$$

where $r_{max} = 150$ Hz denotes the firing rate of a thalamic fiber when its associated feature property is at the fiber's preferred value. Transfer functions were randomly assigned to fibers with the fractions identified in Petersen et al. (2008) (Figure 6A, 11% coding for position and acceleration, 58% for velocity and 20% for direction). The spiking process ψ was an adapting Markov process (Muller et al., 2007) with an adaptation time constant of 100 ms. As the whisker movements were short lasting, rates were evaluated at submillisecond (0.1) resolution.

Similarly to before, only the seven column subvolume (210k neurons) was used for the simulations, and the *in vivo*-like state was realized as $Ca^{2+} = 1.05\,\text{mM}$, $R_{OU} = 0.4$, and $P_{FR} = 0.3$.

The optogenetic inhibition in this experiment targeted 95% (in line with Varani et al. (2022)) of excitatory cells in layer 4. The authors found a few cells which also tested positive for Halo at the bottom of L3 as well, but as they did not quantify it, we decided not to target any lower L3 PCs in the *in silico* version of the experiment. Based on the 595 nm wavelength (yellow light) parameters were set to $\mu_a \approx 0.49\,mm^{-1}$ and $\mu_s' \approx 4.12\,mm^{-1}$. For the depth-based spatial binning of cells, 5 bins were used in L4. After scanning several values, I_0 was set to -200% as that reproduced the ≈ 10 mV hyperpolarization of L4 PCs observed *in vivo*. In line with the *in vivo* experiment, the optogenetic stimulus ended in a (100 ms long) ramp to avoid rebound spikes (Figure 6B).

When going beyond reproducing the same experimental conditions and instead leveraging the *in silico* nature of our setup, synaptic pathways were lesioned by selecting the excitatory population in a given layer as the pre-synaptic population and the excitatory population in L2/3 as the post-synaptic population and not instantiating the connecting synapses during the simulation.

L2/3 PCs had to meet three criteria to be included in the subsequent analysis. Firstly, their activity was required to remain subthreshold during the 500 ms long whisker hold stimulus and in 200 ms long time windows before and after the stimulus, both in control and *in silico* optogenetic runs. Second, they had to be innervated by at least one (active) VPM fiber. Third, the derivative of their voltage trace had to cross the 1 mV/ms threshold in a 20 ms time window after stimulus onset in the control simulation. The last two were motivated by comparing subthreshold voltages to voltage traces from Varani et al. (2022) that showed large, stimulus evoked EPSPs. Around 8% of L2/3 PCs in the central column met all the above criteria and their voltages were averaged to arrive to the traces shown in Figure 6E-F. Thus, unlike in the original analysis, cells rather than trials were averaged. The motivation for this approach is that while *in vivo* it is easier to repeat the same paradigm after establishing stable recording conditions in a given cell, *in silico* it is quicker to record from all cells in a single simulation, instead of repeating the stimulus several times.

4.1.13 Recreating Shapiro et al., 2022

Since our model comprises the nbS1 and not the V1 brain area, we modelled visual drifting gratings in a more abstract way, without taking specifics of the visual system into account. In particular, we defined $\rho(x_\zeta, y_\zeta, t)$ as a spatio-temporal rate pattern corresponding to linear sinusoidal drifting gratings for a fraction F_P of 937 VPM fibers projecting to a single simulated column (30k neurons, 520 μm diameter). For all other VPM fibers ρ was zero. The gratings had a temporal frequency of $f_{temp} = 2\,\text{Hz}$ and a spatial frequency of 0.03 cycles/degree which we translated to $f_{spat} = 0.001\,\text{cycles}/\mu m$ by assuming a cortical magnification factor in rat of 30 μm/degree (Gias et al., 2005). In Figure 7A, the spatial grating patterns are illustrated at different points in time.

As in Shapiro et al. (2022), we used five contrast levels $C \in [0.06, 0.12, 0.24, 0.5, 1.0]$ which were defined as the Michelson contrast given the minimum and maximum luminance values L_{min} and L_{max}:

$$C(L_{min}, L_{max}) = \frac{L_{min} - L_{max}}{L_{min} + L_{max}} \tag{6}$$

Since the physical quantity of luminance does not have a clear correspondence in our model, we used normalized luminance values L_{min} and L_{max} between 0.0 and 1.0 by computing the inverse Michelson contrast centered around a mean normalized luminance of 0.5. The resulting values of L_{min} and L_{max} where then scaled and shifted to the minimum and maximum rates of the sinusoidal modulation R_{min} and R_{max} respectively such that the peak firing rate at contrast 1.0 was given by R_{peak} and the mean of the modulation corresponding to the background firing rate at contrast 0.0 was given by R_{bk}. The resulting sinusoidal input rate signal can be written as:

$$\rho_\zeta(t) = R(t, l_\zeta) = R_{min} + 0.5(R_{max} - R_{min})\Big[1 + \sin(2\pi\, f_{temp}\, t - 2\pi\, f_{spat}\, l_\zeta)\Big]\Big|_+ \tag{7}$$

where t is the time in seconds, l_ζ the linear position of ζ within the grating, and $|_+$ denotes that firing rates are truncated to positive values only. Figure 7B illustrates a random series of rate signals corresponding to different contrasts. No transfer function was used, and spiking process ψ was an adapting Markov process (Muller et al., 2007) with an adaptation time constant of 100 ms. Values for F_P, R_{peak}, and R_{bk} were determined beforehand by a parameter optimization so that the resulting grating responses were qualitatively comparable with the ones reported by Shapiro et al. (2022), see next subsection for details.

Calibration of drifting grating stimulus We ran a parameter scan to determine optimal values for F_P (fraction of 937 VPM fibers projecting to the central column of our model to apply grating stimulus to), R_{peak} (peak firing rate at contrast 1.0), and R_{bk} (background firing rate at contrast 0.0). This calibration was done by running 45 simulations using all combinations of parameter values in the ranges $F_P \in [0.5, 0.75, 1.0]$, $R_{peak} \in [5.0, 10.0, 15.0, 20.0, 25.0]\,\text{Hz}$ and $R_{bk} \in [0.05, 0.1, 0.2]\,\text{Hz}$, and selecting the optimal combination amongst them. Each simulation lasted 40 s during which 20 contrast stimuli were presented for 1 s, followed by a 1 s (blank) inter-stimulus interval. Four contrast levels $C \in [0.06, 0.12, 0.5, 1.0]$ were presented five times each in random order, which was sufficient to fit sigmoidal tuning functions with four parameters (see Eq. 9).

We observed that especially under strong stimulus conditions the response rates of PCs to the first and second cycle of the sinusoidal grating pattern (1 s stimulus at $f_{temp} = 2\,\text{Hz}$)

were quite different, with the second response largely attenuated due to synaptic depletion. Therefore, we extracted first and second peak firing rates r_1 and r_2 respectively from the peristimulus time histograms (PSTHs) computed with 1 ms resolution and 20 ms Gaussian smoothing (Figure S6). We defined a measure of the normalized peak difference as the Michelson contrast of the peak rates r_1 and r_2, given by

$$\hat{r}_{diff} = \frac{r_1 - r_2}{r_1 + r_2} \tag{8}$$

Additionally, we extracted average firing rates for each contrast level of the whole population of PCs within the full (1 s) as well as the first and second halves (0.5 s each) of the stimulation intervals. We then fitted sigmoidal tuning functions with parameters c_{50}, m, n, and R_{max} (see Eq. 9) to these average tuning responses (Figure S7). Finally, as summarized in Figure S6 and S7, we selected the best combination of parameters based on the following selection criteria:

- The peak firing rates in response to the grating stimulus should be sufficiently strong, covering a range of values including the one reported in (Shapiro et al., 2022, cf. Figure 1D). So we imposed the constraint that the maximum peak rates over the whole population of PCs of the first and second peaks r_1 and r_2 respectively should be at least $r_{th} = 30\,\text{Hz}$ at maximum contrast.
- The peak responses to the first and second cycle of the grating stimulus should not be too different. So we aimed for a low peak difference $\hat{r}_{diff}$ at maximum contrast.
- The overall tuning response of the PCs should be in a regime where the tuning curve would have a sigmoidal shape, meaning that it should be increasing but saturating with increasing contrasts. To fulfill this constraint, we aimed for
  - Low c_{50}, i.e., the inflection point of the tuning curve would be at low contrasts
  - High n, i.e., a steep non-linear increase of the tuning curve until saturation

In order to combine these criteria independent of the actual scales of $\hat{r}_{diff}$, c_{50} and n, we computed their individual rank scores in decreasing ($\hat{r}_{diff}$, c_{50}: lower is better) or increasing (n: higher is better) order. We then selected the parameter combination with the highest product of rank scores, excluding the ones with peak firing rates r_1 and r_2 below r_{th} and the ones with c_{50} values close to 1.0 (border cases). We found an optimal parameter combination of $F_P = 1.0$, $R_{peak} = 10.0\,\text{Hz}$, and $R_{bk} = 0.20\,\text{Hz}$ which we used throughout this *in-silico* experiment.

Optogenetic stimulation Optogenetic stimulation was targeted at either 1654 PV+ or 822 Sst+ interneurons in a single column. We used parameters $\mu_a \approx 0.46\,\text{mm}^{-1}$ and $\mu_s' \approx 5.38\,\text{mm}^{-1}$, based on the wavelength of 470 nm (blue light; see Figure S2). I_0 was increased from 0% to 300% in steps of 50%.

Quantification of contrast tuning responses by sigmoidal functions We quantified contrast tuning responses in the same way as described by Shapiro et al. (2022), by least-squares fitting sigmoidal functions to the normalized tuning curves. Normalized tuning curves were obtained by computing the time-averaged firing rates of all 1 s stimulus intervals and dividing them by the mean baseline firing rate (i.e., w/o optogenetic stimulation) at the highest contrast level. The sigmoidal function was given by

$$R(c) = \frac{R_{max}\, c^n}{c^n + c_{50}^n} + m \tag{9}$$

where $R(c)$ describes the response amplitude at contrast c, m is the baseline response at minimum contrast, R_{max} is the maximum increase above baseline, n defines the steepness of the curve, and c_{50} is the contrast at half R_{max}. We used the coefficient of determination (r^2 score) as a measure of the goodness of fit.

Detection of neurons with robust contrast tuning We identified PV+, Sst+, and pyramidal neurons with robust contrast tuning behavior under all conditions. In the experimental study of Shapiro et al. (2022), tetrode recordings were used together with spike sorting. Correspondingly, we only considered neurons firing at rates above 0.5 Hz under all stimulus conditions, meaning they could potentially be detected by spike sorting (Pedreira et al., 2012). In addition, we considered neurons as being robustly tuned if they had strictly monotonically increasing tuning curves.

Modelling the effects of optogenetic stimulation of interneurons Direct photostimulation effects on interneurons were modelled by a divisive scaling model $R_{div}(c)$, a subtractive shifting model $R_{sub}(c)$, or a saturation additive model $R_{sat}(c)$ (Shapiro et al., 2022). For fitting these models, the parameters c_{50}, m, n, and R_{max} of the underlying contrast tuning function $R(c)$ were kept constant at values obtained from baseline fits (i.e., w/o optogenetic stimulation). The divisive scaling model was defined as

$$R_{div}(c) = R(c)/g \tag{10}$$

with a scaling term g. The subtractive shifting model was given by

$$R_{sub}(c) = R(c) - h \Big|_{+} \tag{11}$$

with a shifting term h and rectification to rates equal or above zero. The saturation additive model was defined as

$$R_{sat}(c) = R(c) + \frac{S\, c^{-n}}{c^{-n} + c_{50}^{-n}} + A \tag{12}$$

with a saturation term S and an additive term A. We used the r^2 score to measure the goodness of model fits.

Indirect effects on PCs receiving inhibitory input from optogenetically activated interneurons were modelled by a conductance-based model $R_{cond}(c)$, assuming a saturating additive model description of interneurons (Shapiro et al., 2022). Response rates under this conductance-based model were given by

$$R_{cond}(c) = \Big[\Delta V(c) - V_{th}\Big]^3 \Big|_{+} \tag{13}$$

with a spike threshold $V_{th} = 3.4\,\mathrm{mV}$ and rectification to rates equal or above zero. The membrane potential $\Delta V(c)$ as a function of contrast was given by

$$\Delta V(c) = \frac{g_L\, R_L + g_E(c)\, R_E + g_I(c)\, R_I}{g_L + g_E(c) + g_I(c)} - V_r \tag{14}$$

with values for leak conductance $g_L = 6\,\mathrm{nS}$, leak reversal potential $R_L = -50\,\mathrm{mV}$, excitatory reversal potential $R_E = 0\,\mathrm{mV}$, inhibitory reversal potential $R_I = -65\,\mathrm{mV}$, and

resting potential $V_r = -50\,\mathrm{mV}$ as reported by Shapiro et al. (2022). The excitatory synaptic conductance was given by

$$g_E(c) = \frac{g_{E_max}\, c^n}{c^n + c_{50}^n} + g_{E_min} \tag{15}$$

with the excitatory conductances at low/high contrast given by g_{E_min} and g_{E_max} respectively. The inhibitory synaptic conductance was given by

$$g_I(c) = g_E(c) + \frac{S\, c^{-n}}{c^{-n} + c_{50}^{-n}} + \Delta g_{IE_min} + A \tag{16}$$

with an inhibitory conductance offset $\Delta g_{IE_min} = 2\,\mathrm{nS}$ at low contrast relative to g_{E_min}.

In a first step, parameters S and A were set to zero and the model parameters $c50$, g_{E_min}, g_{E_max}, and n were fit to baseline responses of PCs. In a second step, those parameter values were kept constant and the model parameters S and A were fit to PC responses under photostimulation conditions. Again, we used the r^2 score to measure the goodness of model fits.

4.1.14 Recreating Prince et al., 2021

We also compared the *in vivo* state of our model with the results of a recent *in vitro* study (Prince et al., 2021), which explored how neurons with different biophysical properties encode different types of signals. The *in vitro* study optically activated groups of 10 PCs in slices of L2/3 barrel cortex from mouse lines labelling fast-spiking (FS) and regular-spiking (RS) interneurons. Each PC was targeted individually and a binary signal was encoded either through changes in the rate of optical pulses applied to the 10 stimulus neurons, or through changes in the synchronicity of the pulses. The mutual information shared between the binary signal (when encoded either as changes in firing rate or synchronicity) and the firing rate of different inhibitory sub-types (recorded using whole-cell patch clamping *in vitro*) was analysed.

While the *in vitro* stimuli used optical pulses targeted at single neurons with timings drawn from Poisson processes, it was not necessary to explicitly model such an optical stimulus *in silico*, as we can instead elicit spikes directly in the model. In the original study, the 10 stimulus neurons were uniformly separated in a grid-like pattern at horizontal and vertical distances of $\sim 50\,\mu m$. The binary signal alternated between two states at random intervals of 2-7 s. For the rate coding paradigm, the timings of the optical pulses for the 10 stimulus neurons were drawn from 10 independent inhomogeneous Poisson processes, with the rates of optical activation varying between 5 Hz and 0.5 Hz for the up and down states respectively (average firing rate: 2.7 Hz). For the synchronous case, the timings of the optical pulses for the 10 stimulus neurons were drawn from a single inhomogeneous Poisson process during the up state, or 10 independent inhomogeneous Poisson processes during the down state. For the synchronous case, the firing rates of the up and down state were both 2.7 Hz. We therefore tested stimulus encoding using a range of stimulus neuron counts: from 10 to 1,000.

In our interpretation of the study, mutual information was measured between the binary signal and neural activity during a 0-5 ms and 5-50 ms window following a change in the signal. These represented 'early' and 'late' stimulus encoding windows following

the change in the signal, respectively. As the synchronous up state activated synchronous patterns at a rate of 2.7 Hz, we calculated that a synchronous pattern would only be activated during the early and late windows with probability 0.0135 ($= 2.7 * 5/1000$) and 0.1125 ($= 2.7 * 45/1000$) respectively. We therefore chose to use higher FR of 20 Hz for the synchronous up and down states, and to analyse mutual information between the binary signal and all 50 ms bins. To afford comparison with the rate code experiment type, we used 30 Hz and 10 Hz as the FRs of the up and down states respectively. We also compare stimulus coding during the first 50 ms following the stimulus change for both the synchronous and rate stimulus types.

4.1.15 Analyzing long-range connectivity & correlations

Neurons were split into hexagonal subvolumes of a specified diameter d considering their locations in a flattened view (Bolaños-Puchet and Reimann, prep).Then, the number of long-range connections within and between the hexagonal subvolumes were counted, yielding in S, the adjacency matrix of the resulting directed graph. Distances between hexagonal subvolumes were calculated by considering the centers of the hexagons in the flattened view. Furthermore, correlations of spiking activity of pairs of hexagonal subvolumes were also calculated. To that end, all spikes within a hexagonal subvolume were pooled and their number in 5 ms time bins; and lastly the Pearson correlations of the resulting time series were calculated. The correlation within a hexagonal subvolume was calculated similarly, but using the separate time series of the E and I populations. Together, this yielded F, the matrix of correlations of subvolumes. Based on S and F, the expected correlations of long-range inputs was calculated as follows: Let i be a hexagonal subvolume and S_i the column of S associated with input counts into i. Then $P = S_i \cdot S_i^\top$ is in the matrix of counts of pairs of inputs for all pairs of hexagonal subvolumes. Combining P and F allows one to estimate the distribution of correlations of long-range inputs into i, albeit at the population rather than single-cell level. For the correlation in Figure 8A2, H, J1 a hexagon size of $400\mu m$ was used, while in Figure 8I2 a smaller size of only $50\mu m$ was used.

4.1.16 Node participation

Given a connectivity graph G, a directed n-simplex in G is a set of $n+1$ nodes which are all all-to-all connected in G in a feed-forward fashion, i.e., such that any subset of these has a unique source and a unique sink (see Reimann et al. (2017) for more details). The *n-node participation* of a node v in G is the number of directed n-simplices this node is part of. In particular, for $n = 1$, this is the total degree of the node in G. Thus, this can be though of a generalization of the notion of degree that takes into account account higher order interactions and has been shown to strongly correlate with other node centrality metrics Sizemore et al. (2018).

4.2 Quantification and statistical analysis

Details of all statistical analyses can be found in figures and figure legends.

4.3 Additional Resources

No other additional resources.

Videos

1. Layer-wise E and I population rasters and max-normalised histograms of spontaneous activity for the central column of the seven column subvolume for each of the 60 meta-parameter combinations. Meta-parameter values are shown in brackets in the following order: Ca^{2+}, P_{FR}, R_{OU}.

2. Visualisation of spontaneous activity for the seven column subvolume for the parameter combination $Ca^{2+} = 1.1\,\mathrm{mM}$, $P_{FR} = 0.9$, $R_{OU} = 0.2$ after collapsing activity to flatspace (activity binned and smoothed).

3. Layer-wise E and I population rasters and max-normalised histograms of evoked activity during the 10 single whisker deflection protocol for each of the simulated meta-parameter combinations. Meta-parameter values are shown in brackets in the following order: Ca^{2+}, P_{FR}, R_{OU}, F_P.

4. Trial-averaged max-normalised histograms of evoked activity during the 10 single whisker deflection protocol for each of the simulated meta-parameter combinations. Rasters of spiking activity shown for the first of 10 trials activity. Dashed lines show *in vivo* single whisker deflection reference data. Meta-parameter values are shown in brackets in the following order: Ca^{2+}, P_{FR}, R_{OU}, F_P.

5. Visualisation of trial-averaged response of the seven column subvolume over the 10 single whisker deflection protocol for the parameter combination $Ca^{2+} = 1.1\,\mathrm{mM}$, $P_{FR} = 0.3$, $R_{OU} = 0.4$, $F_P = 20\%$ after collapsing activity to flatspace (activity binned and smoothed).

6. Visualisation of spontaneous activity for the full nbS1 model for the parameter combination $Ca^{2+} = 1.05\,\mathrm{mM}$, $P_{FR} = 0.15$, $R_{OU} = 0.4$ after collapsing activity to flatspace (activity binned and smoothed).

7. Visualisation of trial-averaged response of the full nbS1 model over the 10 single whisker deflection protocol for the parameter combination $Ca^{2+} = 1.1\,\mathrm{mM}$, $P_{FR} = 0.15$, $R_{OU} = 0.4$, $F_P = 20\%$ after collapsing activity to flatspace (activity binned and smoothed).

References

Abdellah, M., Hernando, J., Eilemann, S., Lapere, S., Antille, N., Markram, H., and Schürmann, F. (2018). NeuroMorphoVis: A collaborative framework for analysis and visualization of neuronal morphology skeletons reconstructed from microscopy stacks. *Bioinformatics*, 34(13):i574–i582.

Al-Juboori, S. I., Dondzillo, A., Stubblefield, E. A., Felsen, G., Lei, T. C., and Klug, A. (2013). Light scattering properties vary across different regions of the adult mouse brain. *PloS one*, 8(7):e67626.

Amzica, F., Massimini, M., and Manfridi, A. (2002). Spatial buffering during slow and paroxysmal sleep oscillations in cortical networks of glial cells in vivo. *Journal of Neuroscience*, 22(3):1042–1053.

Ascoli, G. A. et al. (2008). Petilla terminology: Nomenclature of features of GABAergic interneurons of the cerebral cortex. *Nature Reviews Neuroscience*, 9(7):557–568.

Attwell, D. and Laughlin, S. B. (2001). An energy budget for signaling in the grey matter of the brain. *Journal of Cerebral Blood Flow & Metabolism*, 21(10):1133–1145.

Azimipour, M., Baumgartner, R., Liu, Y., Jacques, S. L., Eliceiri, K. W., and Pashaie, R. (2014). Extraction of optical properties and prediction of light distribution in rat brain tissue. *Journal of biomedical optics*, 19(7):075001.

Barros-Zulaica, N., Rahmon, J., Chindemi, G., Perin, R., Markram, H., Muller, E., and Ramaswamy, S. (2019). Estimating the Readily-Releasable Vesicle Pool Size at Synaptic Connections in the Neocortex. *Frontiers in Synaptic Neuroscience*, 11(29).

Barth, A. L. and Poulet, J. F. (2012). Experimental evidence for sparse firing in the neocortex. *Trends in neurosciences*, 35(6):345–355.

Beierlein, M. and Connors, B. W. (2002). Short-term dynamics of thalamocortical and intracortical synapses onto layer 6 neurons in neocortex. *Journal of Neurophysiology*, 88(4):1924–1932.

Beierlein, M., Gibson, J. R., and Connors, B. W. (2003). Two Dynamically Distinct Inhibitory Networks in Layer 4 of the Neocortex. *Journal of Neurophysiology*, 90(5):2987–3000.

Berger, T. (2009). *Properties of Neocortical Microcircuits*. PhD thesis, Ecole Polytechnique Fédérale de Lausanne.

Berger, T., Larkum, M. E., and Lüscher, H. R. (2001). High Ih channel density in the distal apical dendrite of layer V pyramidal cells increases bidirectional attenuation of EPSPs. *Journal of Neurophysiology*, 85(2):855–868.

Billeh, Y. N., Cai, B., Gratiy, S. L., Dai, K., Iyer, R., Gouwens, N. W., Abbasi-Asl, R., Jia, X., Siegle, J. H., Olsen, S. R., Koch, C., Mihalas, S., and Arkhipov, A. (2020). Systematic Integration of Structural and Functional Data into Multi-Scale Models of Mouse Primary Visual Cortex. *Neuron*, 106(3):388–403.

Bolaños-Puchet, S. and Reimann, M. W. (in prep.). Flattening of enhanced cortical atlases opens up new possibilities for data-driven modeling and data visualization. *in prep.*

Borst, J. G. G. (2010). The low synaptic release probability in vivo. *Trends in neurosciences*, 33(6):259–266.

Brasier, D. J. and Feldman, D. E. (2008). Synapse-specific expression of functional presynaptic NMDA receptors in rat somatosensory cortex. *Journal of Neuroscience*, 28(9):2199–2211.

Buzsáki, G. and Mizuseki, K. (2014). The log-dynamic brain: how skewed distributions affect network operations. *Nature Reviews Neuroscience*, 15(4):264–278.

Buzsáki, G. (2004). Large-scale recording of neuronal ensembles. *Nature Neuroscience*, 7(5):446–451. Number: 5 Publisher: Nature Publishing Group.

Chindemi, G., Abdellah, M., Amsalem, O., Benavides-Piccione, R., Delattre, V., Doron, M., Ecker, A., Jaquier, A. T., King, J., Kumbhar, P., Monney, C., Perin, R., Rössert, C., Tuncel, M. A., van Geit, W., DeFelipe, J., Graupner, M., Segev, I., Markram, H., and Muller, E. (2022). A calcium-based plasticity model predicts long-term potentiation and depression in the neocortex. *Nature Communications*, 13(3038).

Colizza, V., Flammini, A., Serrano, M. A., and Vespignani, A. (2006). Detecting rich-club ordering in complex networks. *Nature physics*, 2(2):110–115.

Constantinople, C. M. and Bruno, R. M. (2013). Deep Cortical Layers Are Activated Directly by Thalamus. *Science*, 340(6140):1591–1594.

Cremonesi, F., Hager, G., Wellein, G., and Schürmann, F. (2020). Analytic performance modeling and analysis of detailed neuron simulations. *International Journal of High Performance Computing Applications*, 34((4)):428–449.

Crochet, S. and Petersen, C. C. (2006). Correlating whisker behavior with membrane potential in barrel cortex of awake mice. *Nature Neuroscience*, 9(5):608–610.

Dai, K., Hernando, J., Billeh, Y. N., Gratiy, S. L., Planas, J., Davison, A. P., Dura-Bernal, S., Gleeson, P., Devresse, A., Dichter, B. K., Gevaert, M., King, J. G., van Geit, W. A., Povolotsky, A. V., Muller, E., Courcol, J. D., and Arkhipov, A. (2020). The SONATA data format for efficient description of large-scale network models. *PLoS Computational Biology*, 16(2):e1007696.

Datwani, A., Iwasato, T., Itohara, S., and Erzurumlu, R. S. (2002). NMDA receptor-dependent pattern transfer from afferents to postsynaptic cells and dendritic differentiation in the barrel cortex. *Molecular and Cellular Neuroscience*, 21(3):477–492.

De Kock, C., Bruno, R. M., Spors, H., and Sakmann, B. (2007). Layer-and cell-type-specific suprathreshold stimulus representation in rat primary somatosensory cortex. *The Journal of physiology*, 581(1):139–154.

Destexhe, A., Rudolph, M., Fellous, J. M., and Sejnowski, T. J. (2001). Fluctuating synaptic conductances recreate in vivo-like activity in neocortical neurons. *Neuroscience*, 107(1):13–24.

Diamond, M. E., Armstrong-James, M., and Ebner, F. F. (1992). Somatic sensory responses in the rostral sector of the posterior group (pom) and in the ventral posterior medial nucleus (vpm) of the rat thalamus. *Journal of Comparative Neurology*, 318(4):462–476.

Dura-Bernal, S., Neymotin, S. A., Suter, B. A., Dacre, J., Moreira, J. V., Urdapilleta, E., Schiemann, J., Duguid, I., Shepherd, G. M., and Lytton, W. W. (2023). Multiscale model of primary motor cortex circuits predicts in vivo cell-type-specific, behavioral state-dependent dynamics. *Cell Reports*, 42(6).

Ecker, A., Romani, A., Sáray, S., Káli, S., Migliore, M., Falck, J., Lange, S., Mercer, A., Thomson, A. M., Muller, E., Reimann, M. W., and Ramaswamy, S. (2020). Data-driven integration of hippocampal CA1 synaptic physiology in silico. *Hippocampus*, 30(11):1129–1145.

Egger, R., Narayanan, R. T., Guest, J. M., Bast, A., Udvary, D., Messore, L. F., Das, S., De Kock, C. P., and Oberlaender, M. (2020). Cortical output is gated by horizontally projecting neurons in the deep layers. *Neuron*, 105(1):122–137.

Feldmeyer, D. (2012). Excitatory neuronal connectivity in the barrel cortex. *Frontiers in Neuroanatomy*, 6(24).

Feldmeyer, D., Egger, V., Lübke, J., and Sakmann, B. (1999). Reliable synaptic connections between pairs of excitatory layer 4 neurones within a single 'barrel' of developing rat somatosensory cortex. *Journal of Physiology*, 521(1):169–190.

Feldmeyer, D., Lübke, J., and Sakmann, B. (2006). Efficacy and connectivity of intracolumnar pairs of layer 2/3 pyramidal cells in the barrel cortex of juvenile rats. *Journal of Physiology*, 575(2):583–602.

Feldmeyer, D., Lübke, J., Silver, R. A., and Sakmann, B. (2002). Synaptic connections between layer 4 spiny neurone-layer 2/3 pyramidal cell pairs in juvenile rat barrel cortex: Physiology and anatomy of interlaminar signalling within a cortical column. *Journal of Physiology*, 538(3):803–822.

Feldmeyer, D., Roth, A., and Sakmann, B. (2005). Monosynaptic connections between pairs of spiny stellate cells in layer 4 and pyramidal cells in layer 5A indicate that lemniscal and paralemniscal afferent pathways converge in the infragranular somatosensory cortex. *Journal of Neuroscience*, 25(13):3423–3431.

Felleman, D. J. and Van Essen, D. C. (1991). Distributed hierarchical processing in the primate cerebral cortex. *Cerebral Cortex*, 1:1–47.

Fuhrmann, G., Segev, I., Markram, H., and Tsodyks, M. (2002). Coding of Temporal Information by Activity-Dependent Synapses. *Journal of Neurophysiology*, 87(1):140–148.

Gao, L., Liu, S., Gou, L., Hu, Y., Liu, Y., Deng, L., Ma, D., Wang, H., Yang, Q., Chen, Z., Liu, D., Qiu, S., Wang, X., Wang, D., Wang, X., Ren, B., Liu, Q., Chen, T., Shi, X., Yao, H., Xu, C., Li, C. T., Sun, Y., Li, A., Luo, Q., Gong, H., Xu, N., and Yan, J. (2022). Single-neuron projectome of mouse prefrontal cortex. *Nature Neuroscience*, 25(4):515–529.

Gias, C., Hewson-Stoate, N., Jones, M., Johnston, D., Mayhew, J., and Coffey, P. (2005). Retinotopy within rat primary visual cortex using optical imaging. *Neuroimage*, 24(1):200–206.

Gonzalez, K. C., Losonczy, A., and Negrean, A. (2022). Dendritic Excitability and Synaptic Plasticity In Vitro and In Vivo. *Neuroscience*, 489:165–175.

Gupta, A., Wang, Y., and Markram, H. (2000). Organizing principles for a diversity of GABAergic interneurons and synapses in the neocortex. *Science*, 287(5451):273–278.

Harris, J. A., Mihalas, S., et al. (2019). Hierarchical organization of cortical and thalamic connectivity. *Nature*, 575(7781):195–202.

Henze, D. A., Borhegyi, Z., Csicsvari, J., Mamiya, A., Harris, K. D., and Buzsaki, G. (2000). Intracellular features predicted by extracellular recordings in the hippocampus in vivo. *Journal of neurophysiology*, 84(1):390–400.

Isbister, J. B., Reyes-Puerta, V., Sun, J.-J., Horenko, I., and Luhmann, H. J. (2021). Clustering and control for adaptation uncovers time-warped spike time patterns in cortical networks in vivo. *Scientific Reports*, 11(1):1–20.

Jahr, C. E. and Stevens, C. F. (1990). Voltage dependence of NMDA-activated macroscopic conductances predicted by single-channel kinetics. *The Journal of neuroscience*, 10(9):3178–3182.

Jones, H. and Keep, R. (1988). Brain Fluid Calcium Concentration and Response To Acute Hypercalcaemia During Development in the Rat. *Journal of Physiology*, 402:579–593.

Kawaguchi, Y., Karube, F., and Kubota, Y. (2006). Dendritic branch typing and spine expression patterns in cortical nonpyramidal cells. *Cerebral Cortex*, 16(5):696–711.

Larkman, A. U. (1991). Dendritic morphology of pyramidal neurones of the visual cortex of the rat: Iii. spine distributions. *Journal of comparative neurology*, 306(2):332–343.

Larkum, M. E., Zhu, J. J., and Sakmann, B. (2001). Dendritic mechanisms underlying the coupling of the dendritic with the axonal action potential initiation zone of adult rat layer 5 pyramidal neurons. *Journal of Physiology*, 533(2):447–466.

Larsen, R. S. and Sjöström, P. J. (2015). Synapse-type-specific plasticity in local circuits. *Current Opinion in Neurobiology*, 35:127–135.

Le Bé, J. V., Silberberg, G., Wang, Y., and Markram, H. (2007). Morphological, electrophysiological, and synaptic properties of corticocallosal pyramidal cells in the neonatal rat neocortex. *Cerebral Cortex*, 17(9):2204–2213.

Lennie, P. (2003). The cost of cortical computation. *Current biology*, 13(6):493–497.

Ling, D. S. and Benardo, L. S. (1999). Restrictions on inhibitory circuits contribute to limited recruitment of fast inhibition in rat neocortical pyramidal cells. *Journal of Neurophysiology*, 82(4):1793–1807.

Loebel, A., Silberberg, G., Helbig, D., Markram, H., Tsodyks, M., and Richardson, M. J. E. (2009). Multiquantal release underlies the distribution of synaptic efficacies in the neocortex. *Frontiers in Cellular Neuroscience*, 3(27).

Lübke, J. and Feldmeyer, D. (2007). Excitatory signal flow and connectivity in a cortical column: Focus on barrel cortex. *Brain Structure and Function*, 212:3–17.

Markram, H., Lübke, J., Frotscher, M., Roth, A., and Sakmann, B. (1997a). Physiology and anatomy of synaptic connections between thick tufted pyramidal neurones in the developing rat neocortex. *Journal of Physiology*, 500(2):409–440.

Markram, H., Lübke, J., Frotscher, M., and Sakmann, B. (1997b). Regulation of Synaptic Efficacy by Coincidence of Postsynaptic APs and EPSPs. *Science*, 275(5297):213–215.

Markram, H., Muller, E., Ramaswamy, S., Reimann, M. W., et al. (2015). Reconstruction and Simulation of Neocortical Microcircuitry. *Cell*, 163(2):456–492.

Markram, H., Toledo-Rodriguez, M., Wang, Y., Gupta, A., Silberberg, G., and Wu, C. (2004). Interneurons of the neocortical inhibitory system. *Nature Reviews Neuroscience*, 5(10):793–807.

Markram, H., Wang, Y., and Tsodyks, M. (1998). Differential signaling via the same axon of neocortical pyramidal neurons. *PNAS*, 95(9):5323–8.

Massimini, M. and Amzica, F. (2001). Extracellular calcium fluctuations and intracellular potentials in the cortex during the slow sleep oscillation. *Journal of Neurophysiology*, 85(3):1346–1350.

Mesradi, M., Genoux, A., Cuplov, V., Abi-Haidar, D., Jan, S., Buvat, I., and Pain, F. (2013). Experimental and analytical comparative study of optical coefficient of fresh and frozen rat tissues. *Journal of biomedical optics*, 18(11):117010.

Meyer, H. S., Wimmer, V. C., Hemberger, M., Bruno, R. M., De Kock, C. P., Frick, A., Sakmann, B., and Helmstaedter, M. (2010). Cell type-specific thalamic innervation in a column of rat vibrissal cortex. *Cerebral Cortex*, 20(10):2287–2303.

Muller, E., Buesing, L., Schemmel, J., and Meier, K. (2007). Spike-Frequency Adapting Neural Ensembles: Beyond Mean Adaptation and Renewal Theories. *Neural Computation*, 19:2958–3010.

Nevian, T., Larkum, M. E., Polsky, A., and Schiller, J. (2007). Properties of basal dendrites of layer 5 pyramidal neurons: A direct patch-clamp recording study. *Nature Neuroscience*, 10(2):206–214.

Newton, T. H., Reimann, M. W., Abdellah, M., Chevtchenko, G., Muller, E. B., and Markram, H. (2021). In silico voltage-sensitive dye imaging reveals the emergent dynamics of cortical populations. *Nature Communications*, 12(3630).

Nigam, S., Shimono, M., Ito, S., Yeh, F.-C., Timme, N., Myroshnychenko, M., Lapish, C. C., Tosi, Z., Hottowy, P., Smith, W. C., et al. (2016). Rich-club organization in effective connectivity among cortical neurons. *Journal of Neuroscience*, 36(3):670–684.

Nolte, M., Gal, E., Markram, H., and Reimann, M. W. (2020). Impact of higher order network structure on emergent cortical activity. *Network Neuroscience*, 4(1):292–314.

Nolte, M., Reimann, M. W., King, J. G., Markram, H., and Muller, E. B. (2019). Cortical reliability amid noise and chaos. *Nature Communications*, 10(3792).

Oh, S. W., Harris, J. A., Ng, L., Winslow, B., Cain, N., Mihalas, S., Wang, Q., Lau, C., Kuan, L., Henry, A. M., Mortrud, M. T., Ouellette, B., Nguyen, T. N., Sorensen, S. A., Slaughterbeck, C. R., Wakeman, W., Li, Y., Feng, D., Ho, A., Nicholas, E., Hirokawa, K. E., Bohn, P., Joines, K. M., Peng, H., Hawrylycz, M. J., Phillips, J. W., Hohmann, J. G., Wohnoutka, P., Gerfen, C. R., Koch, C., Bernard, A., Dang, C., Jones, A. R., and Zeng, H. (2014). A mesoscale connectome of the mouse brain. *Nature*, 508(7495):207–214.

Ohana, O. and Sakmann, B. (1998). Transmitter release modulation in nerve terminals of rat neocortical pyramidal cells by intracellular calcium buffers. *The Journal of Physiology*, 513(1):135–148.

Olshausen, B. A. and Field, D. J. (2006). What is the other 85 percent of v1 doing. *L. van Hemmen, & T. Sejnowski (Eds.)*, 23:182–211.

Park, J. M., Hong, Y. K., Rodgers, C. C., Dahan, J. B., Schmidt, E. R., and Bruno, R. M. (2020). Deep and superficial layers of the primary somatosensory cortex are critical for whisker-based texture discrimination in mice. *bioRxiv*.

Pedreira, C., Martinez, J., Ison, M. J., and Quiroga, R. Q. (2012). How many neurons can we see with current spike sorting algorithms? *Journal of neuroscience methods*, 211(1):58–65.

Petersen, R. S., Brambilla, M., Bale, M. R., Alenda, A., Panzeri, S., Montemurro, M. A., and Maravall, M. (2008). Diverse and Temporally Precise Kinetic Feature Selectivity in the VPm Thalamic Nucleus. *Neuron*, 60(5):890–903.

Prince, L. Y., Tran, M. M., Grey, D., Saad, L., Chasiotis, H., Kwag, J., Kohl, M. M., and Richards, B. A. (2021). Neocortical inhibitory interneuron subtypes are differentially attuned to synchrony-and rate-coded information. *Communications Biology*, 4(1):1–16.

Qi, G. and Feldmeyer, D. (2016). Dendritic Target Region-Specific Formation of Synapses between Excitatory Layer 4 Neurons and Layer 6 Pyramidal Cells. *Cerebral Cortex*, 26(4):1569–1579.

Reimann, M. W., Anastassiou, C. A., Perin, R., Hill, S. L., Markram, H., and Koch, C. (2013). A biophysically detailed model of neocortical local field potentials predicts the critical role of active membrane currents. *Neuron*, 79(2):375–390.

Reimann, M. W., Nolte, M., Scolamiero, M., Turner, K., Perin, R., Chindemi, G., Dłotko, P., Levi, R., Hess, K., and Markram, H. (2017). Cliques of neurons bound into cavities provide a missing link between structure and function. *Frontiers in Computational Neuroscience*, 11(48).

Reimann, M. W., Puchet, S. B., Santander, D. E., Courcol, J.-D., et al. (2022a). Modeling and simulation of rat non-barrel somatosensory cortex. part i: Modeling anatomy. *bioRxiv*.

Reimann, M. W., Riihimäki, H., Smith, J. P., Lazovskis, J., Pokorny, C., and Levi, R. (2022b). Topology of synaptic connectivity constrains neuronal stimulus representation, predicting two complementary coding strategies. *PLoS ONE*, 17(1):e0261702.

Renart, A., De La Rocha, J., Bartho, P., Hollender, L., Parga, N., Reyes, A., and Harris, K. D. (2010). The asynchronous state in cortical circuits. *science*, 327(5965):587–590.

Reva, M., Rössert, C., Arnaudon, A., Damart, T., Mandge, D., Tuncel, A., Ramaswamy, S., Markram, H., and Van Geit, W. (2022). A universal workflow for creation, validation and generalization of detailed neuronal models. *bioRxiv*.

Reyes, A. and Sakmann, B. (1999). Developmental switch in the short-term modification of unitary EPSPs evoked in layer 2/3 and layer 5 pyramidal neurons of rat neocortex. *Journal of Neuroscience*, 19(10):3827–3835.

Reyes-Puerta, V., Sun, J.-J., Kim, S., Kilb, W., and Luhmann, H. J. (2015). Laminar and columnar structure of sensory-evoked multineuronal spike sequences in adult rat barrel cortex in vivo. *Cerebral Cortex*, 25(8):2001–2021.

Rozov, A., Burnashev, N., Sakmann, B., and Neher, E. (2001). Transmitter release modulation by intracellular ca2+ buffers in facilitating and depressing nerve terminals of pyramidal cells in layer 2/3 of the rat neocortex indicates a target cell-specific difference in presynaptic calcium dynamics. *The Journal of physiology*, 531(3):807–826.

Sermet, B. S., Truschow, P., Feyerabend, M., Mayrhofer, J. M., Oram, T. B., Yizhar, O., Staiger, J. F., and Petersen, C. C. (2019). Pathway-, layer-and cell-type-specific thalamic input to mouse barrel cortex. *eLife*, 8:e52665.

Shapiro, J. T., Michaud, N. M., King, J. L., and Crowder, N. A. (2022). Optogenetic activation of interneuron subtypes modulates visual contrast responses of mouse v1 neurons. *Cerebral Cortex*, 32(5):1110–1124.

Shoham, S., O'Connor, D. H., and Segev, R. (2006). How silent is the brain: is there a "dark matter" problem in neuroscience? *Journal of Comparative Physiology A*, 192(8):777–784.

Silberberg, G. and Markram, H. (2007). Disynaptic Inhibition between Neocortical Pyramidal Cells Mediated by Martinotti Cells. *Neuron*, 53(5):735–746.

Sizemore, A. E., Giusti, C., Kahn, A., Vettel, J. M., Betzel, R. F., and Bassett, D. S. (2018). Cliques and cavities in the human connectome. *Journal of computational neuroscience*, 44:115–145.

Stuart, G. J. and Sakmann, B. (1994). Active propogation of somatic action potentials into neocortical pyrimidal cell dendrites. *Nature*, 367(January):69–72.

Towlson, E. K., Vértes, P. E., Ahnert, S. E., Schafer, W. R., and Bullmore, E. T. (2013). The rich club of the c. elegans neuronal connectome. *Journal of Neuroscience*, 33(15):6380–6387.

Tsodyks, M. and Markram, H. (1997). The neural code between neocortical pyramidal neurons depends on neurotransmitter release probability. *PNAS*, 94:719–723.

Van Geit, W., Gevaert, M., Chindemi, G., Rössert, C., Courcol, J. D., Muller, E. B., Schürmann, F., Segev, I., and Markram, H. (2016). BluePyOpt: Leveraging open source software and cloud infrastructure to optimise model parameters in neuroscience. *Frontiers in Neuroinformatics*, 10(17).

Varani, S., Vecchia, D., Zucca, S., Forli, A., and Fellin, T. (2022). Stimulus Feature-Specific Control of Layer 2 / 3 Subthreshold Whisker Responses by Layer 4 in the Mouse Primary Somatosensory Cortex. *Cerebral Cortex*, 32(7):1419–1436.

Vargas-Caballero, M. and Robinson, H. P. (2003). A slow fraction of Mg2+ unblock of NMDA receptors limits their contribution to spike generation in cortical pyramidal neurons. *Journal of Neurophysiology*, 89(5):2778–2783.

Wang, Y., Gupta, A., Toledo-Rodriguez, M., Wu, C. Z., and Markram, H. (2002). Anatomical, physiological, molecular and circuit properties of nest basket cells in the developing somatosensory cortex. *Cerebral cortex*, 12(4):395–410.

Wohrer, A., Humphries, M. D., and Machens, C. K. (2013). Population-wide distributions of neural activity during perceptual decision-making. *Progress in neurobiology*, 103:156–193.

Wozny, C. and Williams, S. R. (2011). Specificity of synaptic connectivity between layer 1 inhibitory interneurons and layer 2/3 pyramidal neurons in the rat neocortex. *Cerebral Cortex*, 21(8):1818–1826.

Yang, D., Günter, R., Qi, G., Radnikow, G., and Feldmeyer, D. (2020). Muscarinic and Nicotinic Modulation of Neocortical Layer 6A Synaptic Microcircuits Is Cooperative and Cell-Specific. *Cerebral Cortex*, 30(6):3528–3542.

Yang, D., Qi, G., Ding, C., and Feldmeyer, D. (2022). Layer 6A Pyramidal Cell Subtypes Form Synaptic Microcircuits with Distinct Functional and Structural Properties. *Cerebral Cortex*, 32(10):2095–2111.

Yu, J., Hu, H., Agmon, A., and Svoboda, K. (2019). Recruitment of gabaergic interneurons in the barrel cortex during active tactile behavior. *Neuron*, 104(2):412–427.

Table S1: Excitatory synaptic pathways. Average class parameters are marked in bold and are used predictively (in lack of reference *in vitro* data) for the remaining pathways belonging to the same class. Physical dimensions are as follows: peak conductance $\hat{g}$: nS, depression and facilitation time constants D, F, and the EPSC τ_{decay}: ms, the Hill coefficient of the nonlinear, $[Ca^{2+}]_o$ dependent scaling of release probability U_{Hill}: mM, the release probability U_{SE}, the average number of vesicles in the release-ready pool N_{RRP}, and the NMDA/AMPA ratio $\hat{g}_{ratio}$ are dimensionless.

Pre	**Post**	$\hat{g}$	U_{SE}	D	F	N_{RRP}	τ_{decay}	$\hat{g}_{ratio}$	U_{Hill}
				PC to Sst+IN (E1)					
PC	MC	0.2±0.1	0.09±0.12	138±211	670±830	1.5	1.74±0.18	0.8	2.79
PC	**PT**	**0.6±0.5**	**0.02±0.00**	**194±18**	**507±37**	**4.5**	**1.74±0.18**	**0.8**	**1.09**
PC	**DT**	**0.2±0.1**	**0.02±0.00**	**194±18**	**507±37**	**1.5**	**1.74±0.18**	**0.8**	**2.79**
				PC to PC (E2)					
L23_PC	L23_PC	1.0±0.5	0.46±0.26	671±17	17±5	2.6	1.74±0.18	0.7	2.79
L4_PC	L4_PC	0.6±0.3	0.86±0.09	671±17	17±5	1.0	1.74±0.18	0.9	2.79
L4_SSC	L23_PC	0.2±0.1	0.79±0.04	671±17	17±5	1.8	1.74±0.18	0.5	2.79
L5_STPC	L5_STPC	0.9±0.3	0.39±0.03	690±90	44±21	1.0	1.74±0.18	0.7	2.79
L5_TTPC	L5_TTPC	1.9±1.0	0.38±0.10	365±100	25±45	2.8	1.74±0.18	0.7	2.79
L23_PC	L5_TTPC	0.5±0.2	0.50±0.02	671±17	17±5	1.5	1.74±0.18	0.7	2.79
L4_SSC	L5_STPC	0.6±0.3	0.50±0.02	671±17	17±5	1.2	1.74±0.18	0.7	2.79
L4_SSC	L6_PC	0.4±0.2	0.50±0.02	671±17	17±5	1.0	1.74±0.18	0.7	2.79
L6_TPC:A	L6_TPC:A	1.0±0.5	0.37±0.11	280±90	90±80	1.0	1.74±0.18	0.7	2.79
L6_TPC:C	L6_TPC:C	0.5±0.2	0.23±0.06	420±340	200±130	1.0	1.74±0.18	0.7	2.79
L6_IPC	L6_IPC	0.9±0.3	0.23±0.06	420±340	200±130	1.0	1.74±0.18	0.7	2.79
L6_PC to same L6_PC		**0.8±0.2**	**0.23±0.06**	**420±340**	**200±130**	**1.0**	**1.74±0.18**	**0.7**	**2.79**
L6_TPC:A	L6_TPC:C	1.2±0.5	0.23±0.06	420±340	200±130	1.0	1.74±0.18	0.7	2.79
L6_TPC:A	L6_BPC	0.3±0.1	0.23±0.06	420±340	200±130	1.0	1.74±0.18	0.7	2.79
L6_TPC:C	L6_IPC	0.2±0.1	0.23±0.06	420±340	200±130	1.0	1.74±0.18	0.7	2.79
L6_IPC	L6_BPC	0.4±0.1	0.23±0.06	420±340	200±130	1.0	1.74±0.18	0.7	2.79
L6_BPC	L6_TPC:A	0.2±0.1	0.23±0.06	420±340	200±130	1.0	1.74±0.18	0.7	2.79
L6_PC to diff. L6_PC		**0.5±0.4**	**0.23±0.06**	**420±340**	**200±130**	**1.0**	**1.74±0.18**	**0.7**	**2.79**
PC	**PC**	**0.7±0.4**	**0.50±0.02**	**671±17**	**17±5**	**1.5**	**1.74±0.18**	**0.7**	**2.79**
				PC to Sst-IN (E2)					
PC	NBC	0.6±0.4	0.72±0.12	227±70	13±24	4.5	1.74±0.18	0.8	1.09
PC	**PT**	**0.6±0.5**	**0.50±0.02**	**671±17**	**17±5**	**4.5**	**1.74±0.18**	**0.8**	**1.09**
PC	L1_GABAB-	0.3±0.1	0.50±0.02	671±17	17±5	1.5	1.74±0.18	0.8	1.94
L6_TPC:A	L6_BC	0.4±0.1	0.58±0.13	240±80	70±90	1.5	1.74±0.18	0.8	1.09
L6_TPC:C	L6_BC	0.4±0.1	0.36±0.21	380±310	280±340	1.5	1.74±0.18	0.8	1.09
L6_IPC	L6_BC	0.3±0.1	0.51±0.20	440±300	100±50	1.5	1.74±0.18	0.8	1.09
L6_PC	**L6_BC**	**0.4±0.1**	**0.47±0.21**	**370±290**	**155±215**	**1.5**	**1.74±0.18**	**0.8**	**1.09**
PC	**IN**	**0.4±0.1**	**0.50±0.02**	**671±17**	**17±5**	**1.5**	**1.74±0.18**	**0.8**	**1.94**

Proximal Targeting inhibitory mtypes: N/L/SBC, CHC. N/LBC etypes: cACint, cIR, bAC, bIR, cNAC have E1, while the rest of etypes; and SBC and CHC mtypes have E2 short-term dynamics.
Distal Targeting inhibitory mtypes: BP, DBC, BTC. L1_GABAB- comprise all non NGC mtypes in L1

Table S2: Inhibitory synaptic pathways. Average class parameters are marked in bold and are used predictively (in lack of reference *in vitro* data) for the remaining pathways belonging to the same class. Physical dimensions are as follows: peak conductance $\hat{g}$: nS, depression and facilitation time constants D, F, and the IPSC τ_{decay}: ms, the Hill coefficient of the nonlinear, $[Ca^{2+}]_o$ dependent scaling of release probability U_{Hill}: mM, the release probability U_{SE}, the average number of vesicles in the release-ready pool N_{RRP}, and the $GABA_B/GABA_A$ ratio $\hat{g}_{ratio}$ are dimensionless.

Pre	**Post**	$\hat{g}$	U_{SE}	D	F	N_{RRP}	τ_{decay}	$\hat{g}_{ratio}$	U_{Hill}
				IN to PC (I1)					
L6_BC	L6_BC	2.3±0.5	0.16±0.10	45±21	376±253	1.0	10.40±6.20	0.0	1.94
SBC (cACint)	PC	1.9±1.0	0.16±0.10	45±21	376±253	3.3	10.40±6.20	0.0	1.94
				IN to PC and IN (I2)					
MC	PC	3.0±1.5	0.30±0.08	1250±520	2±4	1.0	8.30±2.20	0.0	1.94
DT	**PC**	**3.0±1.5**	**0.25±0.13**	**706±405**	**21±9**	**1.0**	**8.30±2.20**	**0.0**	**1.94**
NBC	PC	1.9±1.0	0.14±0.05	875±285	22±5	3.3	8.30±2.70	0.0	1.94
NGC	PC	0.2±0.1	0.25±0.13	706±405	21±9	1.0	36.50±1.30	0.8	1.94
L1_GABAB-	PC	0.3±0.1	0.25±0.13	706±405	21±9	1.0	8.30±2.20	0.0	1.94
SBC (dNAC)	PC	1.9±1.0	0.25±0.13	706±405	21±9	3.3	8.30±2.20	0.0	1.94
IN	*****	**2.3±0.5**	**0.25±0.13**	**706±405**	**21±9**	**1.0**	**8.30±2.20**	**0.0**	**1.94**
				IN to PC (I3)					
L6_BC	L6_PC	1.9±1.0	0.44±0.25	195±190	200±320	1.0	10.40±6.20	0.0	1.94
PT	**PC**	**1.9±1.0**	**0.32±0.14**	**144±80**	**62±31**	**3.3**	**6.40±1.70**	**0.0**	**1.94**

Proximal Targeting inhibitory mtypes: N/L/SBC, CHC. N/LBC etypes: cNAC, dSTUT, cSTUT, bSTUT have I3, while the rest of etypes; and SBC (except: cACint and dNAC) and CHC mtypes have I2 short-term dynamics. Distal Targeting inhibitory mtypes: BP, DBC, BTC. L1_GABAB- comprise all non NGC mtypes in L1

Table S3: Thalamocortical synaptic pathways. Values taken from the internal connectivity (Table S1) are marked in bold. Physical dimensions are the same as in Table S1.

Pre	**Post**	$\hat{g}$	U_{SE}	D	F	N_{RRP}	τ_{decay}	$\hat{g}_{ratio}$	U_{Hill}
				VPM, POm to Sst+IN (E1)					
*	Sst+	**0.2±0.1**	**0.09±0.12**	**138±211**	**670±830**	**1.5**	**1.74±0.18**	**0.8**	**2.79**
				VPM, POm to PC (E2)					
VPM	L23_PC	1.7±0.6	0.75±0.1	**671±17**	**17±5**	**1.5**	**1.74±0.18**	**0.7**	**2.79**
VPM	L4_PC	1.1±0.4	0.75±0.1	**671±17**	**17±5**	**1.5**	**1.74±0.18**	**0.7**	**2.79**
VPM	L56_PC	2.4±0.9	0.75±0.1	**671±17**	**17±5**	**1.5**	**1.74±0.18**	**0.7**	**2.79**
POm	PC	1.7±0.6	0.75±0.1	**671±17**	**17±5**	**1.5**	**1.74±0.18**	**0.7**	**2.79**
				VPM, POm to PV+IN (E2)					
VPM	L4_PV+	1.4±0.4	**0.72±0.12**	**227±70**	**13±24**	**4.5**	**1.74±0.18**	**0.8**	**1.09**
VPM	L6_PV+	3.1±1.0	**0.72±0.12**	**227±70**	**13±24**	**4.5**	**1.74±0.18**	**0.8**	**1.09**
VPM	L235_PV+	2.2±0.4	**0.72±0.12**	**227±70**	**13±24**	**4.5**	**1.74±0.18**	**0.8**	**1.09**
POm	PV+	2.2±0.4	**0.72±0.12**	**227±70**	**13±24**	**4.5**	**1.74±0.18**	**0.8**	**1.09**
				VPM, POm to 5HT3aR+IN (E2)					
*	5HT3aR+	**0.4±0.1**	**0.50±0.02**	**671±17**	**17±5**	**1.5**	**1.74±0.18**	**0.8**	**1.94**

Sst+ inhibitory mtypes: MC and BP, DBC, BTC (cACint etype only). PV+ inhibitory mtypes: N/LBC, CHC. 5HT3aR+ mtypes: the rest of the mtypes not listed above (e.g. NGC, SBC, and everything in L1).

Table S4: Validation of PSP amplitudes (see Figure 3B1)

Pre	**Post**	*in vitro* (mV)	*in silico* (mV)	Reference
L23_PC	L23_PC	1.00±0.70	0.99±0.67	Feldmeyer et al. (2006)
L23_PC	L5_TTPC	0.30±0.30	0.30±0.24	Reyes and Sakmann (1999)
L4_EXC	L4_EXC	1.59±1.51	1.62±1.31	Feldmeyer et al. (1999)
L4_SSC	L23_PC	0.70±0.60	0.66±0.34	Feldmeyer et al. (2002)
L4_SSC	L5_STPC	0.60±0.40	0.59±0.33	Feldmeyer et al. (2005)
L4_SSC	L6_PC	0.29±0.16	0.30±0.30	Qi and Feldmeyer (2016)
L5_TTPC	L5_TTPC	1.30±1.10	1.24±0.73	Markram et al. (1997a)
L5_STPC	L5_STPC	0.80±0.20	0.75±0.40	Le Bé et al. (2007)
L6_BPC	L6_TPC:A	0.21±0.00	0.22±0.15	Berger (2009)
L6_IPC	L6_BPC	0.42±0.18	0.42±0.21	Berger (2009)
L6_IPC	L6_IPC	1.05±0.31	1.09±0.81	Berger (2009)
L6_TPC:C	L6_IPC	0.18±0.00	0.19±0.13	Berger (2009)
L6_TPC:C	L6_TPC:C	0.43±0.22	0.43±0.29	Berger (2009)
L6_TPC:A	L6_BPC	0.32±0.27	0.31±0.17	Berger (2009)
L6_TPC:A	L6_TPC:C	1.19±0.15	1.10±0.63	Berger (2009)
L6_TPC:A	L6_TPC:A	1.51±0.98	1.45±1.11	Berger (2009)
L23_PC	L1_GABAB-	1.10±0.30	1.09±0.83	Wozny and Williams (2011)
L4_EXC	L4_FS	2.20±2.20	2.17±2.46	Beierlein et al. (2003)
L5_TTPC	L5_MC	0.28±0.30	0.28±0.33	Silberberg and Markram (2007)
L6_IPC	L6_BC	1.59±1.60	1.56±1.48	Berger (2009)
L6_TPC:A	L6_BC	2.20±3.28	2.02±1.44	Berger (2009)
L6_TPC:C	L6_BC	1.29±1.65	1.28±0.84	Berger (2009)
L6_PC	L6_MC	0.20±0.12	0.15±0.14	Berger (2009)
L1_NGC	L23_PC	0.58±0.10	0.54±0.41	Wozny and Williams (2011)
L1_GABAB-	L23_PC	0.27±0.04	0.26±0.13	Wozny and Williams (2011)
L4_FS	L4_EXC	1.10±0.80	1.14±0.81	Beierlein et al. (2003)
L5_MC	L5_TTPC	0.50±0.40	0.47±0.25	Silberberg and Markram (2007)
VPM	L4_EXC	2.40±2.00	2.51±2.10	Beierlein et al. (2003)
VPM	L4_FS	4.10±3.20	4.09±2.52	Beierlein et al. (2003)
VPM	L6_EXC	1.20±0.80	1.28±1.96	Beierlein and Connors (2002)
VPM	L6_FS	3.90±3.50	3.11±2.57	Beierlein and Connors (2002)
Thick-tufted mtypes: L5_TPC:A, L5_TPC:B. Slender-tufted mtypes: L5_TPC:C, L5_UPC.				

Table S5: Validation of first PSP amplitudes' CVs (see Figure 3B2)

Pre	**Post**	*in vitro* (mV)	*in silico* (mV)	Reference
L4_EXC	L4_EXC	0.37±0.16	0.25±0.06	Feldmeyer et al. (1999)
L4_EXC	L4_FS	0.27±0.13	0.38±0.25	Beierlein et al. (2003)
L4_FS	L4_EXC	0.25±0.11	0.28±0.09	Beierlein et al. (2003)
L4_SS	L5_STPC	0.33±0.20	0.43±0.06	Feldmeyer et al. (2005)
L4_SS	L6_PC	0.50±0.11	0.51±0.06	Qi and Feldmeyer (2016)
L4_SS	L23_PC	0.27±0.13	0.32±0.07	Feldmeyer et al. (2002)
L5_TTPC	L5_TTPC	0.31±0.14	0.39±0.09	Barros-Zulaica et al. (2019)
L5_STPC	L5_STPC	0.58±0.24	0.51±0.06	Le Bé et al. (2007)
L23_PC	L23_PC	0.33±0.18	0.43±0.15	Feldmeyer et al. (2006)
L234_PC	L234_NBC	0.32±0.08	0.21±0.08	Wang et al. (2002)
Thick-tufted mtypes: L5_TPC:A, L5_TPC:B. Slender-tufted mtypes: L5_TPC:C, L5_UPC.				

Table S6: Validation of mPSC frequency (see Figure 3E2)

Pre	**Post**	*in vitro* (Hz)	*in silico* (Hz)	Reference
E	L23_PC	8.20±2.90	9.36±4.38	Brasier and Feldman (2008)
E	L4_PC	11.90±2.40	15.64±7.84	Brasier and Feldman (2008)
E	L6_CC	2.80±0.80	3.87±2.14	Yang et al. (2020)
E	L6_CT	0.95±0.36	1.41±0.74	Yang et al. (2020)
I	L5_PC	21.10±4.80	16.06±6.74	Ling and Benardo (1999)

Cortico-cortical mtypes: L6_UPC, L6_IPC, L6_HPC.
Cortico-thalamic mtypes: L6_TPC:A, L6_TPC:C.

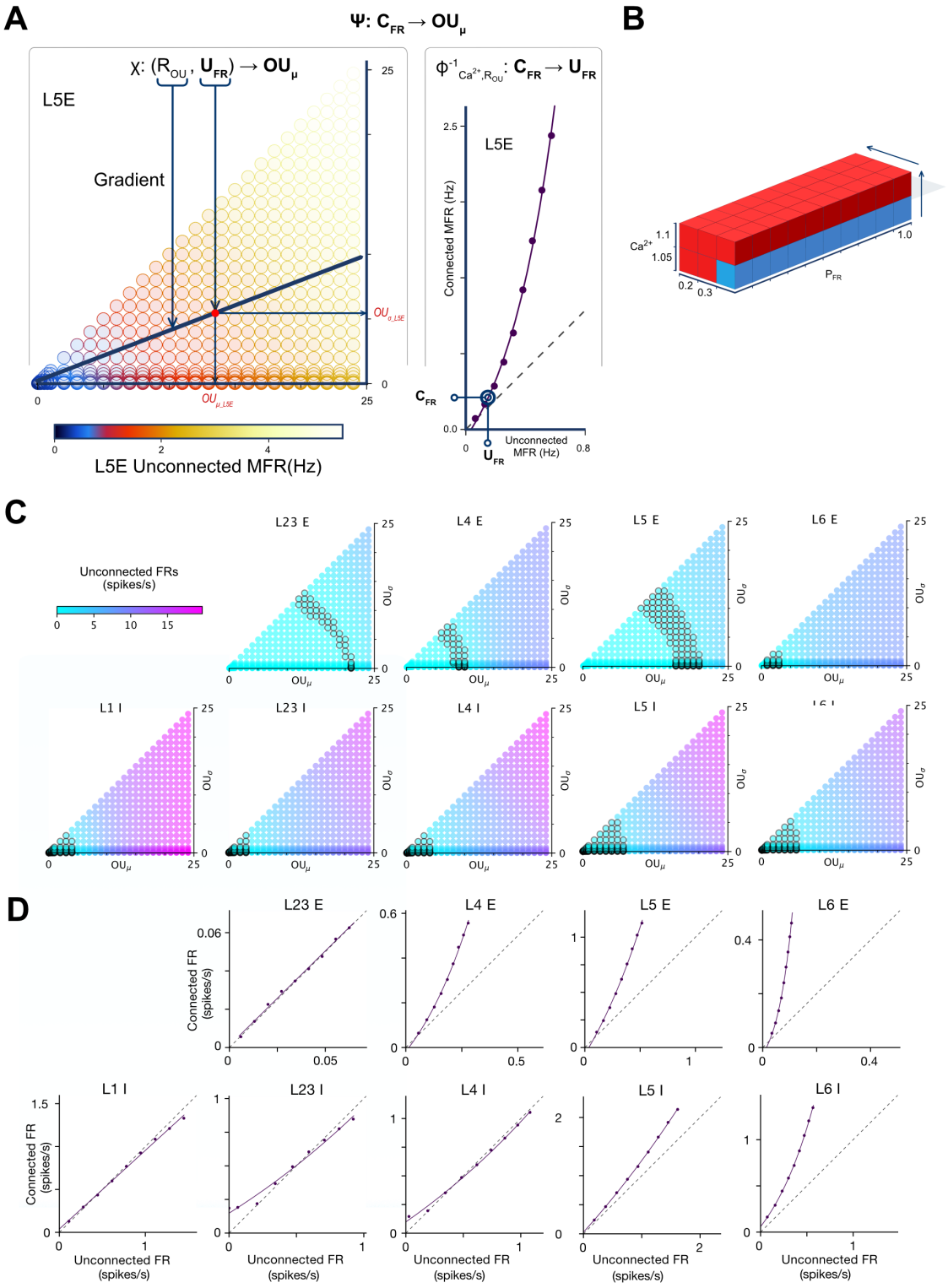

Figure S1: Spontaneous activity calibration: estimating χ and ϕ. A: Estimation of χ and ϕ for L5 E (illustration). $\Psi_{Ca^{2+},R_{OU}} : \boldsymbol{C_{FR}} \mapsto \boldsymbol{OU_{\mu}}$ is estimated by dividing it into the two functions χ and ϕ, which are determined separately. Left: $\chi : (R_{OU}, \boldsymbol{U_{FR}}) \mapsto \boldsymbol{OU_{\mu}}$. The color of each point shows the mean unconnected FR in a single column for L5E for different combinations

of OU_μ (x-axis) and OU_σ (y-axis). For a given value of R_{OU} interpolation is used over the datapoints to estimate the predicted FRs along a line of gradient R_{OU} starting at the origin. As FRs increase monotonically with increasing OU_μ and OU_σ, the interpolation can be used to estimate the OU_μ and OU_σ combination that will produce a given target unconnected FR. Right: $\phi_{Ca^{2+},R_{OU}} : \boldsymbol{U_{FR}} \mapsto \boldsymbol{C_{FR}}$. In each iteration, 10 simulations of the seven hexagon subvolume are run for a range of target P_{FR} values. For each population (i.e. L5 E) an exponential is fit to unconnected vs. connected firing rates, and used to estimate unconnected firing rates which will achieve target connected firing rates on the next iteration. **B:** Visualisation of the meta-parameter space. The algorithm is run for a single combination of Ca^{2+} and R_{OU} (blue), and is then generalised for other combinations (red). **C:** Data for estimation of χ for each population. Population FRs from unconnected simulations of a single column. Simulations vary by OU_μ and OU_σ. Colour shows FR. Black circles show region where FRs are greater than 0 and less than the population's *in vivo* reference FR. The dependence of unconnected FR on OU_μ and OU_σ is heterogeneous across populations. **D:** Final estimation of $\phi_{1.1,0.4}$ for each neuron group. Exponential fit of unconnected vs connected FRs for each population after 5th iteration. The final fits are heterogeneous across populations.

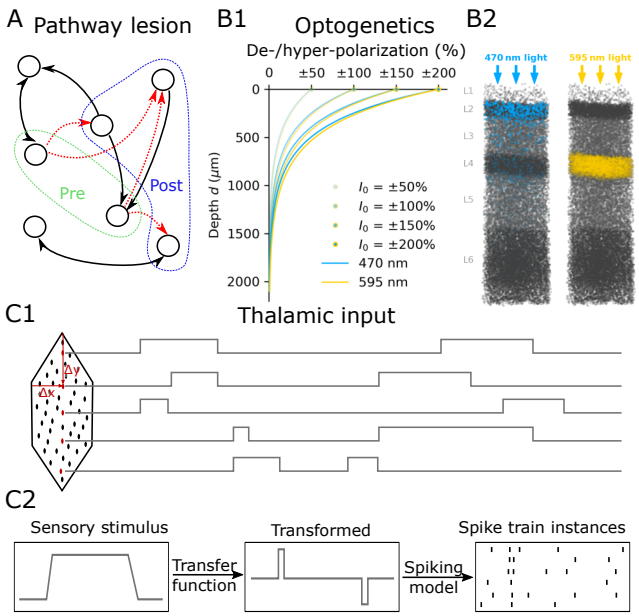

Figure S2: *In silico* experimental methods. A: Synaptic pathway lesions. After selecting a pre- (green) and post-synaptic (blue) population of neurons, connections between them in the specified direction are removed (red arrows). **B:** Optogenetic manipulations. **B1:** Decay with depth of the strength of a stimulus applied to mimic the effect of optogenetic manipulations with 470 nm (blue) and 595 nm (yellow) light. Indicated for exemplary intensities (values of I_0). **B2:** Targeted neuronal populations in two *in silico* optogenetic experiments. Density of affected cells (combination of expression level and light depth) indicated by the corresponding color of light. Unaffected populations in grey. Left: Excitation of inhibitory populations. Right: Inhibition of PCs in L4. **C:** Stimulation with thalamic inputs. **C1:** Each thalamic fiber in the model is assigned a position in a flat coordinate system. Based on the coordinates, type of fiber (VPM vs. POm), or randomly, time series of sensory stimulation are assigned to the fibers. **C2:** Sensory stimuli are transformed by a transfer function capturing pre-thalamic processing. The transfer function can simply be identity. The transformed signal is then used with a spiking model to generate stochastic spike trains that serve as inputs into a simulation.

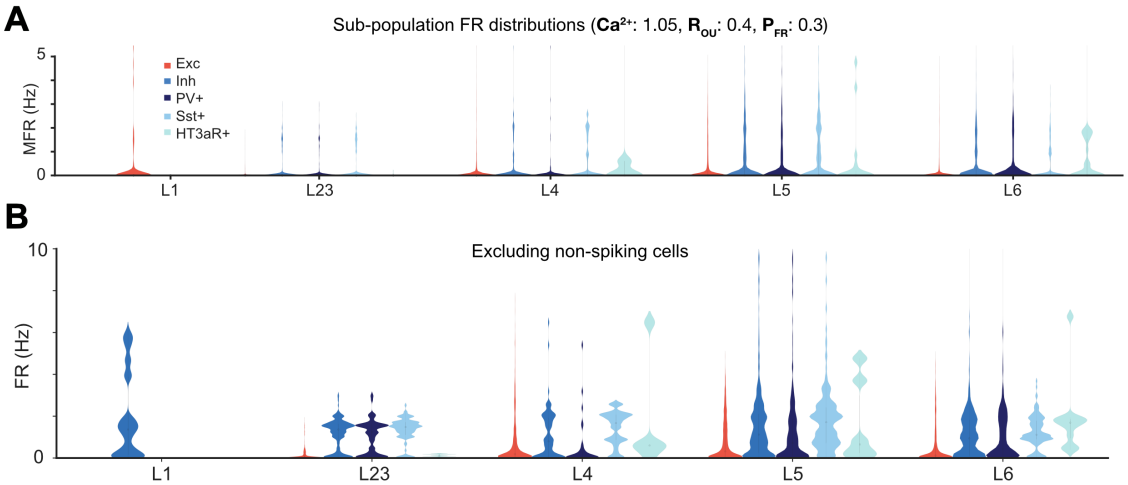

Figure S3: Firing rate distributions. A: Firing rate distributions of different subpopulations for one of the parameter combinations. **B:** Non-spiking cells are excluded for improved visualisation of the distributions.

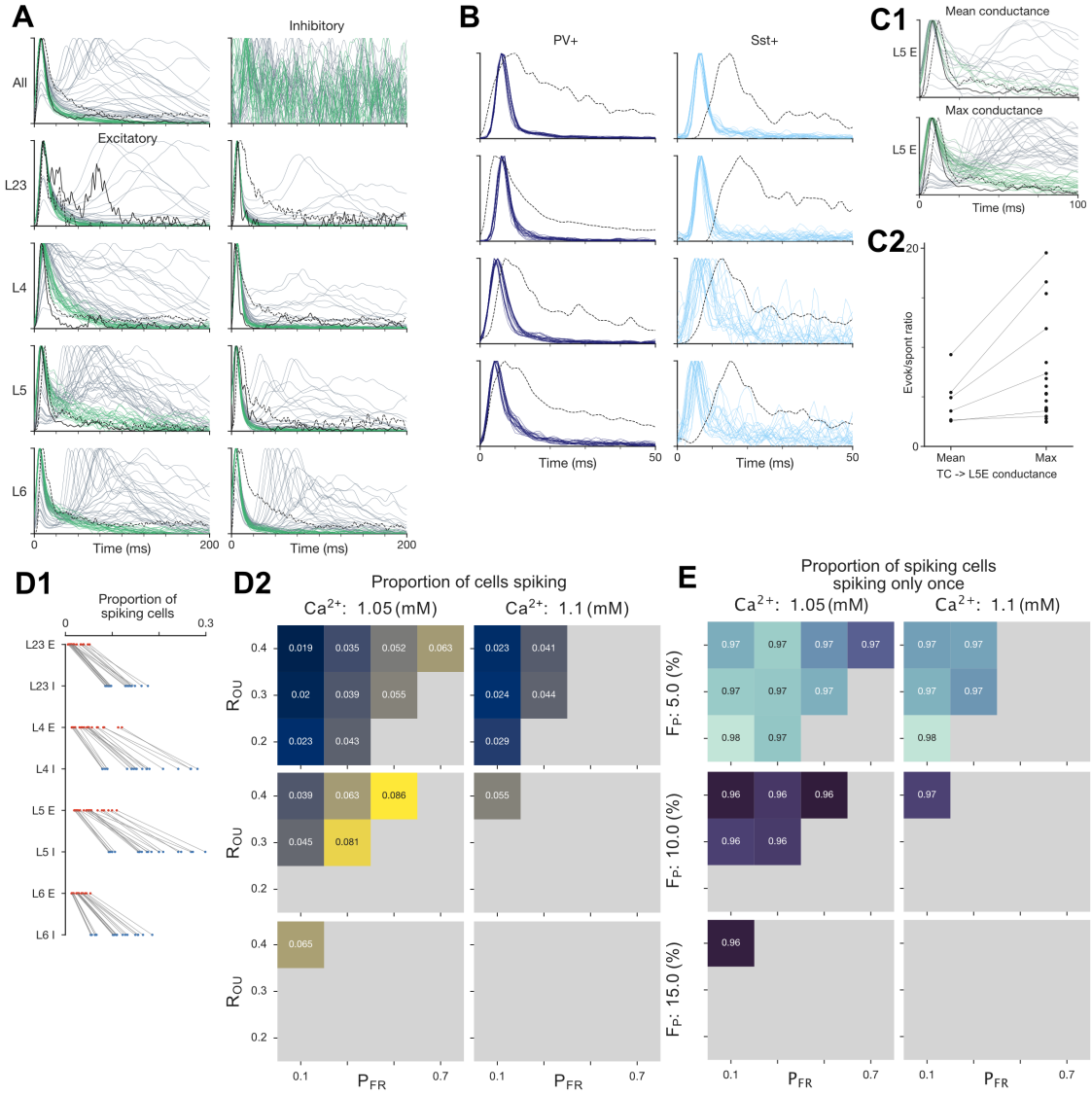

Figure S4: Whisker deflection responses - supplementary. A: PSTHs in response to the single whisker deflection stimulus for all parameter combinations. PSTHs of simulations which passed the initial criteria are coloured green, whilst those which did not are coloured grey. **B:** Layer-wise PV+ and Sst+ subpopulation PSTHs for simulations which passed the criteria. **C:** Analysis of evoked responses of L5 E under two simulation cases. The first case uses the mean of the VPM to L4 E and L6 E synaptic conductance for the VPM to L5 E conductance, whilst the second uses the maximum of the two values (VPM to L6 E). **C1:** For the two simulation cases, L5 E PSTHs for the criteria passing (green) and failing (grey) simulations. For the mean case, some of the simulations that do not burst or do not have a secondary rebound, fail the criteria because of low signal to noise ratio. **C2:** Ratios between evoked and spontaneous activity of L5 E population for criteria passing simulations. There are fewer criteria passing simulations for the mean case, and those that do are much lower than the *in vivo* reference (40.2). **D1:** Proportion of spiking cells by population in the central column over 100ms following stimulus onset. Each line represents a different criteria passing simulation. **D2:** Heatmap showing the effect of the meta-parameters on the proportion of spiking cells over the entire central column. **E:** Heatmap showing the effect of the meta-parameters on the proportion of spiking cells which spike only once over 100ms following stimulus onset.

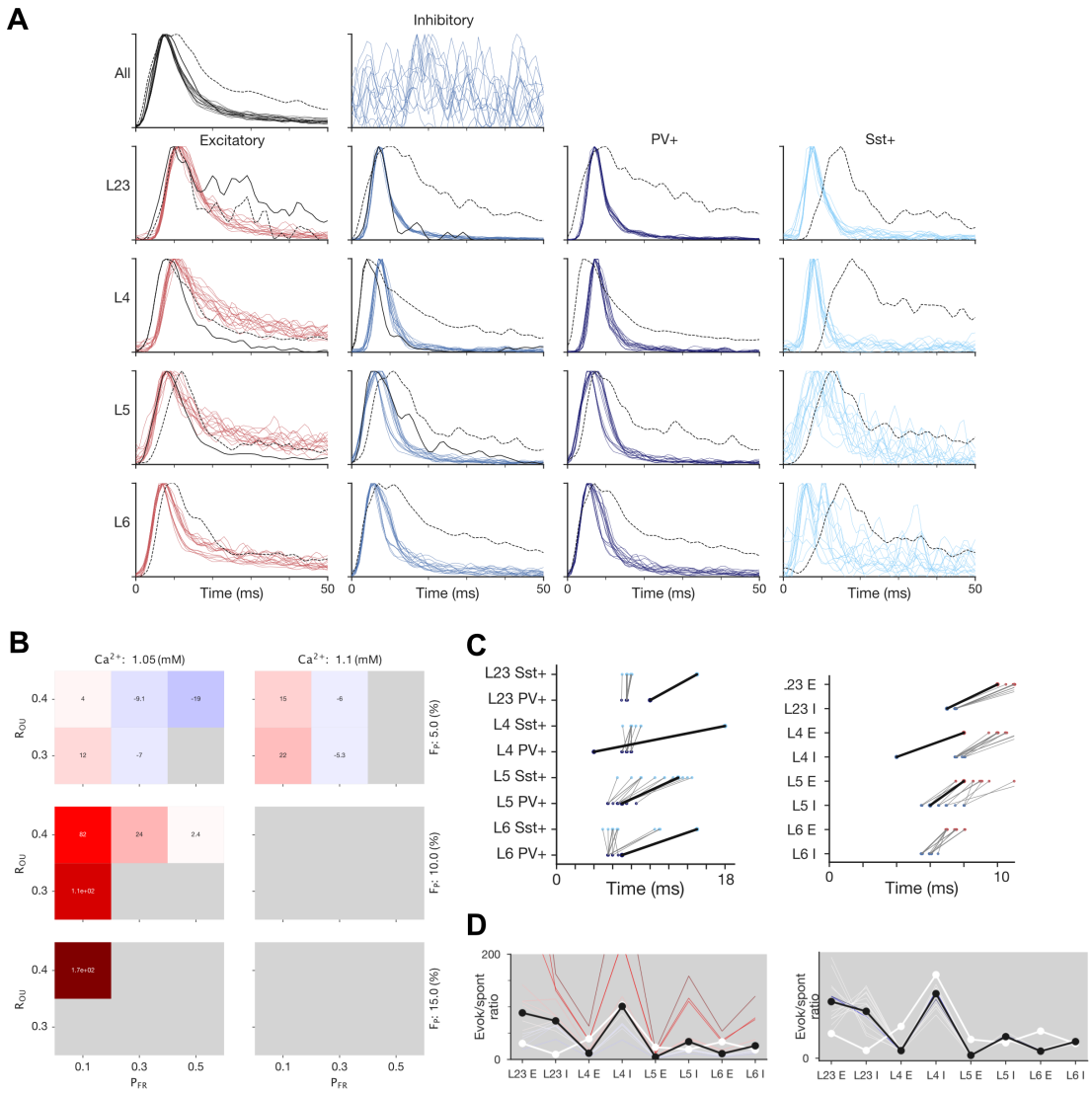

Figure S5: Active whisker touch responses - supplementary: Same as Fig. 5 but using an active whisker touch VPM stimulus and *in vivo* reference for the active whisker touch paradigm (see Methods).

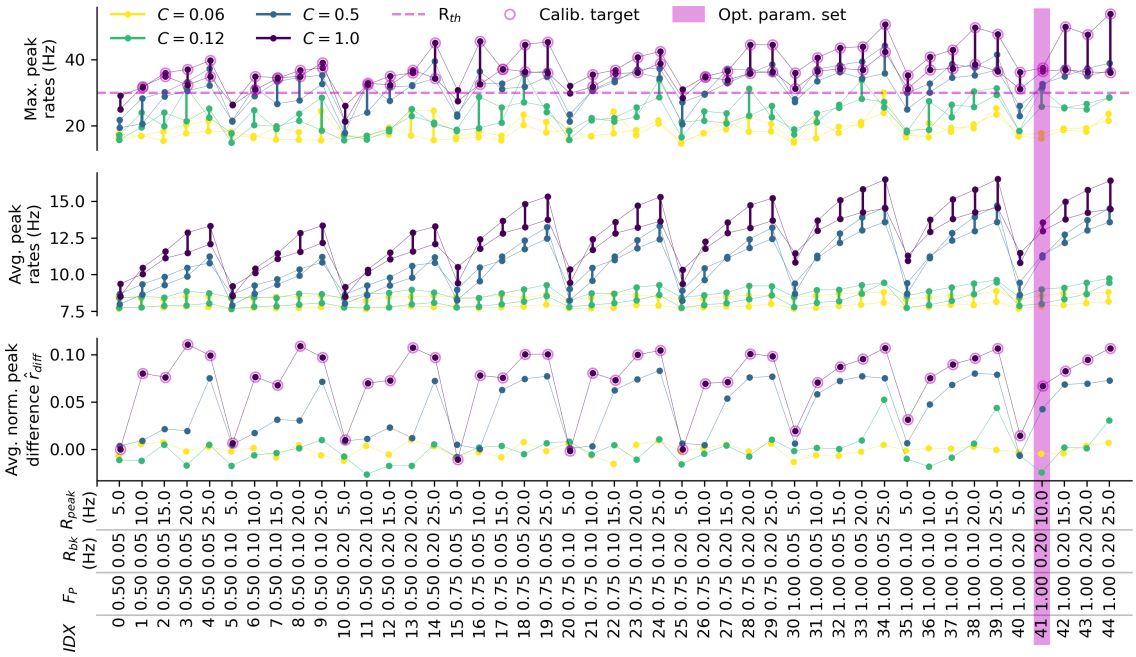

Figure S6: Calibration of the drifting grating stimulus based on peak firing rates. The drifting grating stimulus was calibrated by running a parameter scan of 45 simulations to determine optimal values for F_P, R_{bk}, and R_{peak}. The maximum (top) and average (middle) of the first and second peak firing rates r_1 and r_2 (connected points) over the whole population of PCs, together with the average of the normalized peak difference (Michelson contrast) $\hat{r}_{diff}$ (bottom) are summarized. Different colors indicate different contrast levels $C \in [0.06, 0.12, 0.5, 1.0]$. The rate threshold $r_{th} = 30\,\text{Hz}$ at maximum contrast, the calibration target values that were taken into account for selecting the optimal parameter set, as well as the optimal parameter set ($F_P = 1.0$, $R_{bk} = 0.2\,\text{Hz}$, and $R_{peak} = 10.0\,\text{Hz}$), are highlighted.

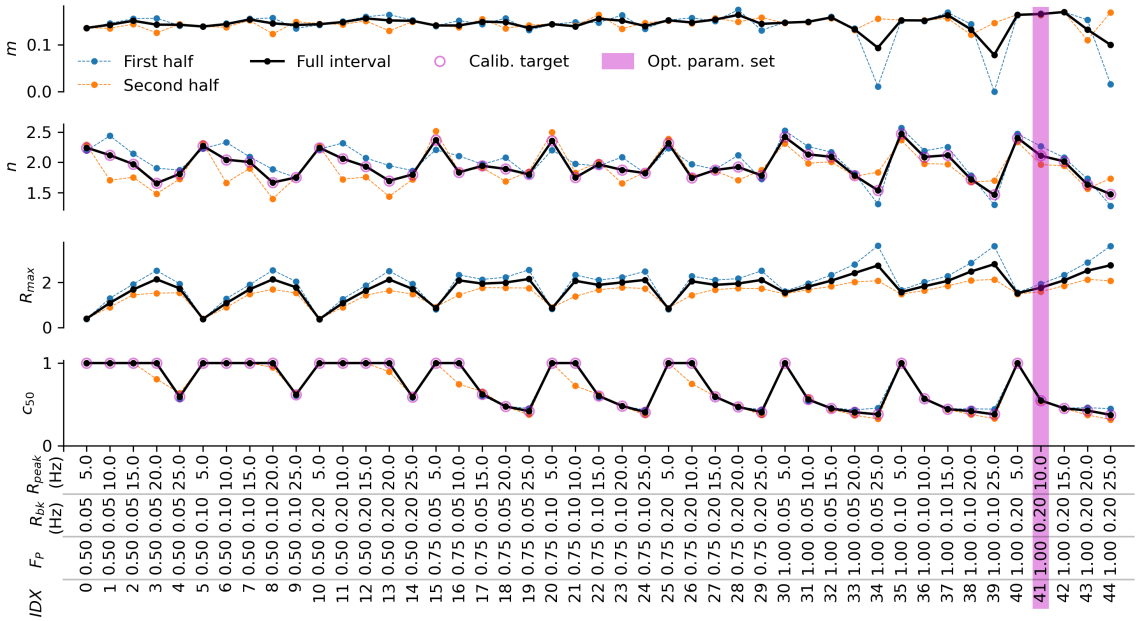

Figure S7: Calibration of the drifting grating stimulus based on sigmodal parameters. The drifting grating stimulus was calibrated by running a parameter scan of 45 simulations to determine optimal values for F_P, R_{bk}, and R_{peak}. The values of the four parameters m, n, R_{max}, and c_{50} for fitting a sigmoidal function to the average firing rates of the whole population of PCs within the full stimulation interval are summarized. Dashed lines indicate fitted parameter values when considering only the first or second half of the response interval. Calibration target values that were taken into account for selecting the optimal paramter set, as well as the optimal parameter set ($F_P = 1.0$, $R_{bk} = 0.2\,\text{Hz}$, and $R_{peak} = 10.0\,\text{Hz}$), are highlighted.

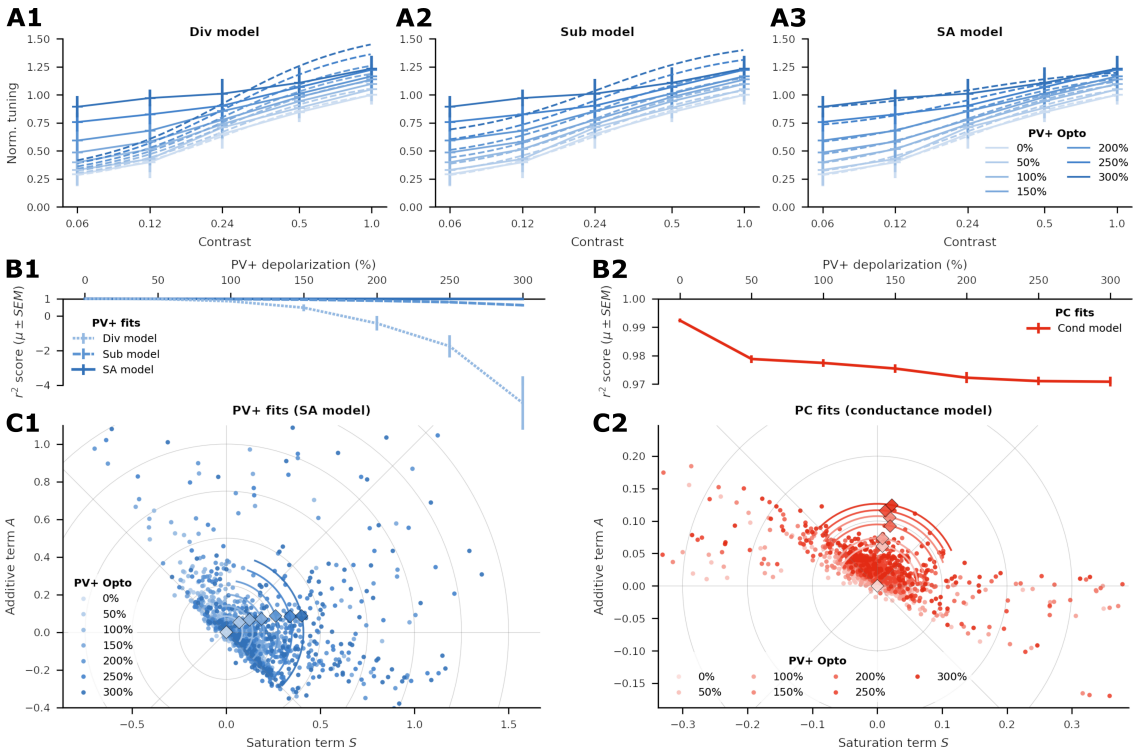

Figure S8: Modelling the effects of optogenetic stimulation of interneurons. A1-A3: Divisive scaling (Div), subtractive shifting (Sub), and saturation additive (SA) model fits (dashed lines) to responses of an exemplary PV+ interneuron (solid lines) at different levels of PV+ optogenetic stimulation, ranging from 0% (baseline) to 300%. **B1:** Goodness of Div/Sub/SA model fits ($\mu \pm SEM$ of r^2 score) for different depolarization levels over all 259 robustly tuned PV+ interneurons, showing that direct photostimulation effects on interneurons can be best described by the saturation additive model. **C1:** Polar plot of S (saturation) and A (additive) parameter values of the SA model fits to all 259 robustly tuned PV+ interneurons at different levels of PV+ optogenetic stimulation. Diamond markers indicate mean values (in polar coordinates) over neurons, colored arc lines the circular SD of the polar angles. **B2:** Same as B1, but for conductance-based model fits describing indirect photostimulation effects on all 228 robustly tuned PCs, assuming a saturating additive model description of interneurons. **C2:** Same as C1, but for the conductance-based model fits to all robustly tuned PCs.

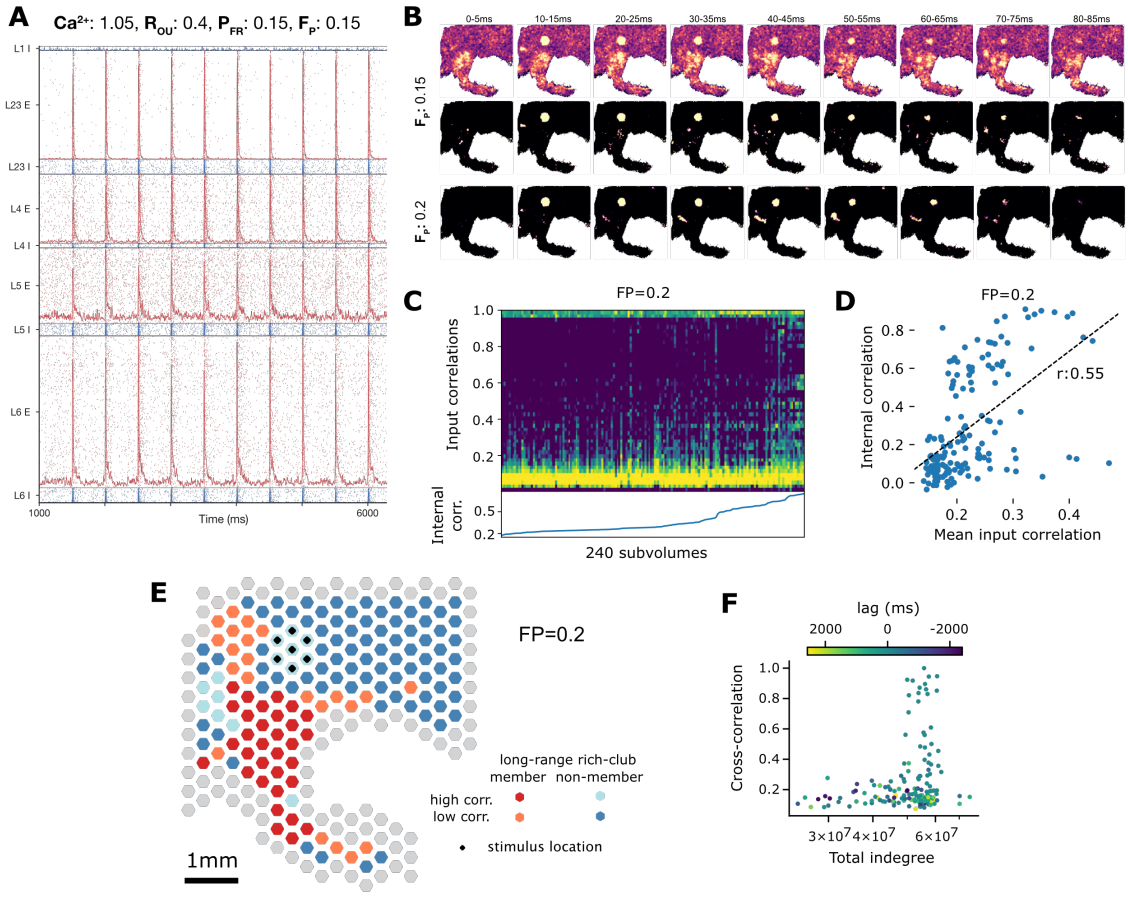

Figure S9: Full nbS1 - supplementary: **A:** Evoked responses of a single hexagonal subvolume over 10 single whisker deflections. **B:** Trial-averaged activity of the full circuit for $F_P = 15\%$ following the single whisker deflection stimulus (top). Middle and bottom: trial-averaged activity of the full circuit for $F_P = 15\%$ following the single whisker deflection stimulus for $F_P = 15\%$ and $F_P = 20\%$, showing only the top 2% of bins for each time window after the baseline activity level has been subtracted. **C:** Distribution of spiking correlations of inputs into 240 subvolumes. Calculated at reduced spatial resolution, based on connection counts and correlations between the subvolumes (see Supp. Methods). Subvolumes are sorted by the E/I correlation of neurons within them. For evoked activity with $F_P = 20\%$. **D:** Mean of the correlations of inputs into 240 subvolumes (as in C) against internal spiking correlation for all subvolumes during spontaneous activity. Black line: linear fit. Calculated based on connection counts and correlations between $50\,\mu m$ hexagonal subvolumes (see Supp. Methods). **E:** Classification of subvolumes based on low or high internal correlation and membership in the long-range rich club. Data from evoked activity with $F_P = 20\%$. **F:** Indegree from the subvolume innervated by the VPM stimulus against correlation with that subvolume, indicated for all other subvolumes. Color indicates the Δt with maximum correlation.